STUDIES ON MECHANISM OF HEAVY-ION INDUCED REACTION ON GOLD IN ENERGY REGION BELOW 10MeV/u

BY

AKIHIKO YOKOYAMA

A THESIS

SUBMITTED TO

FACULTY OF SCIENCE

OSAKA UNIVERSITY

1988

SYNOPSIS

Mechanisms of heavy-ion induced nuclear reactions in mass-asymmetric systems were studied in this study. Especially nucleon transfer reaction and compound formation reaction were investigated.

Excitation functions and projected mean recoil ranges of the target-like products in ^{37}Cl-, ^{16}O-, ^{14}N-, and ^{12}C-induced reactions on ^{197}Au were measured with γ-ray spectrometry. The energy range studied was near the Coulomb barrier of the systems and below 10MeV/u. Kinetic energy spectra and angular distributions of emitted projectile-like products in a ^{16}O-induced reaction were measured with a ΔE-E counter telescope method. The projectile energy used were 8.8MeV/u and 6.6MeV/u.

Nucleon transfer reaction was discussed distinguishing the products from quasi-elastic transfer reaction (QET) and those from deep inelastic transfer reaction (DIT). Observations indicate that QET takes place along a trajectory near the Coulomb trajectory. QET are made to be connected with interaction radius and most of the cross section ratios were reproduced well by an extended tunneling model. The tendency towards equilibration of the N/Z value and the energy damping, which are the characteristic features of DIT, are found only in the production of Au isotopes. Damped components of projectile-like products observed were concluded to be produced in a very short interaction time. Cross sections of those products were reproduced by the sum rule model better than by the diffusion model and their total kinetic energies can

also be explained well by a model using recoil formula by Siemens et al. with an assumption of short time interaction.

Excitation functions and mean projected recoil ranges of the evaporation residues in ^{16}O- and ^{12}C-induced reactions were measured with γ-ray spectrometry, and α-ray spectrometry with a ISOL and a He-jet transport system. The energy range studied were between 5MeV/u and 8MeV/u.

Fusion cross sections as a sum of cross sections of evaporation residues and that of fission were reproduced well with either of the Bass model or the extra-push model.

Competition between evaporation residue formation and fission process was discussed with a statistical calculation using fission barriers dependent on angular momentum. The excitation functions of fission and particle evaporation were reproduced well by a calculation with fission barriers predicted by the rotating finite range model.

Moreover a simple method based on the statistical model but practically with no fitting processes was described. It enabled us to define a specific J-window for preactinide fissioning systems, to deduce fission barrier $B_f(J)$ at this J-value, and to determine the effective fissioning nucleus together. The deduced fission barriers were 8.0MeV of ^{211}Fr at $16\hbar$ and 7.8MeV of ^{207}At at $27\hbar$.

CONTENTS

1. INTRODUCTION

1.1 HEAVY-ION INDUCED REACTION

The term heavy-ion induced reaction describes all nuclear reactions of projectiles heavier than ^{4}He ion. Heavy-ion induced reactions have several characteristic features; namely, a large number of angular momenta, broad distribution of angular momenta, and a great deal of excitation energy taken into the reaction system. Therefore, a variety of features of reaction can be expected in heavy-ion induced reactions. We can observe in heavy-ion induced reactions the compound formation reaction producing evaporation residues and fusion-fission products, direct reactions such as pick-up reaction, stripping and break-up reactions, and the pre-equilibrium process, which are observed also in light-ion induced reactions. Besides them, deep inelastic transfer reaction, quasi-elastic transfer reaction, and quasi-fission were found to be observed as characteristic heavy-ion induced reactions [1,2]. Quite a few nuclear physists and nuclear chemists have had a great interest in these reactions for two or three decades of years. They have tried to understand and formulate these processes through a lot of discussions of experimental results and theoretical approaches as well.

At present, heavy-ion induced reactions are distinguished by the magnitude of the involved angular momentum and divided into several reaction groups. As shown in Fig.1.1, it is considered that there are several criti-

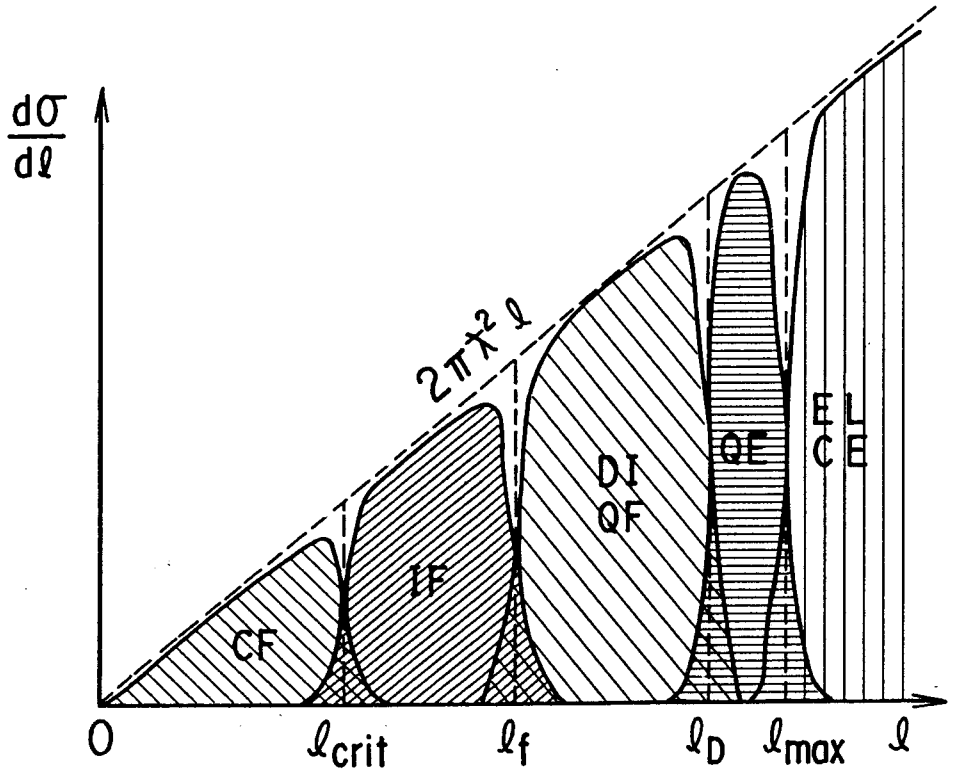

Fig.1.1 Schematic illustration of the partial cross section of the heavy-ion induced reaction for compound formation (CF), incomplete fusion (IF), deep inelastic scattering (DI), quasi-fission (QF), quasi-elastic scattering (QE), elastic scattering (EL), and Coulomb excitation (CE). $2\pi\lambda\!\!\!^{-2}\ell$ is the maximum value of the reaction cross section at each ℓ. Vertical dashed lines indicate the boundaries of the various ℓ windows in a sharp cut-off model with the characteristic ℓ values noted at the abscissa. Hatched areas represent the diffuse ℓ windows in the exact treatment. The division of the total cross section among the various processes is strongly dependent on the combination of target and projectile nuclei and on the bombarding energy. (from [3])

cal angular momentum values in a heavy-ion induced reaction system and that compound formation (CF), incomplete fusion (IF), deep inelastic scattering (DI), quasi-fission (QF), quasi-elastic processes (QE), elastic scattering (EL), and Coulomb excitation (CE) are successively seen in the increasing order of angular momentum ℓ in the figure. $2\pi \lambda\!\!\!^{-2} \ell$ is the maximum value of the reaction cross section at each ℓ [3]. The angular momentum of the reaction system is associated with the impact parameter and the depth of reaction that is equivalent to the length of interaction time or closeness of interaction distance. (see Fig.1.2.)

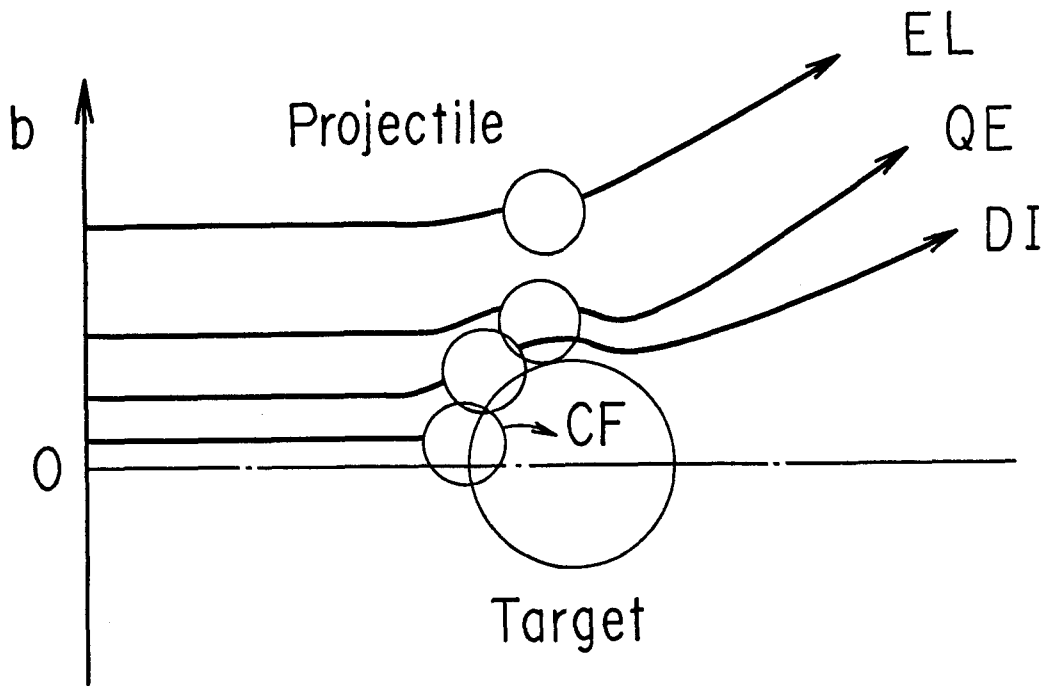

Fig.1.2. Trajectories of a projectile in the classical pictures of compound formation (CF), deep inelastic scattering (DI), quasi-elastic scattering (QE), and elastic scattering (EL). The ordinate indicates variation of impact parameter b of the reactions.

1.2 OUTLINE AND BACKGROUND OF THE PRESENT STUDY

In this study, I investigated nuclear reactions induced by ^{12}C, ^{14}N, ^{16}O, and ^{37}Cl ions on ^{197}Au. Reaction products in these mass-asymmetric systems can be distinguished by their mass numbers and divided into several product groups of different mass regions; namely,

1) light particles such as neutron, proton, α particle, etc.,
2) projectile-like products,
3) fission products which have about half as much mass numbers as the compound nucleus,
4) target-like products,
5) compound-like products which have the mass numbers of the sum of projectile and target masses. (see Fig.1.3)

Products of 2) and 4) are produced mainly in the nucleon transfer reaction, while products of 1), 3), and 5) are associated with the compound formation reaction. Therefore, I will describe the nucleon transfer reaction in section 2 and the compound formation cross section in section 3.

Cross sections of target-like products were measured as well as their projected mean recoil ranges, kinetic energy spectra and the angular distribution of emitted projectile-like products in order to make clear the heavy-ion induced reaction in a mass asymmetric system. For this purpose use was made of several techniques, such as the radiochemical method, the Δ E-E counter telescope method, rapid α-ray measurements, ISOL (isotope separator on-line), a He-jet transport system etc., to detect as many nuclides as possible which are distributed in a wide range of mass number

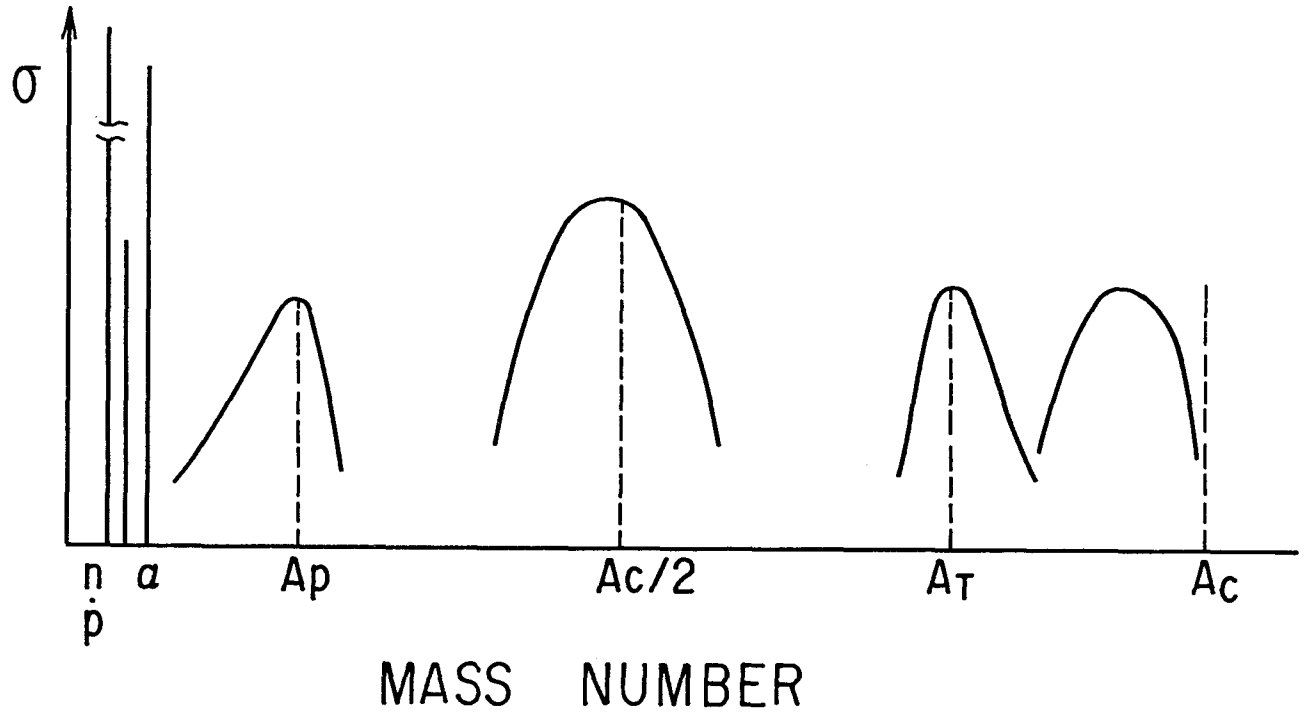

Fig.1.3. Schematic illustration of the mass distribution of reaction products in a mass-asymmetric system. The symbols A_P, A_T, and A_C represent the masses of projectile, target, and compound nucleus, respectively.

and half life.

In section 2, I will discuss the nucleon transfer reaction distinguishing quasi-elastic transfer reaction (QET) and deep inelastic transfer reaction (DIT). Cross sections of QET will be described in relation to the interaction distance whereas DIT will be discussed in relation to the interaction time and their cross sections are compared with two kinds of model calculations.

In section 3, the compound formation cross section will be compared with two kinds of model calculations for nuclear fusion. Furthermore I will discuss the fission barrier dependent on the angular momentum which determines whether compound nucleus decays into fission or particle evaporation. A newly devised method to deduce the fission barrier shall be described for a narrow angular momentum window and the neutron multiplicity of fission was deduced from the analysis competition of particle evaporation and fission.

REFERENCES TO SECTION 1

1. Bass, R.: Nuclear Reactions with Heavy Ions. Texts and Monograghs in Physics. Berlin, Heidelberg, New York: Springer-Verlag 1980
2. Lefort, M., Ngô, Ch.: Ann. Phys. (Paris) 3, 5 (1978)
3. Birkelund, J. R., Huizenga, J. R.: Ann. Rev. Nucl. Part. Sci. 33, 265 (1983)

2. MASS-ASYMMETRIC TRANSFER REACTION INDUCED BY HEAVY-IONS

2.1. INTRODUCTION

Nucleon transfer reactions induced by heavy-ions have been explained by two kinds of reaction mechanisms; namely, the quasi-elastic transfer reaction (QET) and the deep inelastic transfer reaction (DIT) [1-7]. QET is distinguished from DIT by means of differences in the amount of energy damping, in the characteristics of the angular distribution and in the degree of mass transfer, and tendencies of equilibration towards the N/Z value and equilibration along the mass-symmetry axis [3,5,7]. The quasi-elastic transfer reaction is characterized by minimum damping of the initial kinetic energy, mass transfer of a few nucleons at most, and a narrow angular distribution near the grazing angle of the relevant system, while the deep inelastic reaction is characterized by large damping of the initial kinetic energy, transfer of a large number of nucleons between two interacting nuclei, and a broad angular distribution. In addition, the N/Z equilibration has been often found to be attained in DIT at the initial stage of the process.

Though several models are applied to QET fairly rigorously [5], it is difficult to estimate their gross cross section values satisfactorily except for a tunneling model [8,9] which succeeded to reproduce the cross section below the Coulomb barrier. The diffusion model [10-17] which treats statistically DIT has been successfully utilized to explain their features

and to reproduce the kinetic energy spectra and the mass (or charge) distributions of reaction products [14,16,17]. This useful model, however, was found unable to be applied to very mass-asymmetric reaction systems [18].

In this section, I will report on transfer reaction products in light heavy-ion reactions on gold, which are mass-asymmetric systems. The experiments were performed in the energy region below 10MeV/u, where projectile fragmentation and sequential decay of the products were not expected to be important [19,20]. It follows that one is able to treat nucleon transfer reactions in those systems as two-body processes. Two types of experiments complementary to each other were carried out. One is an activation method including chemical procedure and the other is in-beam experiment using a ΔE-E counter telescope. By the former method determined were cross sections and mean projected recoil ranges of target-like products (TLP); Tl, Hg, and Au isotopes. Nuclides of half-lives longer than the order of hours were detected. With the latter technique the kinetic energy of emitted projectile-like products (PLP) was measured, atomic numbers of which are from 3 to 9. These two methods would give one useful information on energetics and kinematics in the reaction, which would serve elucidation of the reaction mechanism. Accordingly, the products of QET will be distinguished from those of DIT by means of their characteristic features. QET will be treated with an extended tunneling model and the cross sections will be explained in relation to the interaction distances. Damped reaction products in those reactions were investigated in order to clarify the singularity of DIT in a very mass-asymmetric reaction system. The results were analyzed by means of a concept of a relaxation process consisting of full and partial

equilibration. The relaxation process was in parallel treated by the diffusion model and the sum rule model [21,22], and the latter applied to the transfer reaction of mass-asymmetric systems satisfactorily. The study on target-like products is described in 2.2, 2.3, and 2.4. The study on projectile-like products is described in 2.5, 2.6, and 2.7. Some conclusions on mass-asymmetric transfer reaction are given in 2.8.

2.2. EXPERIMENTAL OF RADIOCHEMICAL METHOD

2.2.1. Irradiation System with Heavy-Ions

In the activation experiment uses were made of ^{37}Cl, ^{16}O and ^{12}C beams provided by the tandem Van de Graaff accelerator of Japan Atomic Energy Research Institute and ^{14}N beams by AVF cyclotron of Research Center for Nuclear Physics at Osaka University. I like to describe here the R-2 course installed in the tandem Van de Graaff accelerator tower. This course, which is illustrated in Fig.2.1, was chiefly used in the present study. Accelerated ions are transported in the beam course, curved by a bending magnet (D magnet), and focussed with a Q magnet to pass through three slits which are provided to arrange the size of cross section of the beam. An activation experiment was performed at the end of the beam line, where target stacks were attached to a Faraday cup and irradiated. The beam intensity was monitored with a current integrator electrically connected with the Faraday cup. In order to measure the correct beam intensity, secondary electrons were suppressed by supplying the Faraday cup with positive high voltage up to a few hundred volts.

I bombarded with the particles stacked foils consisting of several pairs of 1μm thick ^{197}Au target foil and Al catcher foil which was used to collect recoiling reaction products. The projectiles lose their kinetic energy in the foil. In order to obtain the average projecting energy in each foil, the energy loss was calculated with the OSCAR code [23], which

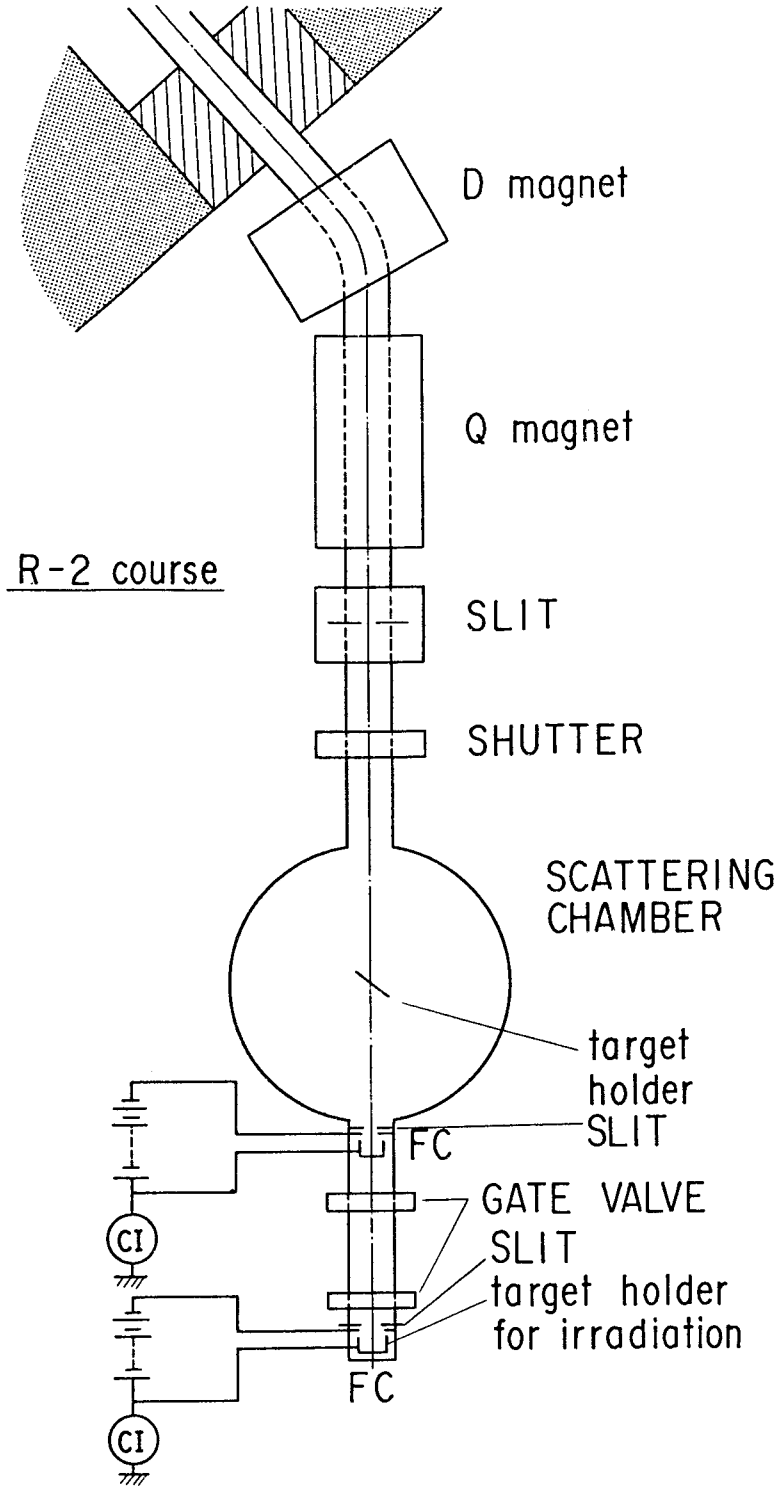

Fig.2.1. Layout of the R-2 course installed in the tandem Van de Graaff accelerator of Japan Atomic Energy Research Institute. The beam transport system consists of a bending magnet (D magnet) and a focussing magnet (Q magnet). The beam intensity was monitored by the measurement of the electric current of the Faraday cup (FC).

can calculate the stopping power and range of a particle moving in matter according to several fundamental formulas. The projectile energy used was less than 10MeV/u, which is the energy region near the Coulomb barrier of the reaction system.

Besides a counter experiment was performed in a scattering chamber installed in the same course, at the center of which targets were attached to a holder. The beam intensity was monitored with a Faraday cup (FC) near the scattering chamber. Experimental set-up of the counter experiment will be described in detail in 2.3.1.

2.2.2. γ -ray Spectroscopy with Ge-Semiconductor detector

After the bombardment of heavy-ions, γ -rays from each foil of the target stack were measured with a system shown in Fig.2.2. An ORTEC Ge(Li)-semiconductor detector is placed in a shield composed of Fe plates and Pb blocks to suppress the background of γ -rays. The sample was attached to a Lucite plate placed right above a Ge crystal of the detector. The block diagram for the measurement is also depicted in the same figure. Pulses from the detector were amplified with a pre-amplifier and then with a spectroscopy amplifier. The amplified linear pulses were converted in an analog-to-digital converter (ADC) to digital signals, which were stored in a multichannel analyzer (MCA) connected with a microcomputer making data handling easy by means of a CRT, a printer, and a floppy disk driver with it.

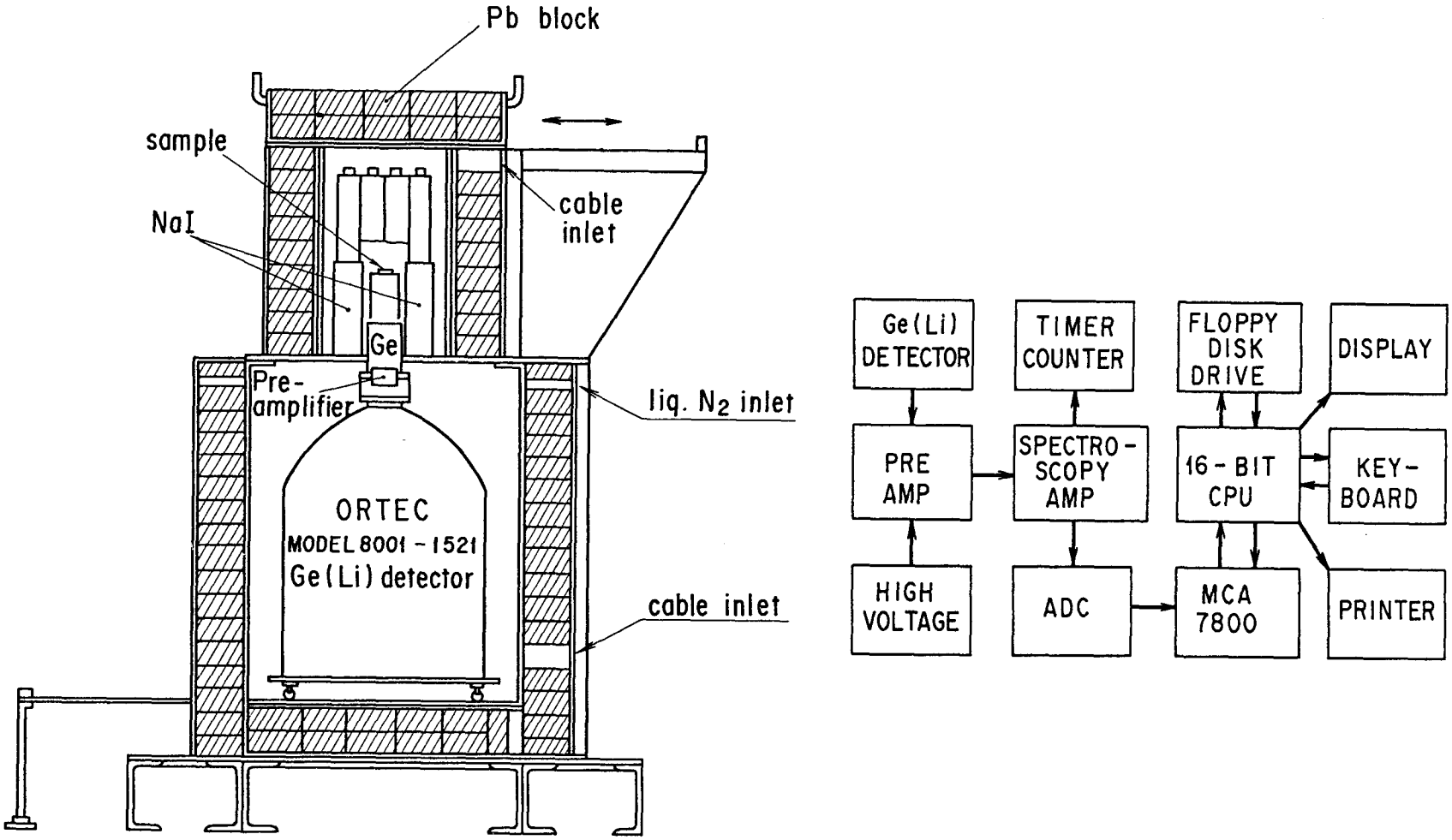

Fig.2.2. A system for the measurement of γ rays with a Ge(Li) semiconductor detector. The detector in a shield composed of Fe plates and Pb blocks (left) and the block diagram for the measurement (right) are depicted.

The Ge(Li) detector was calibrated with standard γ-rays sources. The calibration curves on energy and efficiency were obtained at the same geometry as the measurements of samples. As the standard sources a multiple-gamma source composed of some isotopes emitting one or several strong γ-rays was used together with ^{152}Eu and ^{56}Co both of which emit a number of some strong γ-rays with appropriate energy intervals. A calibration curve on the efficiency at the position 5cm apart from the surface of the detector is drawn as an example in Fig.2.3. Agreement of the measured values by multi-γ-rays emitters and a few γ-rays emitters as seen in the figure demonstrates that the distance as close as 5cm between the detector and the sample is sufficient to suppress the error due to the sum effect of γ-rays.

A γ-ray spectrum measured is shown in Fig.2.4, where the sample is chemically separated Au precipitate for the ^{37}Cl-induced reaction on ^{197}Au. In the spectrum one can see the γ-rays and x-rays emitted in the nuclear decay of ^{194}Au, ^{195}Au, ^{196}Au, ^{196m}Au, ^{198}Au, and ^{199}Au nuclides without contamination of other elements due to the chemical separation. The chemical separation will be described in detail in 2.2.3.

The cross sections were determined for the reaction products of Tl, Hg, and Au. In addition to the cross section mean projected recoil ranges for several nuclides were deduced from the ratio of the radioactivity of a target foil to that of the succeeding catcher. The values of the γ-ray emission rate per decay of Au isotopes listed in Table 2.1 [24,25] were adopted to derive the cross section values. As for the other nuclides the data of [26] were adopted.

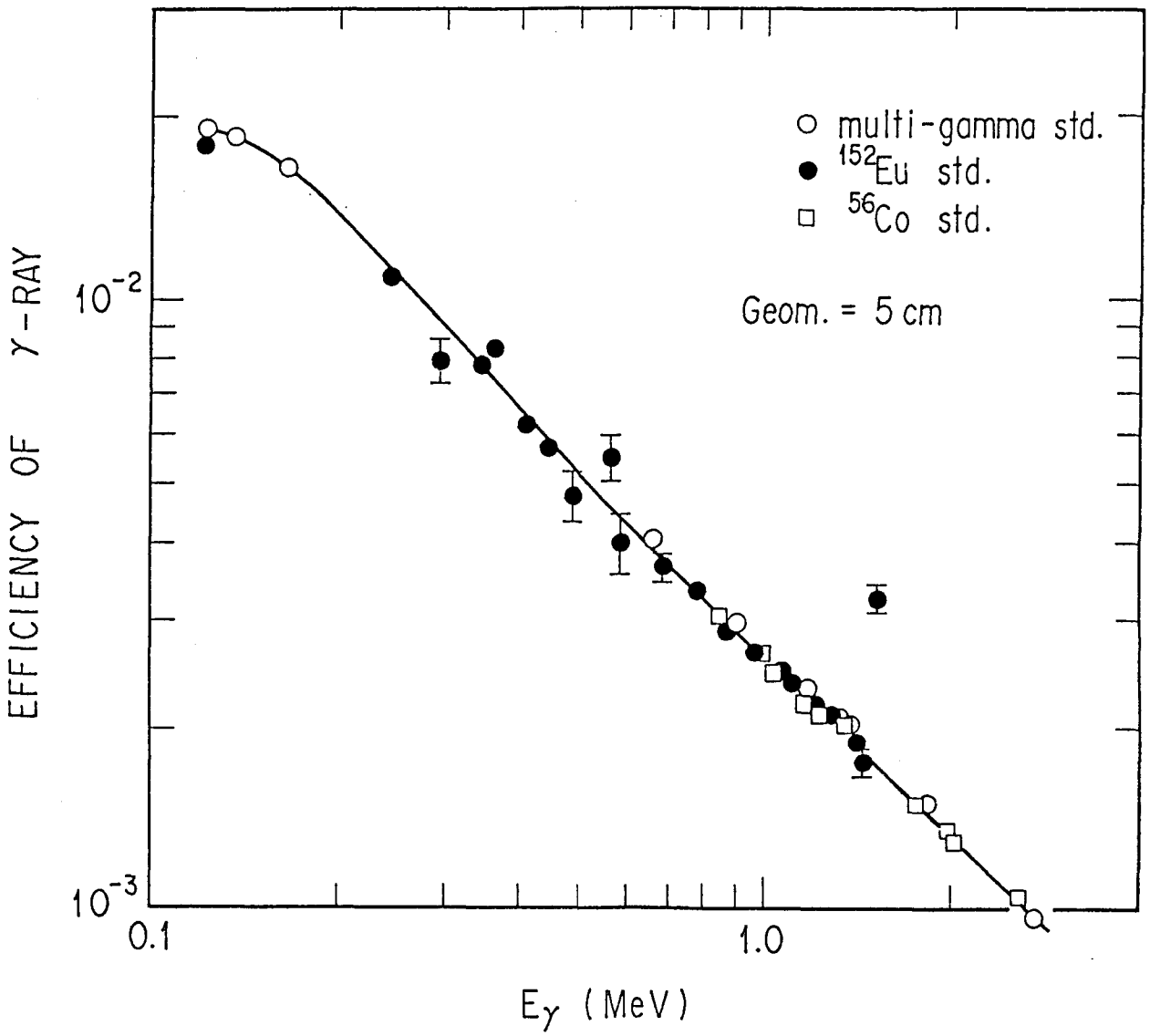

Fig.2.3. A calibration curve on the efficiency at the position 5cm apart from the surface of the detector. Open circles represent data by a multiple-gamma source composed of some isotopes emitting one or several strong γ rays, closed circles those by ^{152}Eu, and squares those by ^{56}Co.

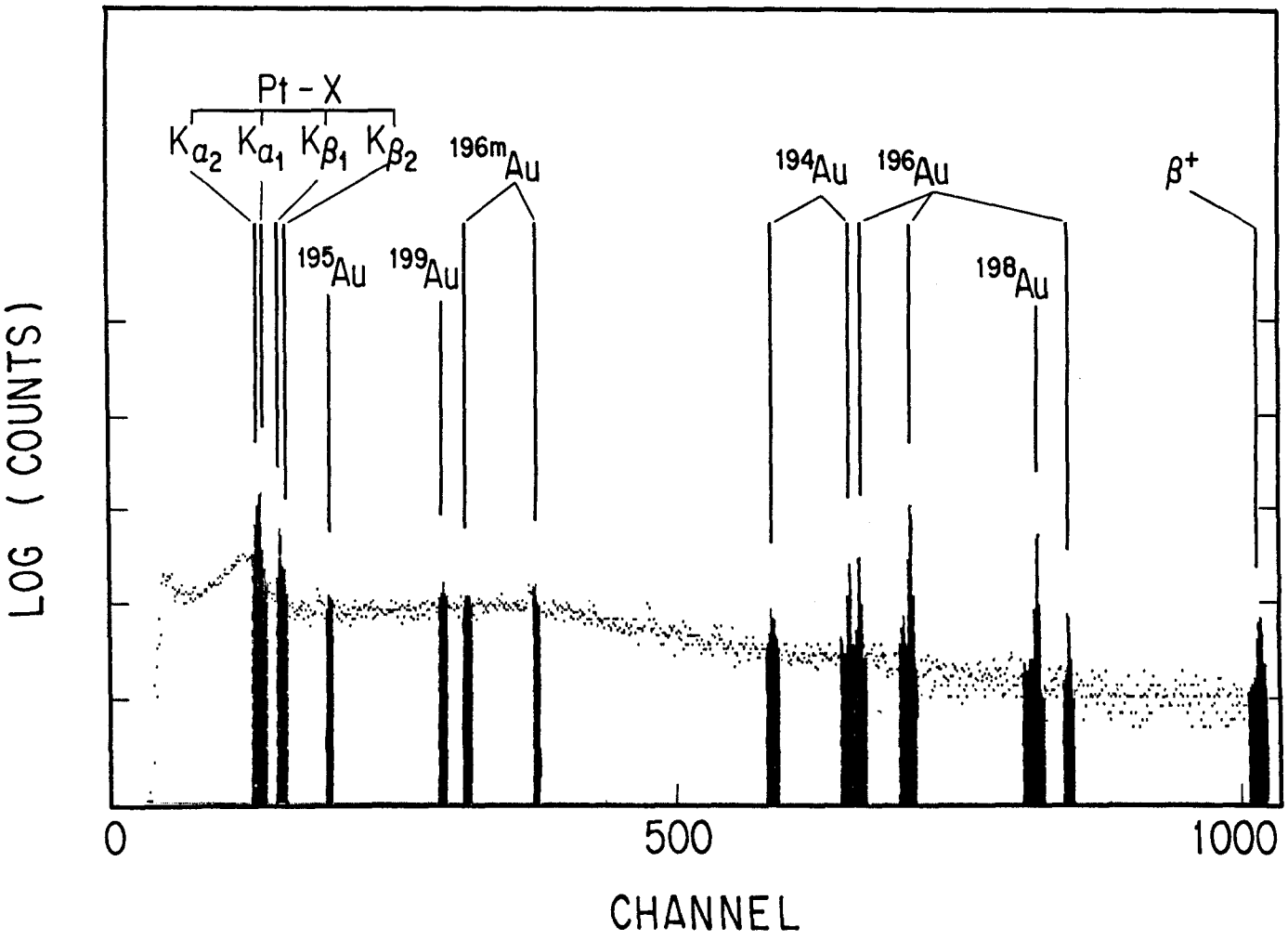

Fig.2.4. A γ-ray spectrum of chemically separated Au precipitate for the ^{37}Cl-induced reaction on ^{197}Au. In the spectrum one can see the γ rays and the x rays emitted in the nuclear decay of ^{194}Au, ^{195}Au, ^{196}Au, ^{196m}Au, ^{198}Au, and ^{199}Au nuclides.

Table 2.1. half lives and γ -ray emission rates per decay for Au nuclides

Nuclide (spin)	half life	Eγ (keV)	γ -ray emission rate
^{199}Au (3/2+)	3.148 d	158.4	0.369 ± 0.007
^{198m}Au (12-)	2.30 d	214.9	0.769
		204.1	0.415 ± 0.03
^{198}Au (2-)	2.697 d	411.8	0.955
^{196m}Au (12-)	9.7 h	147.8	0.425 ± 0.021
		188.3	0.374 ± 0.017
^{196}Au (2-)	6.183 d	355.7	0.869
		333.0	0.229 ± 0.005
^{195}Au (3/2+)	183 d	98.9	0.109 ± 0.005
^{194}Au (1-)	39.5 h	328.5	0.630
		293.6	0.110 ± 0.006
^{193}Au (3/2+)	17.65 h	186.2	0.101 ± 0.008 [25]
		255.57	0.0670 ± 0.0058
		268.2	0.0389 ± 0.0032
^{192}Au (1-)	5.03 h	316.5	0.783 ± 0.010
		295.9	0.302 ± 0.004

2.2.3. Chemical Separation of Au Element

In order to detect small yields of Au isotopes chemical separation was performed as the scheme depicted in Fig.2.5. The Au foil irradiated with heavy-ions was dissolved in aqua regia, while the Al catcher foil was dissolved with Au carrier in aqua regia as well. The solutions were dried up after adding Tl(Ⅲ) carrier of 10mg and Hg(Ⅱ) carrier of 10mg and adjusted to 0.1N in HCl. They were passed through a cation resin column with Diaion SK#1 of 5ml volume to eliminate all the cations in the solutions and obtain the solutions of At, Tl, Hg, and Au elements which form complex anions in the conditions described above. They were dried up again to adjust them to the 10ml 8N-HCl solution. Then the solutions were subjected to the solvent extraction with 10% tri-n-butyl phosphate in toluene. The At, Tl, and Au elements were extracted into the organic layer while Hg element remained in the aqueous layer [27], Tl and Au were back-extracted with conc. HNO_3. The solutions of Au were dried up again and dissolved in 20ml water. The Au element was selectively reduced with $NaHSO_3$ [28] and finally precipitated and filtered with a chimney filter to prepare the counting sources for the activity measurement.

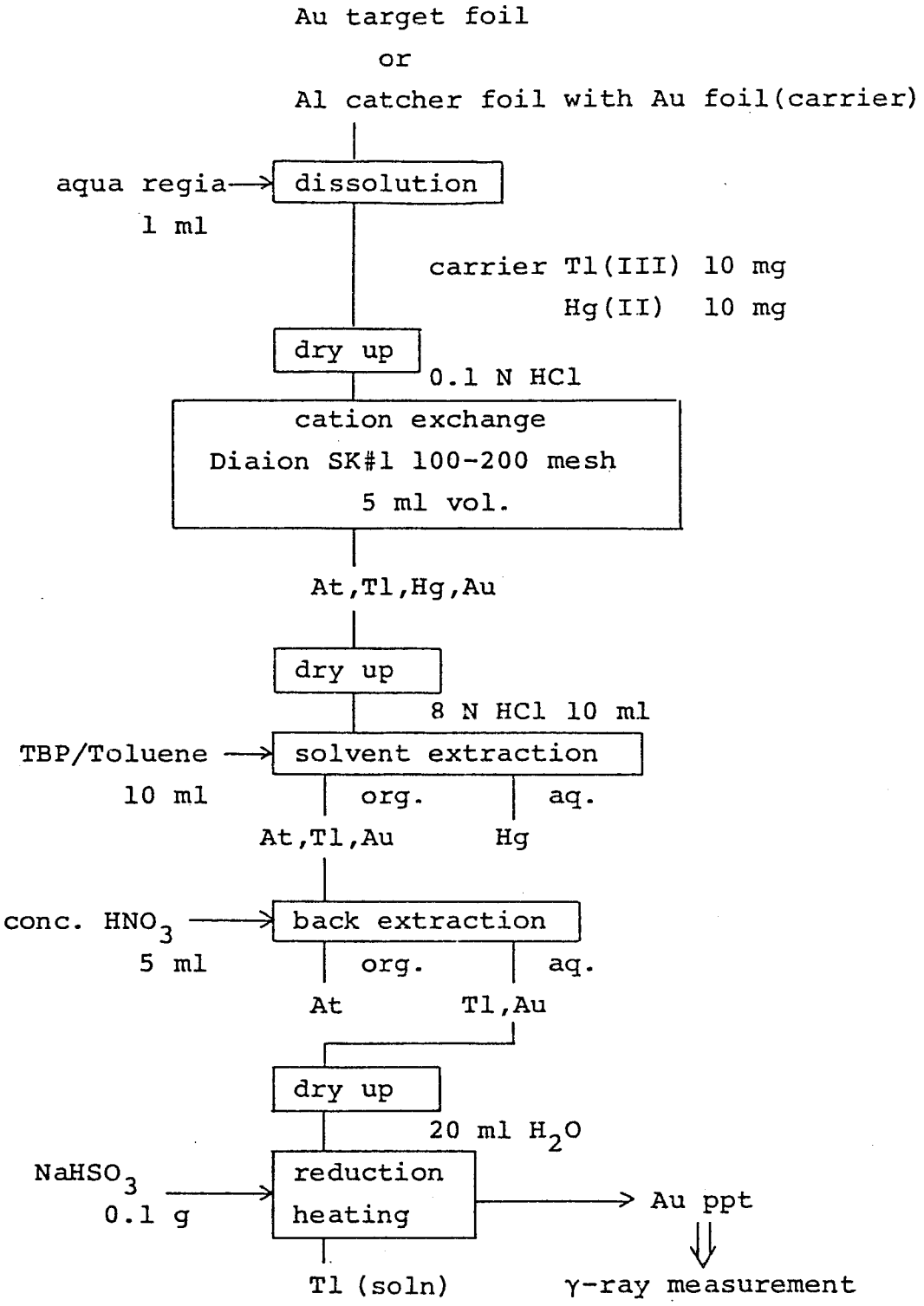

Fig.2.5. A scheme for the chemical separation of Au element.

2.3. RESULTS OF RADIOCHEMICAL EXPERIMENT

2.3.1 Excitation Functions of Target-like Products in the ^{16}O- and ^{12}C-Induced Reactions

Figure 2.6 shows excitation functions of target-like products of the ^{16}O-induced reaction. The products observed are Au, Hg, and Tl nuclides. The errors given by bars in the figure are the statistical errors in counting γ-rays. Energy values of the horizontal axis represent the average laboratory energies in each target foil. The energy loss in 1μm Au foil is less than 5MeV for a ^{16}O projectile. Observed were Au isotopes with mass numbers of 192, 193, 194, 195, 196m, 196g, and 198, Hg isotopes of 195m and 197m, and Tl isotopes of 197, 198m, 198g, 199, 200, and 201, respectively. The functions exhibit characteristic features of a peripheral reaction since the cross section values reach saturation with increase of the projecting energy and become independent of the excitation energy thereafter. Figure 2.7 shows excitation functions of Au isotopes of the ^{12}C-induced reaction. The energy loss in the target foil is less than 2MeV for a ^{12}C projectile. Au isotopes of 193, 194, 195, 196m, 196g, and 198 were observed. These functions closely resemble those of the ^{16}O-induced reaction in the feature of the projecting energy dependence. I should remark, however, that the function of ^{194}Au is somewhat different from the others in the tendency of increase in the lower energy region. It suggests that more than two kinds of reaction mechanisms contribute to the produc-

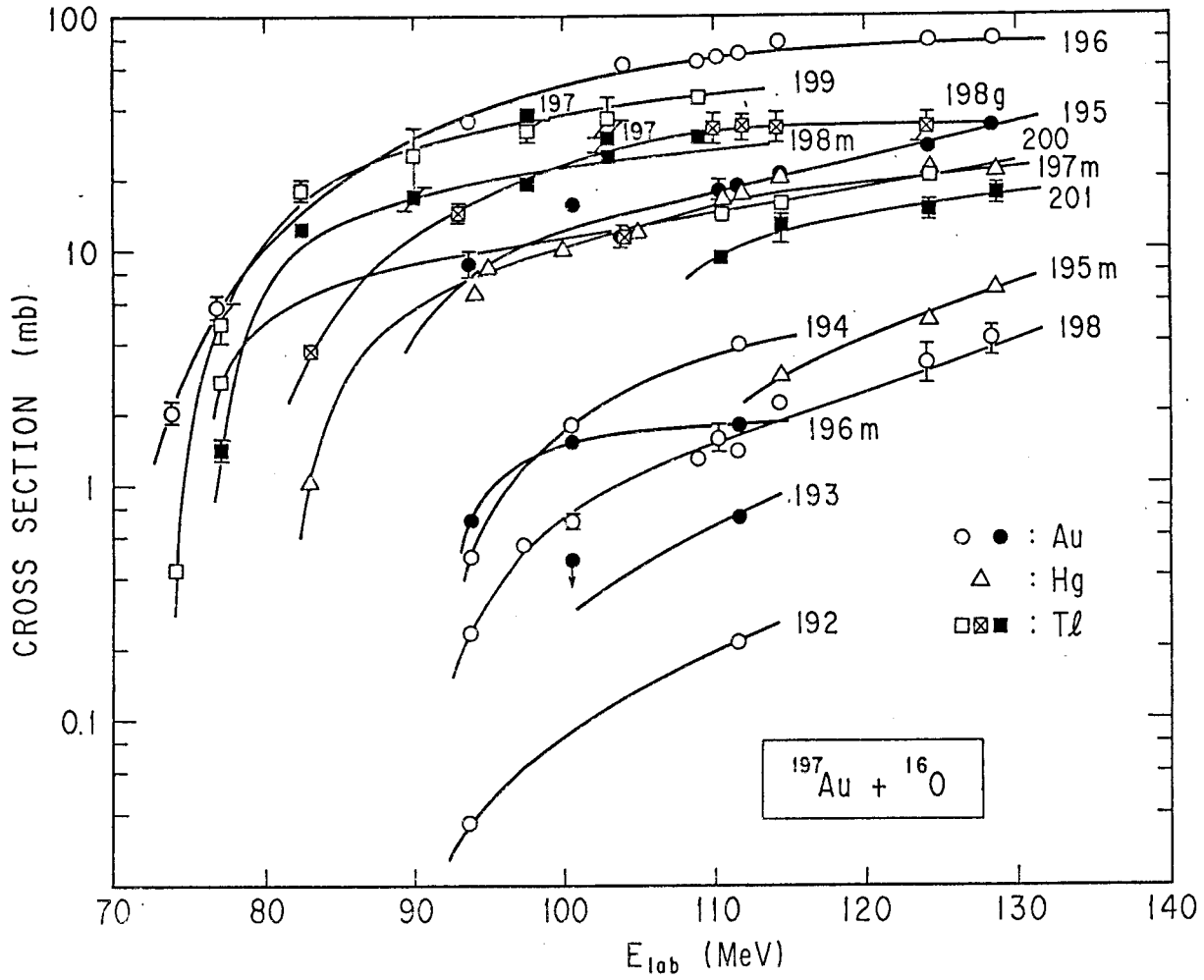

Fig.2.6. Excitation functions of target-like products of the ^{16}O-induced reaction. The products are Au, Hg, and Tl nuclides. The errors in the figure are due to statistical errors in counting γ rays. Energy values of the horizontal axis represent the average labolatory energies in each target foil.

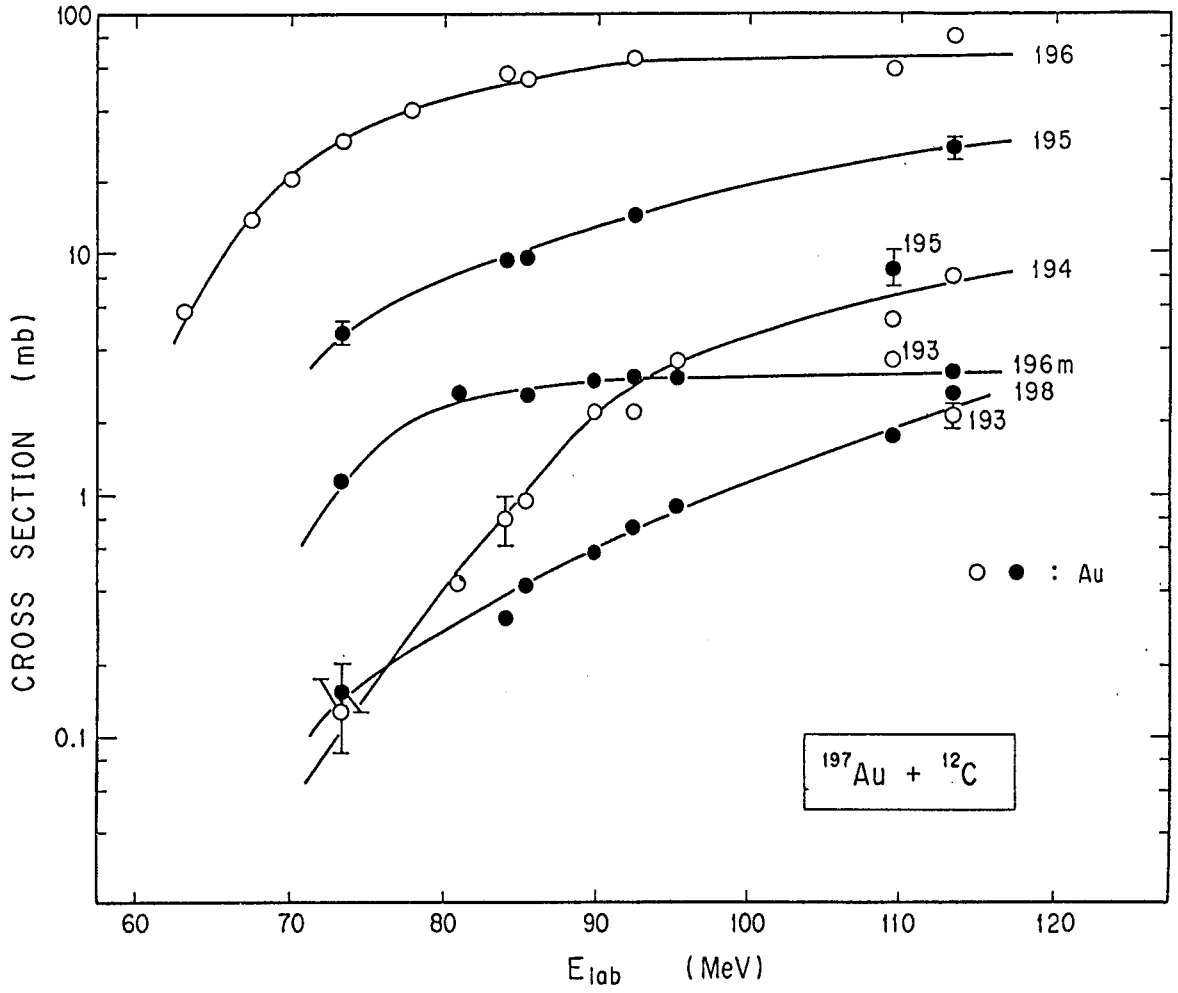

Fig.2.7. Excitation functions of Au isotopes of the ^{12}C-induced reaction. The errors in the figure are due to statistical errors in counting γ rays. Energy values of the horizontal axis represent the average labolatory energies in each target foil.

tion of Au nuclides.

2.3.2. Isotopic Distributions of Au in the ^{37}Cl-, ^{16}O-, ^{14}N-, and ^{12}C-Induced Reactions

Yields of Au isotopes in the ^{37}Cl-, ^{16}O-, ^{14}N-, ^{12}C-induced reactions are given in Table 2.2. The yields of Au isotopes of 192, 193, 194, 195, 196m, 196g, 198m, 198g, and 199 were measured owing to the chemical separation described in 2.2.3. Yields are sometimes presented as relative values to the yield of ^{196}Au. This is because the chemical yields were not obtained accurately in some cases. Chemical yields were determined by comparing the γ-ray intensities of ^{196}Au with those observed in the irradiated foil which was not subjected to chemical separation, and the measurement was not always able to be performed in a good condition. The yields except for the cases described above are given as cross sections in mb. The errors of all the yields include statistical errors in counting γ-rays, errors of the fitting process in the decay analysis, and uncertainties in the γ-ray emission rates listed in Table 2.1. The resulting isotopic distributions of Au will be discussed in detail in 2.4.1.

2.3.3. Projected Mean Recoil Ranges of Target-like Products in the ^{16}O-, ^{14}N-, and ^{12}C-Induced Reactions

Table 2.2.(a) Yields of Au isotopes in the ^{37}Cl- and ^{16}O-induced reactions on ^{197}Au

Projectile	E_{lab} (MeV)	^{199}Au	^{198}Au	^{196}Au	^{195}Au	^{194}Au	^{193}Au	^{192}Au
^{37}Cl	200*	3.5	27.3	100	52	10.7	—	2.1
		± 1.2	± 0.5		± 10	± 0.4		± 0.2
			0.8(m)	4.3(m)				
			± 0.4	± 0.3				
	180	—	4.97	21.8	6.4	0.30	—	—
			± 0.02	± 0.6	± 1.4	± 0.02		
				0.44(m)				
				± 0.04				
^{16}O	112	—	1.50	68.3	15.8	3.85	0.73	0.21
			± 0.01	± 0.1	± 0.8	± 0.01	± 0.07	± 0.01
				1.76(m)				
				± 0.06				
	101	—	0.70	50.4	15.4	1.80	—	0.48
			± 0.04	± 0.1	± 1.0	± 0.06		± 0.08
	94	—	0.259	34.9	6.27	0.495	—	0.037
			± 0.005	± 0.1	± 0.40	± 0.005		± 0.004
				0.70(m)				
				± 0.02				

* Data are presented as relative values when the yield of ^{196}Au is 100.

The other values are cross sectins in mb. (m) represents metastable isotope.

Table 2.2.(b) Yields of Au isotopes in the ^{14}N- and ^{12}C-induced reactions on ^{197}Au.

Projectile	E_{lab} (MeV)	^{199}Au	^{198}Au	^{196}Au	^{195}Au	^{194}Au	^{193}Au	^{192}Au
^{14}N	123*	—	14.6	100	22.1	7.60	1.59	1.12
			± 0.1		± 1.5	± 0.07	± 0.19	± 0.02
				2.55(m)				
				± 0.08				
	116*	—	14.1	100	23.1	6.01	0.88	0.86
			± 0.1		± 1.7	± 0.06	± 0.34	± 0.03
			0.48(m)	2.41(m)				
			± 0.03	± 0.08				
	101	—	1.51	11.82	2.2	—	—	—
			± 0.02	± 0.03	± 0.4			
	89	0.13	0.80	7.69	0.87	—	—	—
		± 0.03	± 0.01	± 0.02	± 0.14			
^{12}C	114	—	2.60	79.8	27.	7.88	2.1	—
			± 0.02	± 0.2	± 3.	± 0.03	± 0.2	
				3.2(m)				
				± 0.2				
	109	—	1.77	59.3	8.4	5.19	3.6	—
			± 0.10	± 0.2	± 1.5	± 0.03	± 0.4	

* Data are presented as relative values when the yield of ^{196}Au is 100.

The other values are cross sectins in mb. (m) represents metastable isotope.

In Fig.2.8 are plotted the mean projected recoil ranges of ^{198}Au and ^{196}Au in the ^{16}O-induced reaction. Mean projected recoil range R_{recoil} was calculated by the formula [29]:

$$R_{recoil} = \rho t \frac{Ac}{At + Ac} \frac{\sigma in + \sigma out}{2\sigma out}, \qquad (2.1)$$

where ρt is the density of the target foil, Ac is the radioactivity of a relevant nuclide recoiling into the forward catcher foil, and At is that of the same nuclide remaining in the target foil. σin and σout denote cross sections at entrance and exit of the beam for the target, respectively. The ranges are free from the errors of the γ-ray emission rate because it is cancelled out by taking the ratios of the yields. Therefore the errors are mainly due to the statistical errors. Figure 2.9 shows the mean projected recoil ranges of Tl and Hg nuclides in the ^{16}O-induced reaction. The ranges of target-like products observed are close to each other at the same bombarding energy in the ^{16}O-induced reaction. Figure 2.10 shows recoil ranges of Au nuclides in the ^{12}C-induced reaction. Recoil ranges of target-like products exhibit similar characteristic features of decreasing with increase of the projecting energy. Those products recoil out with less kinetic energies or in more forward directions with increase of the projecting energy.

In Fig.2.11 are plotted the recoil ranges as a function of the mass number of Au nuclides in the ^{14}N- and ^{12}C-induced reactions. The ranges of

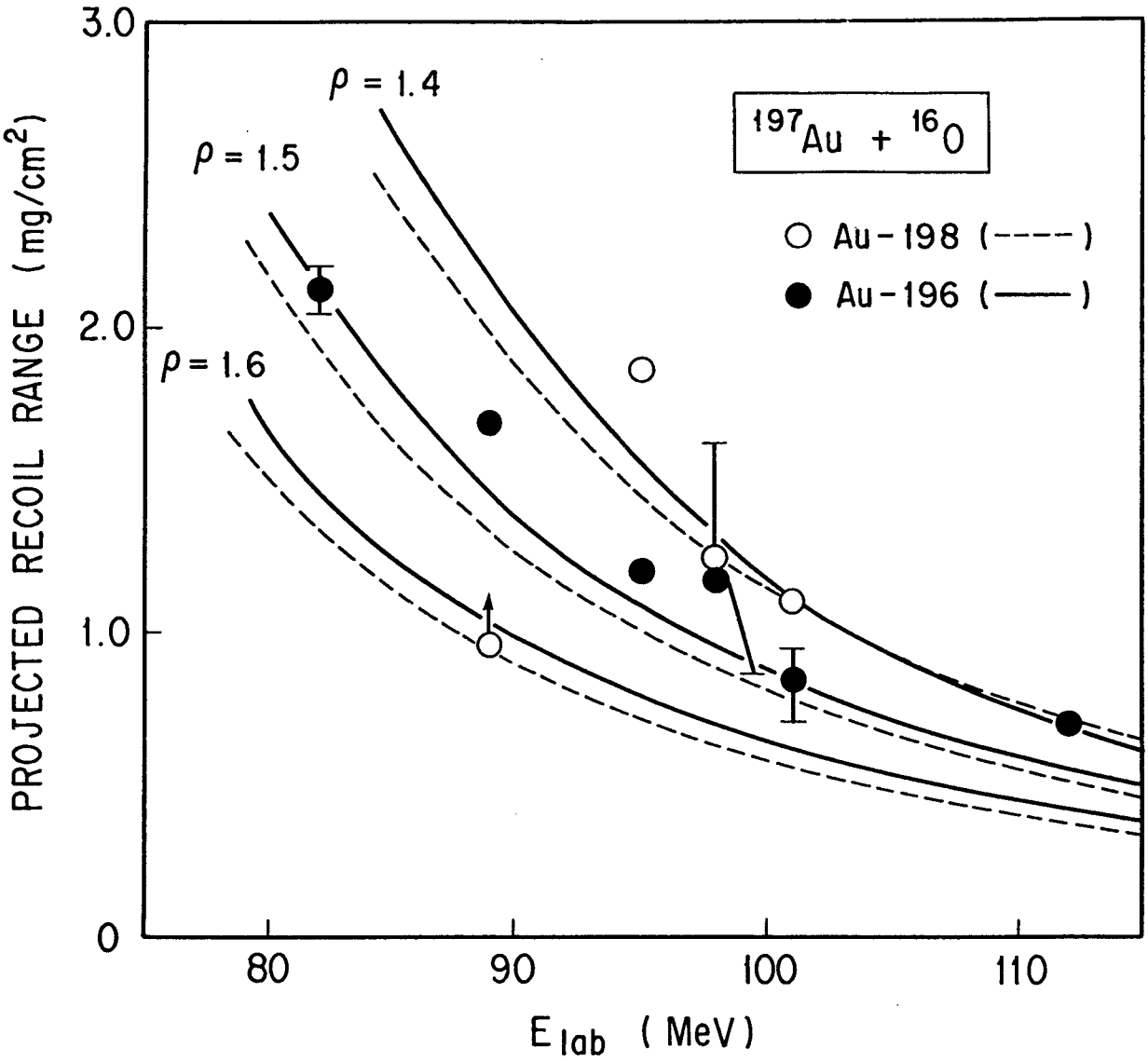

Fig.2.8. Mean projected recoil ranges of ^{196}Au and ^{198}Au in the ^{16}O-induced reaction. Solid lines and dashed lines represent the calculated recoil ranges of ^{196}Au and ^{198}Au, respectively, for ρ = 1.4, 1.5, and 1.6. ρ gives the distance of the closest approach between two interacting nuclei expressed in unit of the sum of the nuclear radii. (see 2.4.2.)

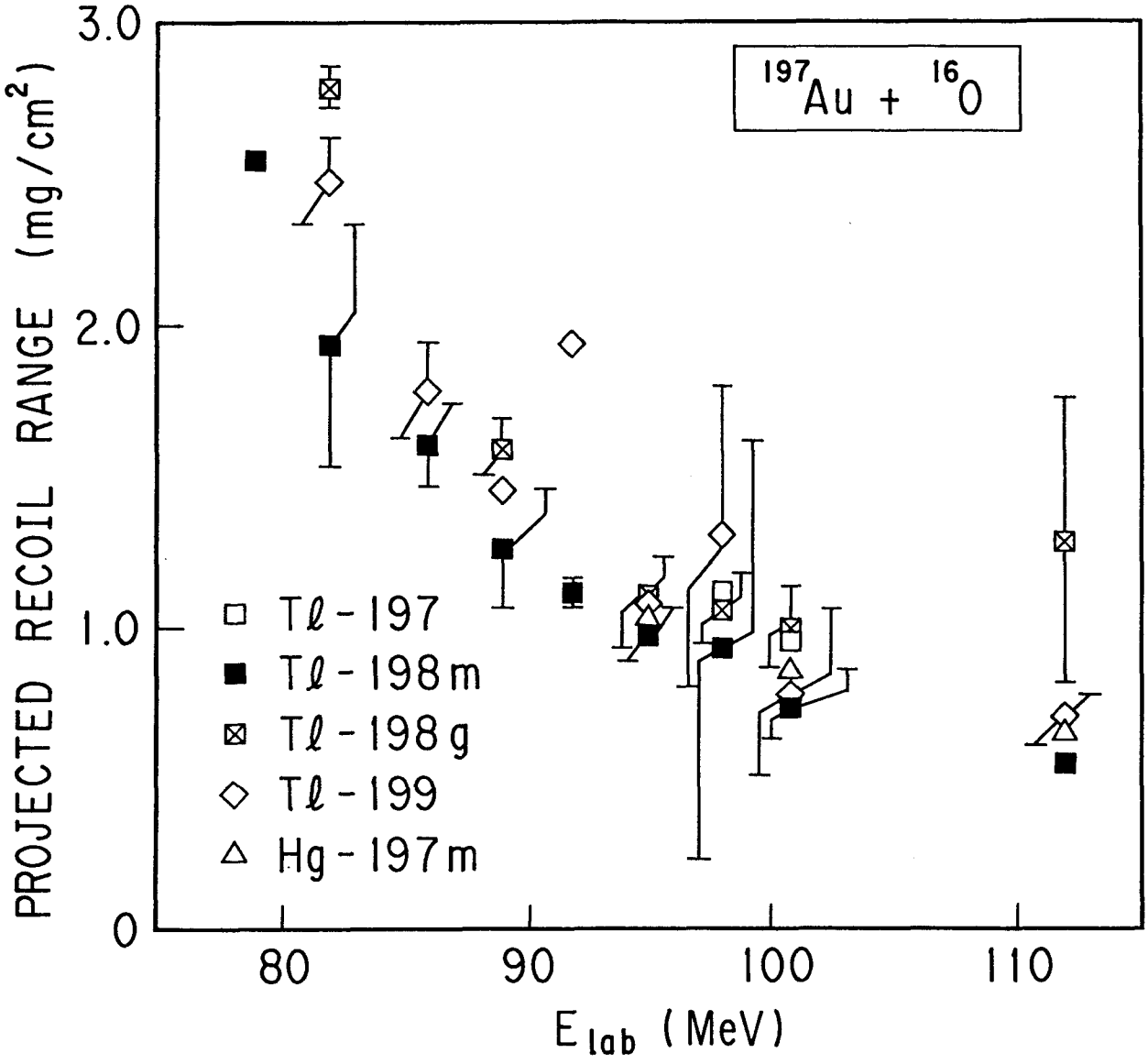

Fig.2.9. Mean projected recoil ranges of Tl and Hg nuclides in the ^{16}O-induced reaction.

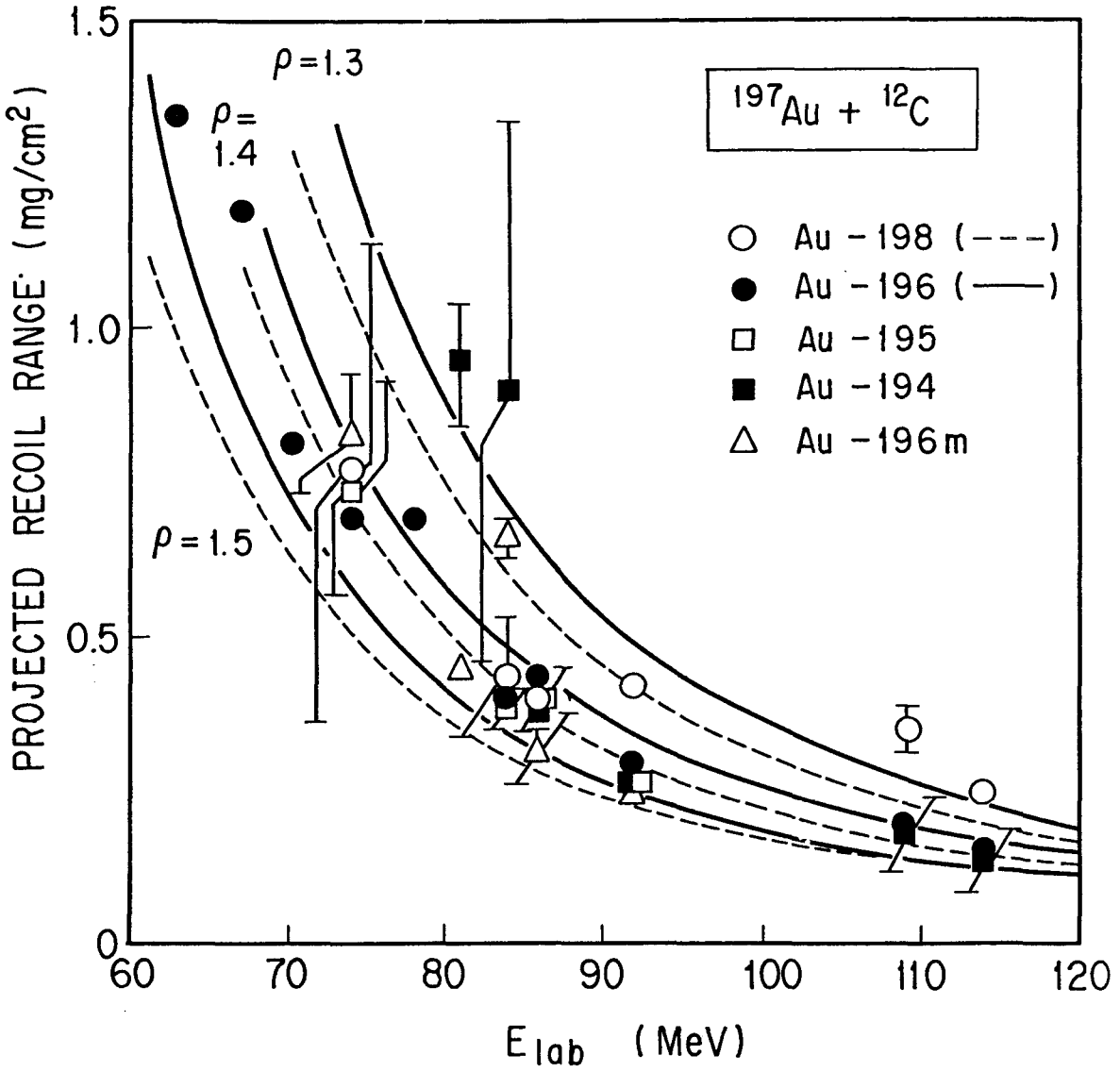

Fig.2.10. Mean projected recoil ranges of Au nuclides in the ^{12}C-induced reaction. Solid lines and dashed lines represent the calculated recoil ranges of ^{196}Au and ^{198}Au, respectively, for ρ = 1.3, 1.4, and 1.5. ρ gives the distance of the closest approach between two interacting nuclei expressed in unit of the sum of the nuclear radii. (see 2.4.2.)

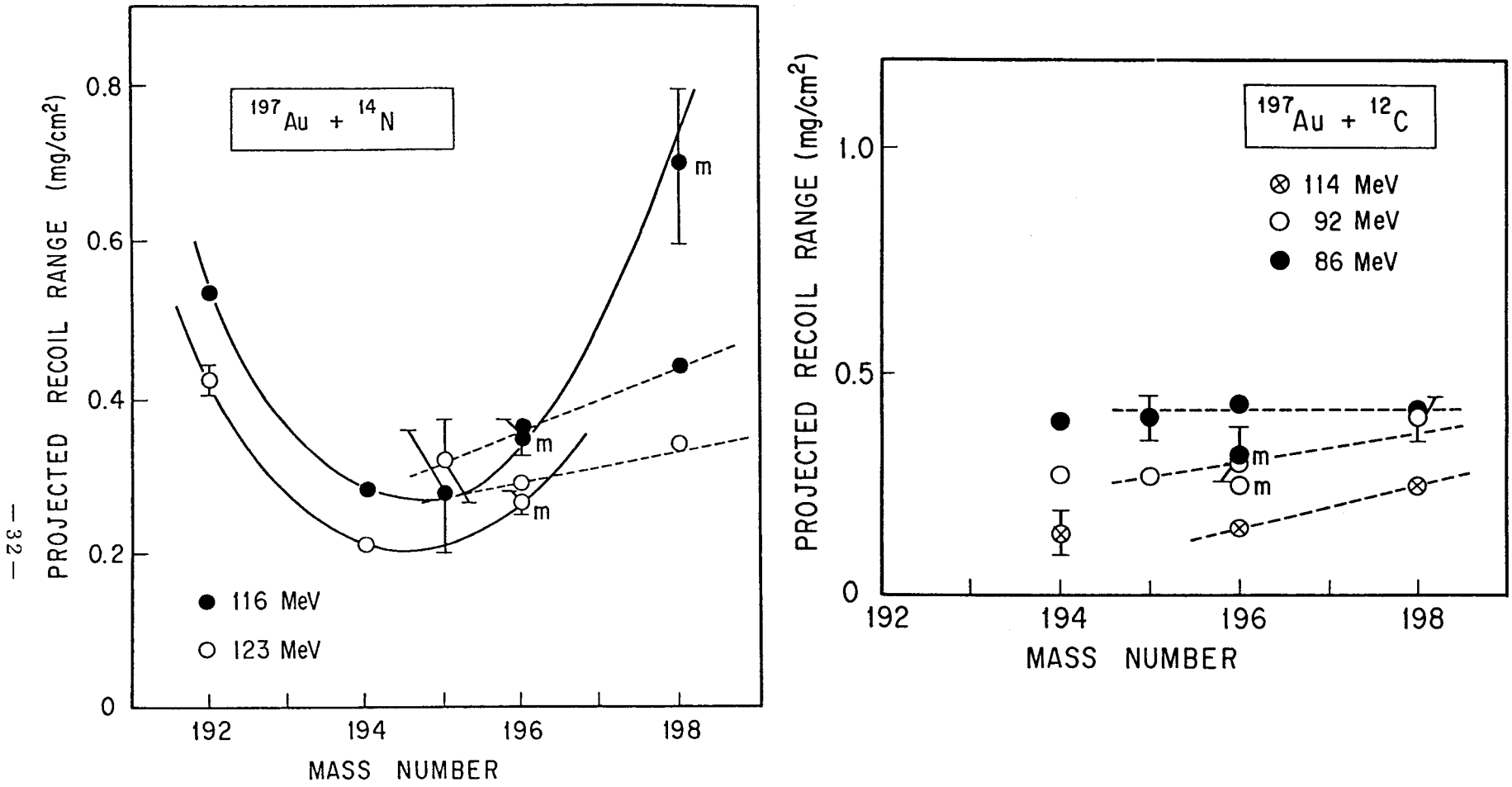

Fig.2.11. Mean projected recoil ranges as a function of mass number of Au nuclides in the ^{14}N- and ^{12}C-induced reactions. The bombarding energies were 116MeV and 123MeV for the ^{14}N-induced reaction and 86MeV, 92MeV, and 114MeV for the ^{12}C-induced reaction. According to the idea distinguishing products of QET and DIT in 2.4.1, dashed lines through recoil ranges of the isotopes produced by QET and solid lines through those of the isotopes produced by DIT are drawn.

Au with the mass numbers, 192, 194, 195, 196, 196m, 198, and 198m were measured in the ^{14}N-induced reaction, while the ranges of Au with the mass numbers, 194, 195, 196, 196m, and 198 were measured in the ^{12}C-induced reaction. The ranges of Au products except for 192 and 198m resemble each other in each reaction system.

2.4. DISCUSSION ON TARGET-LIKE PRODUCTS

2.4.1. Quasi-Elastic Transfer and Deep Inelastic Transfer Reactions in the Isotopic Distribution of Au

First I like to make an attempt distinguishing the reaction products associated with the quasi-elastic transfer reaction (QET) and those associated with the deep inelastic transfer reaction (DIT). These two reactions are important in the classification of transfer reactions [5]. In general, QET is noticeable in the reaction transferring at most a few nucleons, while up to several dozens of nucleons can be transferred in DIT. QET takes a trajectory near the Coulomb trajectory with minimum interaction and the projectile kinetic energy is little dissipated in QET in contrast to large energy dissipation in DIT [3,5]. The dissipation causes conversion of the orbital angular momentum into intrinsic spins of the composite system. Therefore high spin isotopes are likely to be produced in DIT.

The isotopic distribution of cross sections of gold production is tried to be explained with two Gaussian distributions as shown in Fig.2.12 for ^{37}Cl-, ^{16}O-, ^{14}N-, ^{12}C-induced reactions. Of the two Gaussians, one closer to the target mass number is characterized by a narrow width, and the other has a wider distribution composed of isotopes far from target and high spin metastable isotopes near the target mass. As given in Table 2.1, both of the ^{196m}Au and ^{198m}Au nuclides have spins of $12\hbar$ which are very large compared with spins of the other Au nuclides. As shown in Fig.2.12

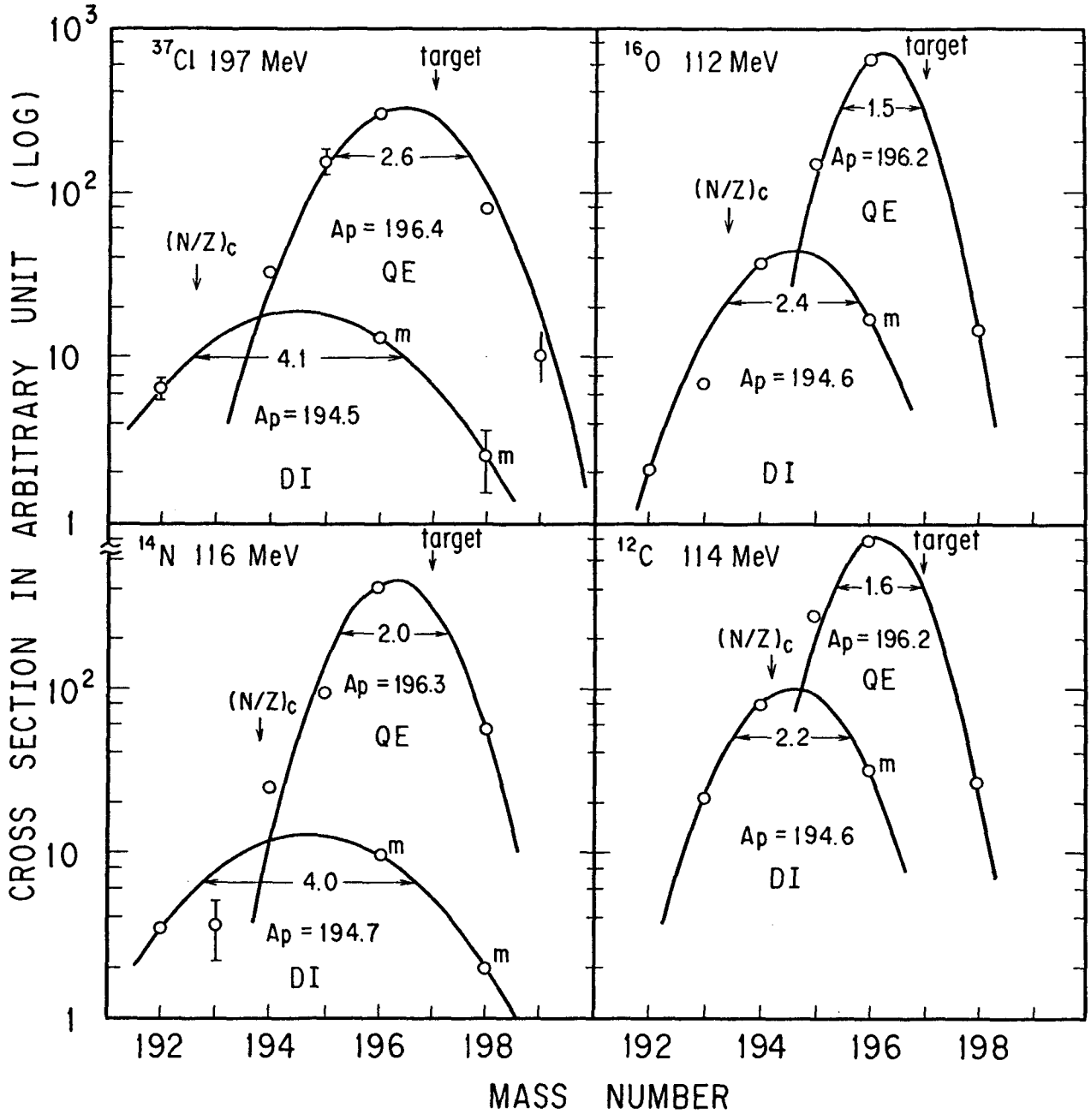

Fig.2.12. Mass distributions of Au products for the ^{37}Cl-, ^{16}O-, ^{14}N-, ^{12}C-induced reactions. Peak positions Ap and widths of the fitted two gaussian distributions drawn with solid lines are described in the figure. The target mass and a mass of the product which has the same N/Z value as the compound nucleus are noted with arrorws.

the experimental cross sections are satisfactorily reproduced. Peak positions of the wider distributions all lie near the N/Z value of the compound system. This shows accomplishment of charge equilibration found as one of the features of DIT. Equilibration of the N/Z value will be further discussed in 2.7.3. This method has been proposed by Kratz et al.[30] in ^{132}Xe-induced reaction on ^{197}Au. In Fig.2.13 the peak position and width of the Gaussian are plotted as a function of the incident energy devided by the Coulomb barrier of the respective reaction system for reactions ^{197}Au + ^{12}C, ^{14}N, ^{16}O, ^{37}Cl, and ^{132}Xe of [30]. It was found that both width and peak position of QET were nearly independent of the incident energy in the energy region of the present experiment. On the contrary, the peak position of DIT has a tendency of shifting to a lower mass number as the incident energy increases. This is an consequence of evaporation of more neutrons with increase of the excitation energy left in residual nuclei because of damping of the kinetic energy, which is a characteristic feature of DIT. The widths of DIT may be varied because of uncertainties of small yields of isotopes far from the target.

According to the classification of the products of QET and DIT in the previous paragragh, I drew dashed lines through recoil ranges of the isotopes produced by QET and a solid line through those of the isotopes produced by DIT in Fig.2.11. The figure shows that recoil ranges of the isotopes produced by DIT vary drastically with the mass number, while those of the isotopes produced by QET are similar to each other. This fact is considered to reflect the consequence that all the trajectories of QET producing these nuclides are close to the grazing trajectory of a particle

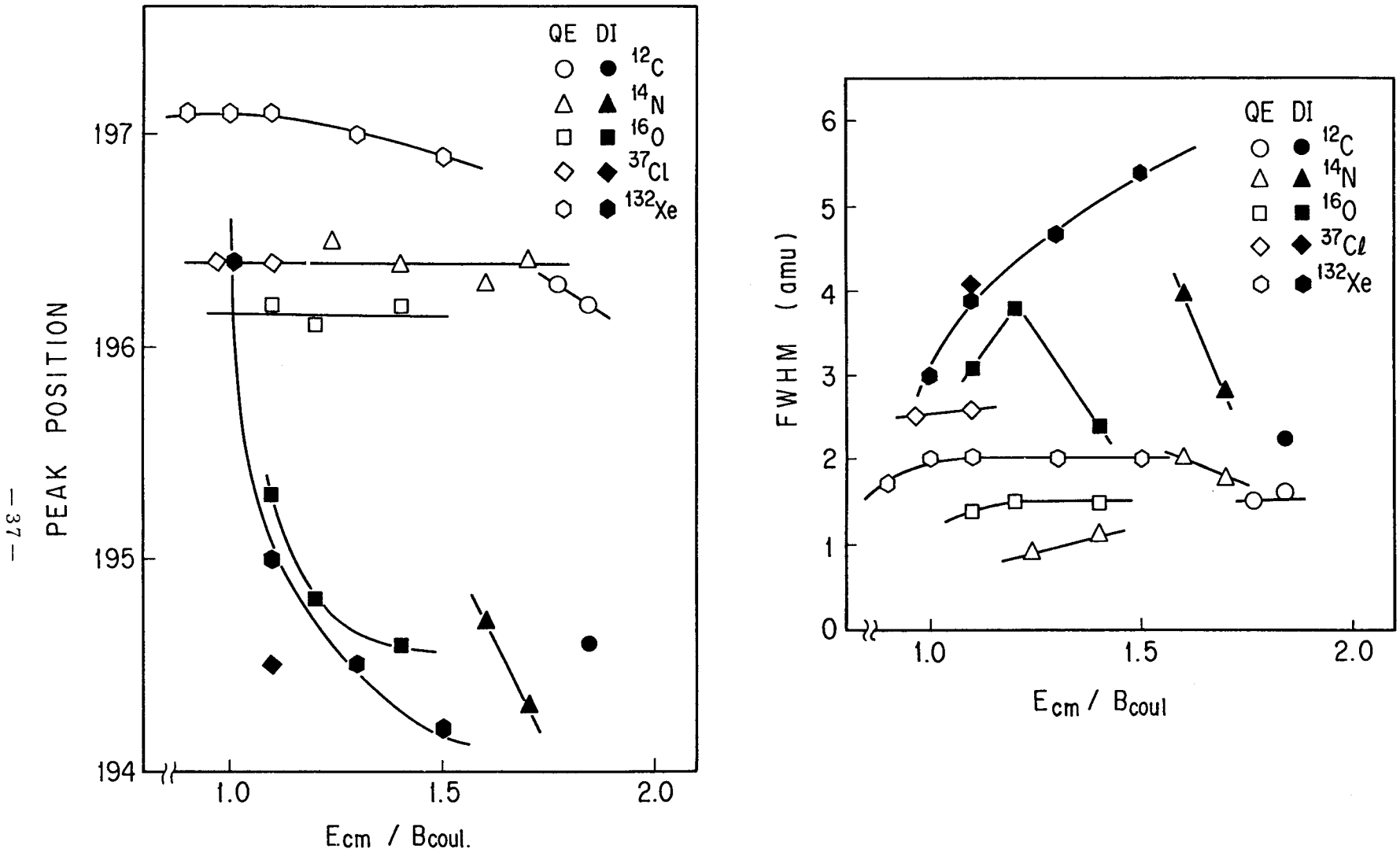

Fig.2.13. The peak position and width of the gaussian mass distribution as a function of the incident energy devided by the Coulomb barrier of the respective reaction system for the reactions ^{197}Au + ^{12}C, ^{14}N, ^{16}O, ^{37}Cl, and ^{132}Xe of [28]. Solid lines are drawn for a guide of the eye.

scattered elastically by the Coulomb force. Since the interaction time of DIT is longer than QET it causes a variation of the scattering angle of the products with the mass number, that is, a variation of the recoil ranges.

2.4.2. Characteristics of Quasi-Elastic Transfer Reaction of Au Isotopes

Figures 2.8 and 2.10 show projected recoil ranges of Au isotopes in the ^{16}O-induced and ^{12}C-induced reactions, respectively. Lines in Figs.2.8 and 2.10 represent the ranges calculated with the assumption that residual nuclei are scattered by the projectiles moving in the grazing trajectory. Recoil energy E_{recoil} and scattering angle θ_{gr} are calculated by the formulas [5]:

$$E_{recoil} = E_{cm} \frac{A_{TLP}\, A_P A_T}{A_P + A_T} \frac{1+\gamma^2+2\gamma\cos\theta_{gr}}{\gamma^2} \quad (\text{in MeV}) \tag{2.2}$$

where

$$\gamma = \left[\frac{A_P A_{TLP}}{A_T (A_P + A_T - A_{TLP})} \frac{E_{cm}}{E_{cm}+Q} \right]^{1/2}, \tag{2.3}$$

$$\theta_{gr} = 2\arcsin[B_{coul}/(2E_{cm} - B_{coul})] + \pi \qquad \text{(in radian in c.m.s)}, \tag{2.4}$$

and

$$B_{coul} = 1.44 Z_P Z_T / [\rho (A_P^{1/3} + A_T^{1/3})] \qquad \text{(in MeV)} \tag{2.5}$$

with atomic number Z and mass number A. The suffixes P, T, and TLP stand for projectile, target, and target-like product, respectively. E_{cm} is the projectile kinetic energy in c.m.s. ρ is a measure for the distance of the closest approach between two interacting nuclei expressed in unit of the sum of the nuclear radii. Q is the Q value for the transfer reaction from ground state to ground state. The calculated recoil energy is then converted into the projected range in the laboratory system by using the OSCAR code [23]. As shown in Figs.2.8 and 2.10, calculated recoil ranges can reproduce well experimental ones of ^{198}Au and ^{196}Au which are likely to be produced by QET according to the discussion in 2.4.1. Therefore these QET products are considered to be associated with the grazing trajectory.

2.4.3. Cross Section and Interaction Distance of the Quasi-Elastic Transfer Reaction

Several features of QET have been described in 2.4.1 and 2.4.2. Recoil range data of ^{16}O- and ^{12}C-induced reactions are converted into interaction

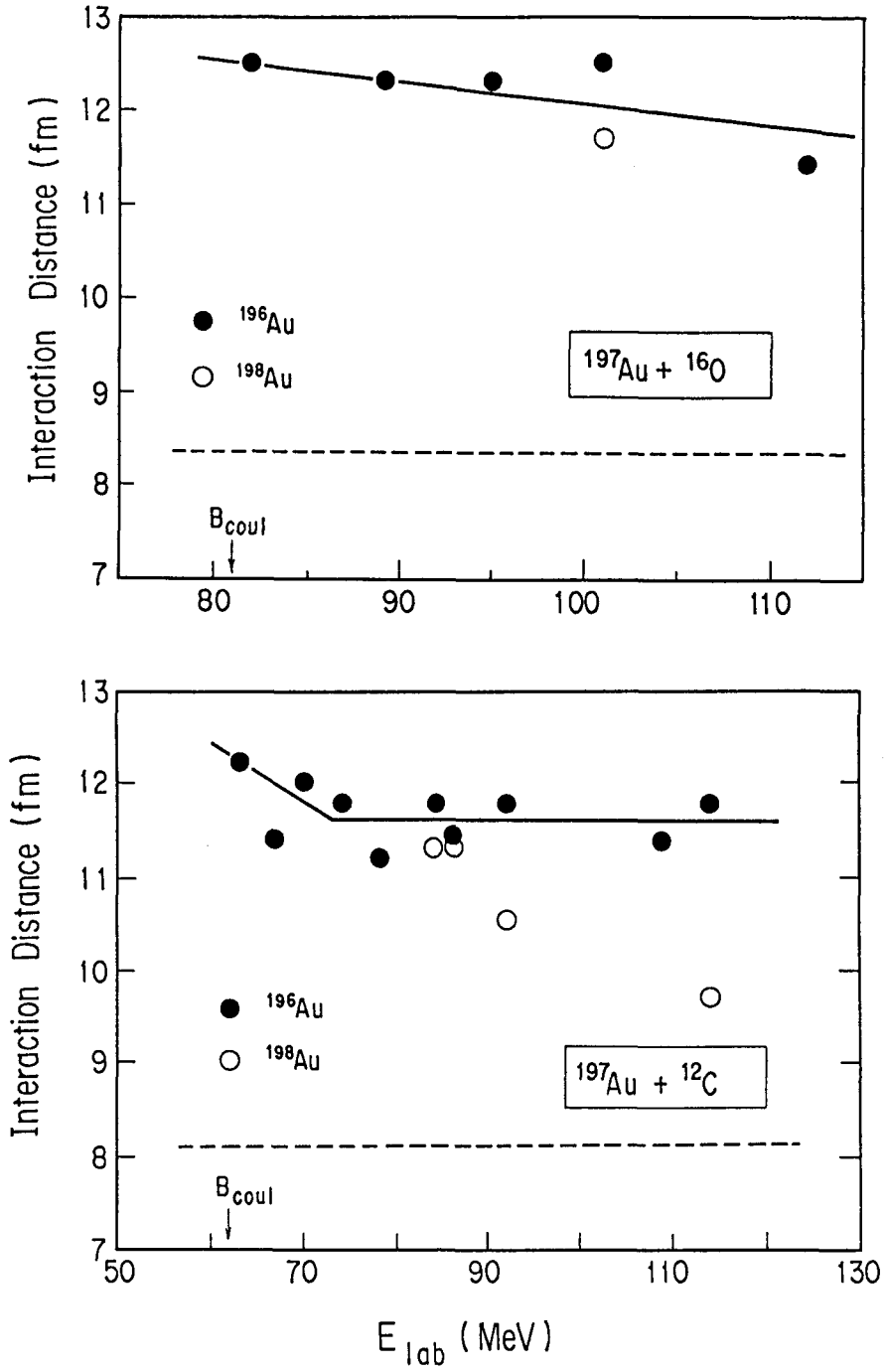

Fig.2.14. Interaction distances of quasi-elastic transfer for the ^{16}O- and ^{12}C-induced reactions by using the calculated results shown in the Figs.2.8 and 2.10. Solid lines are drawn to reproduce experimental values. Dashed lines represent size of the nuclear potential well. (see text)

distance R_{int} by using the calculated results shown in the Figs.2.8 and 2.10, which are depicted in Fig.2.14. The closest distances of the Coulomb repulsion are concluded to be between 11 and 13 fm in both of the systems, and it decreases slightly with increase of the incident energy. It means that QET may take place along a trajectory through a constant interaction distance independent of the incident energy. This is the reason why ratios of QET products are nearly constant in a wide range of the incident energy as shown in Figs.2.6 and 2.7 and they have a constant width for the Gaussian distribution drawn through their cross sections as shown in Fig.2.13.

The relation of cross sections of the QET products and the relevant interaction distance shall be discussed then by means of the obtained R_{int} values for ^{12}C-, ^{14}N-, ^{16}O-, and ^{37}Cl-induced reactions. The expression of tunneling penetration proposed for the neutron transfer reaction below Coulomb barrier [8,9] was assumed to be valid. In order to apply this model to the present systems in the energy range above the Coulomb barrier, I further put a postulate that interacting nuclei are deformed at the instant of collision and neutrons are excited to higher levels. Thus I can derive an expression of the ratio of cross sections of QET products as decribed below.

$$\frac{\sigma(^{197+x}Au)}{\sigma(^{196}Au)} = \exp\{-2\alpha_0 L[(V_P(xn) - xE_n)^{1/2} - (V_T(n) - E_n)^{1/2}]\} \quad (x = -2,1,2), \quad (2.6)$$

where

$$\alpha_0 = (2|x|m_n)^{1/2}/\hbar \qquad (2.7)$$

$$= 0.22\ \mathrm{MeV}^{-1/2}\mathrm{fm}^{-1}\ (\text{ for } x=1 \text{ as an example })$$

and

$$L = R_{int} - r_0(A_P^{1/3}+A_T^{1/3}) \qquad (2.8)$$

In the expression, x is the number of neutrons transferred from projectile to target, V the neutron separation energy, E_n the excitation energy of the neutron in the nuclear potential well due to nuclear deformation, m_n the neutron mass and L the width of the barrier or the separation between the surfaces. r_0 is a measure of the size of the well (see a schematic illustration in Fig.2.15). Calculated results were fitted to the cross section ratios by adjusting two parameters E_n and r_0. The E_n and r_0 which are 6.3MeV and 1.0fm, respectively, give the best fit to the data. The ratios of cross sections are able to be well reproduced for a variety of the projectiles and the absolute magnitudes except for $\sigma(^{199}\mathrm{Au})/\sigma(^{196}\mathrm{Au})$, calculated values for which are about tenth smaller than the experimental ones. Another reaction mechanism except for QET may contribute to the production of ^{199}Au although it could not be clarified in this study.

The size of the nuclear potential well is shown in Fig.2.14 with a dashed line. It shows that the closest distances of QET are between 3 and 4 fm apart from the well edge. This gap may exhibit the degree of deformation of the interacting nuclei or the length of the neck at the instant of

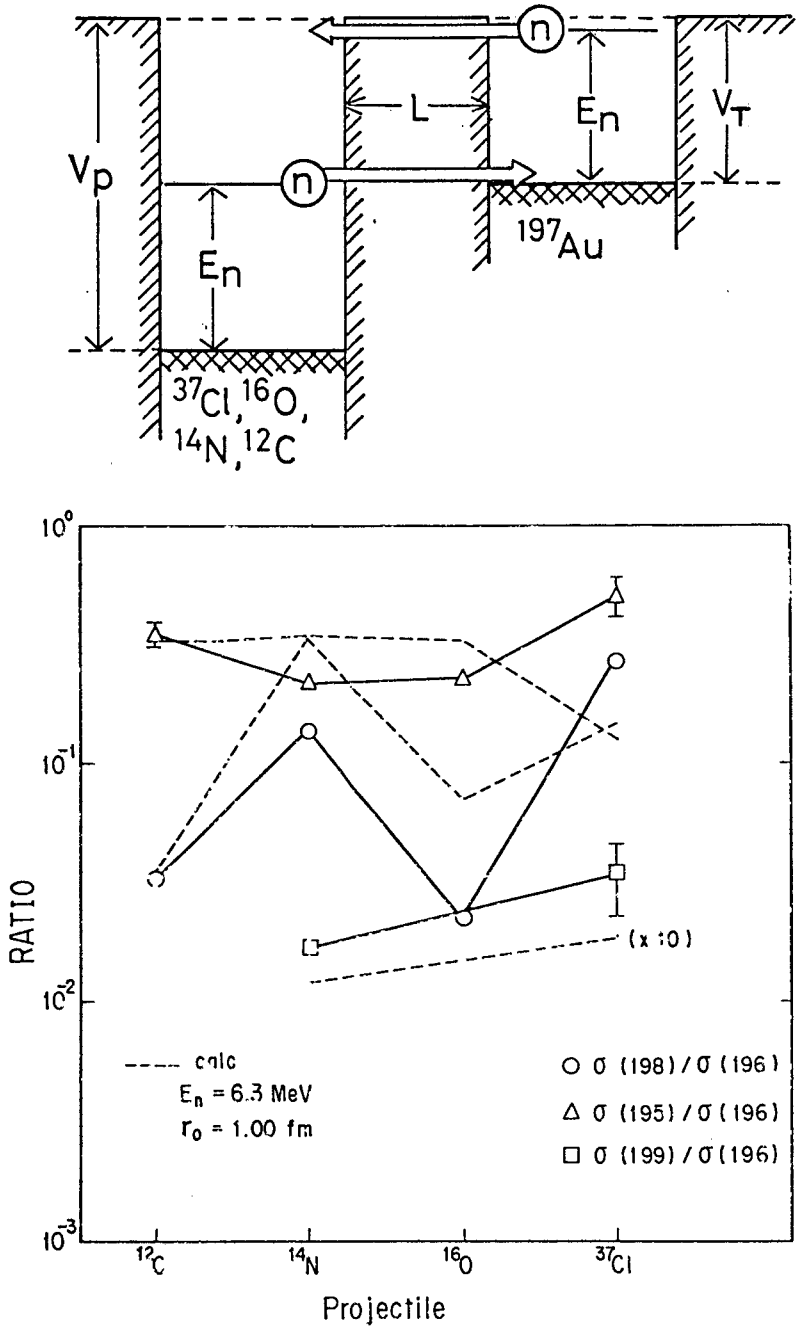

Fig.2.15. Cross section ratios of the quasi-elastic transfer products. Solid lines are drawn through the experimental values, while dashed lines represent the values calculated with a extended tunneling model. The model is illustrated schematically in the top. See text for the parameters E_n and r_0.

interaction.

2.5. EXPERIMENTAL OF COUNTER EXPERIMENT

2.5.1. Set-up in the Scattering Chamber

In-beam measurements during bombardment with ^{16}O-6.6MeV/u and ^{16}O-8.8MeV/u beams were performed in a 50cm diam. scattering chamber in the R-2 course described in 2.2.1. The set-up in the scattering chamber is drawn in Fig.2.16. The target of 1μm thick Au foil was placed at the center of the chamber. Beam of accelerated ions were adjusted with the magnets described in 2.2.1 to pass through an upstream slit of 2mm ϕ in the chamber. In order to focus the beam on the center at the target position, a quartz plate attached to the target holder was irradiated beforehand. Fluorescent light is emitted from the quartz plate irradiated with charged particles and a beam spot becomes visible. In the measurement the target was set at 45° or 90° with respect to the beam direction. One of the two angles was selected not to reduce solid angles of detectors. The beam intensity was monitored with a downstream Faraday cup (FC) as well as the activation method. Besides a Si(Au) semiconductor detector was fixed at 15° for use as a monitor counter which measures elastically scattered particles to know how many interactions of target nuclei and projectiles occur. Emitted particles were detected by a counter telescope consisting of a combination of 50μm thick ΔE and 1500μm thick E Si(Au) detectors. The solid angle of the effective area of the telescope was between 0.39msr and 4.4msr. The laboratory angles at which the measurement was performed ranged 16° through 90°. Explanation

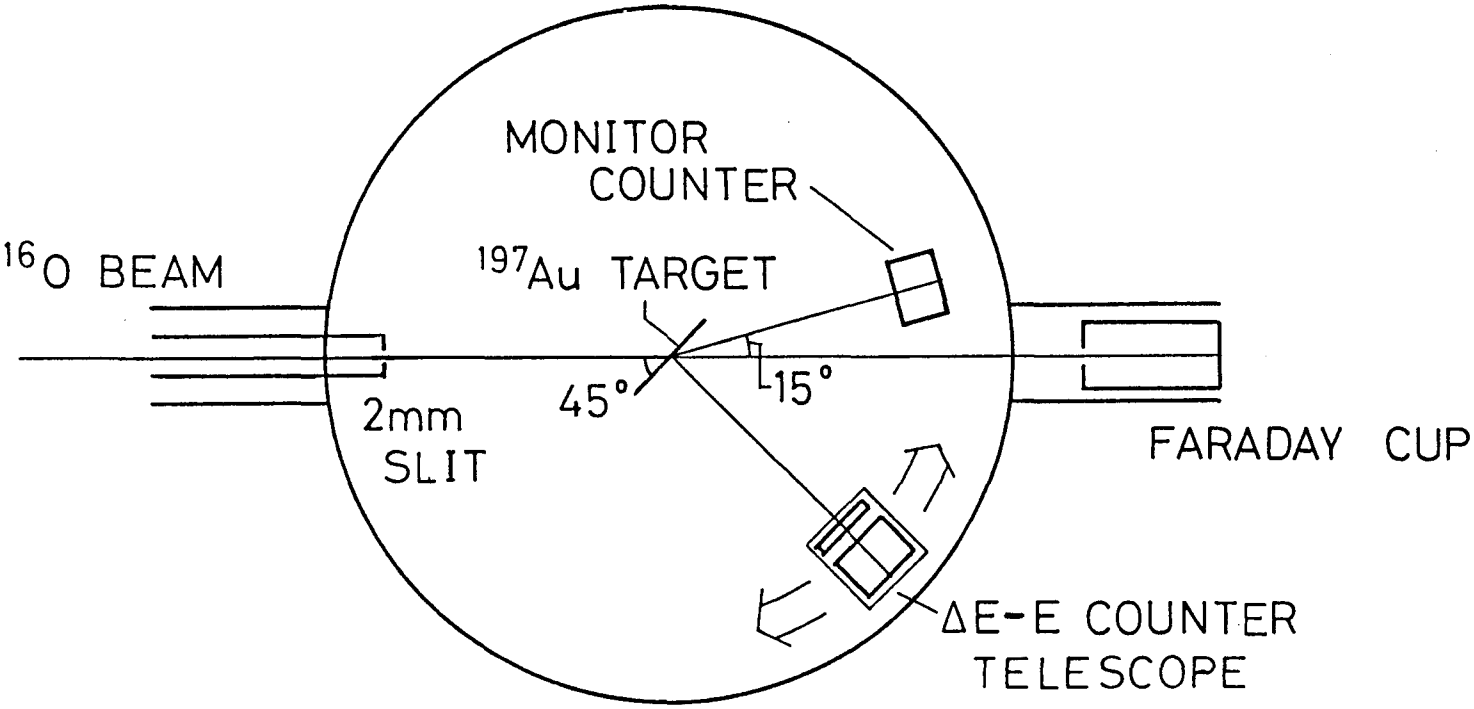

Fig.2.16. Experimental set-up in a 50cm diam. scattering chamber of the R-2 course for in-beam measurements.

of the counter telescope method will be given in 2.5.2.

2.5.2. Particle Identification by the ΔE-E Counter Telescope Method

The ΔE-E counter telescope method [31] is a supreme one for identifying emitted particles by means of stopping power dE/dx and kinetic energy E of the particles. The ΔE-E counter telescope consists of a thin transmission detector (ΔE detector) and a total absorption detector (E detector). Si(Au) semiconductor detectors were used as the detectors in the present study.

The principle of measurement of the semiconductor detectors is as follows. In the course of energy loss in the detector the projected high energy ion lifts electrons from the highest filled band, the valence band, to the conduction band and holes are created in the valence band. Lifted electrons and created holes move to the opposite directions to each other under the influence of an electric field, and when they reach electrodes generated is an electric pulse proportional to the depositted energy of particles. The energy resolution obtainable with the detectors are typically less than 1%.

Accordingly, stopping power dE/dx is measured as a specific energy loss ΔE by allowing the particles to pass through the ΔE detector thin compared to their ranges and recording the energy deposits in that detector. The rest energy E—ΔE of the particles is measured by stopping the particles in the E detector.

Stopping power of an energetic ion is related to the kinetic energy E, the mass m_i and the effective charge $z_i e$ of the ion. If kinetic energies of ions are small compared to their rest-mass energy ($\beta = v/c \ll 1$), the stopping power is formulated by Bohr [32] as follows.

$$-dE/dx = (4\pi z_i^2 e^4 NZ/mv^2) \ln(2mv^2/I)$$

$$= (2\pi e^4 NZ/m) \ln(2mv^2/I) (m_i z_i^2/E), \qquad (2.9)$$

where e and m are the charge and the mass of electron, respectively, v is the velocity of ion, N is the number of atoms per unit volume of the absorber, Z is the atomic number of the absorber, and I is the average energy to ionize the atom of the absorber. Accordingly, ions of different charges and masses with an equal energy can be distinguished by their stopping powers.

In Fig.2.17, the relation between the energy loss ΔE and the rest energy ($E - \Delta E$) calculated with the OSCAR code [23] is depicted for various elements. The figure demonstrates that the ΔE-E curves are clearly distinguishable not only between different elements but also between different isotopes of the same element.

2.5.3. Electronics for Measurement and Data Aquisition System

Figure 2.18 shows a block diagram of electronics including a ΔE-E

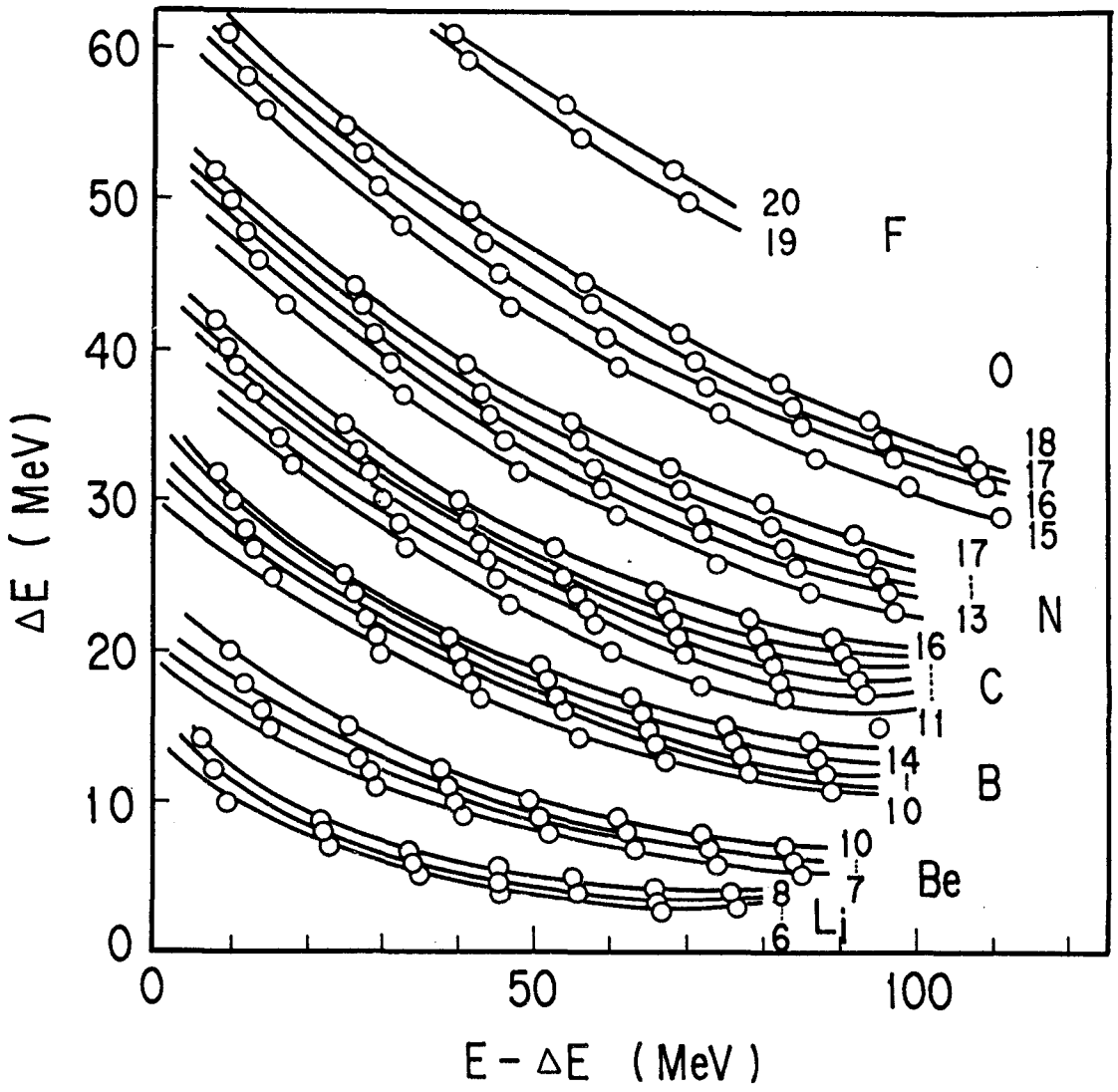

Fig.2.17. Map of energy loss ΔE and the rest energy (E—ΔE) of representative isotopes calculated with the OSCAR code [23]. Open circles represent the calculated values at the kinetic energies of 120MeV, 110MeV, 100MeV, etc. for F isotopes, those of 140MeV, 130MeV, 120MeV, etc. for O isotopes, those of 120MeV, 110MeV, 100MeV, etc. for N isotopes, those of 110MeV, 100MeV, 90MeV, etc. for C isotopes, those of 100MeV, 90MeV, 80MeV, etc. for B isotopes, those of 90MeV, 80MeV, 70MeV, etc. for Be isotopes, and those of 80MeV, 70MeV, 60MeV, etc. for Li isotopes. Solid lines are drawn through the calculated values.

counter telescope and a monitor counter for the in-beam measurement. The electronics system is made up of a circuit for fast-slow coincidence between timing signals from the ΔE detector and from the E detector.

Signal pulses from the ΔE detector and the E detector amplified were used as timing pulses and linear pulses as well. Event pulses were obtained by using the ΔE timing pulses as start signals and the E timing pulses as stop signals in a time-to-amplitude converter (TAC). Meanwhile the linear pulses from both of the detectors were further amplified with spectroscopy amplifiers. The coincidence between an event pulse and the relevant linear pulses was taken in a universal coincidence circuit. The linear pulses satisfying the coincidence were digitized with the analog-to-digital converters (ADC's) and the data were recorded event by event on magnetic tapes in the list mode with a VAX11 microcomputer furnished with a CAMAC system [33,34]. Counts of the ΔE, E and monitor detectors, and digitized pulses of a beam current integrator were monitored with scalers installed with a CAMAC system at the same time. The analysis of the data were carried out off-line using the same computer.

2.5.4. Analysis of Data

A two-dimensional map was constructed by the recorded list-mode data consisting of pairs of ΔE and $(E-\Delta E)$ values at each angle for the two incident energies. The map was parted into sections belonging to individual elements or isotopes as shown in Fig.2.19 with a stylus pen and a data

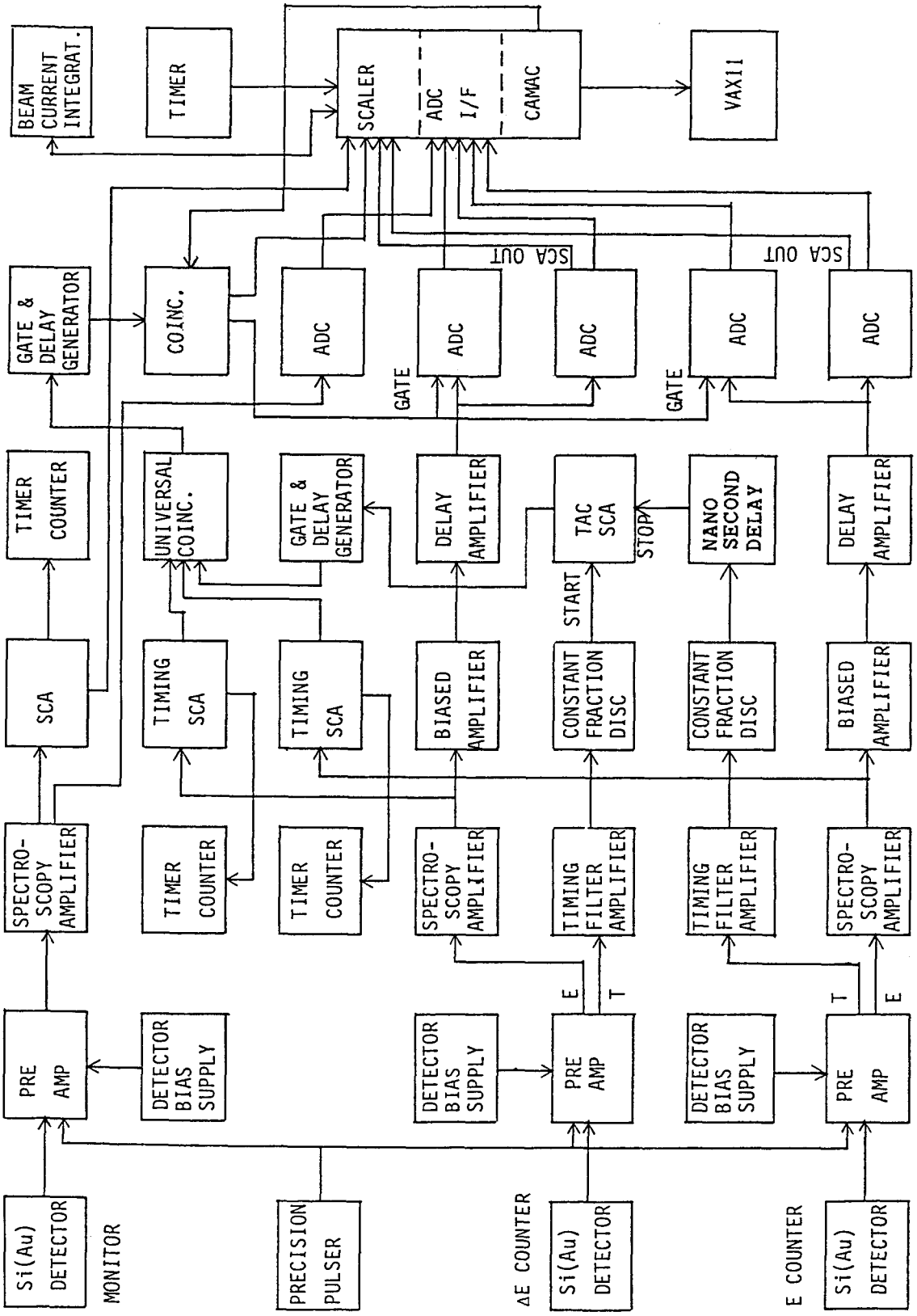

Fig.2.18. A block diagram of electronics including a Δ E-E counter telescope and a monitor counter for the in-beam measurement.

tablet on CRT display. According to the partition, the list-mode data were then sorted with the computer to construct an energy spectrum of each element or each isotope. The procedures described above were carried out by means of a data aquisition and analyzing system for the JAERI 20MV Tandem Accelerator [33,34].

Energy calibration of the energy spectra was done by using elastic peaks of ^{16}O particles. A typical calibration curve for the E detector is drawn in Fig.2.20. Corrections of energy loss of the target foil and the ΔE detector were taken into account in the calibration. In order to obtain the kinetic energy of projectile-like products, a correction for the energy loss was made for each element or each isotope by using the OSCAR code [23].

It has been pointed out that pulses from different heavy particles with an equal kinetic energy do not agree in its height. This effect is called the pulse height defect. It is, however, negligible in the region of atomic numbers up to about 16 [35]. The atomic number of the projectile-like products observed in the present study ranged from 3 through 9. Therefore the calibration curve obtained with oxygen can also be used for the other particles.

The laboratory energies E_{lab} at laboratory angles θ_{lab} were converted to center-of-mass energies E_{cm} at center-of-mass angles θ_{cm} by the formula based on the assumption of the two-body kinematics [36] as follows.

$$E_{cm} = \frac{A_P A_{PLP}}{(A_P+A_T)(A_P+A_T-A_{PLP})} E_P(1+\delta^2-2\delta\cos\theta_{lab})/\delta^2 \qquad (2.10)$$

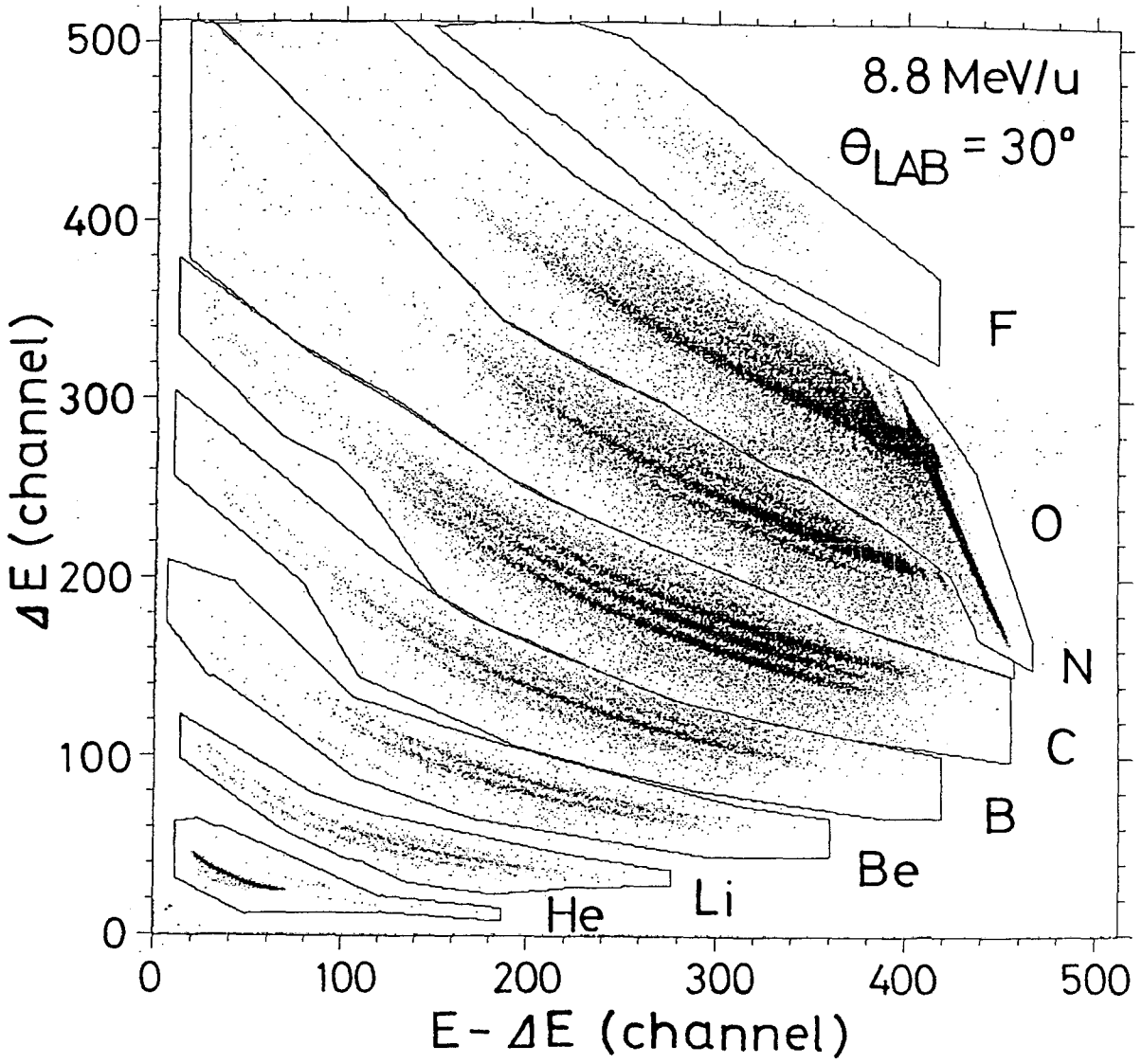

Fig.2.19. A typical (E—Δ E)-Δ E map of emitted particles measured at 30° in the laboratory system for the 8.8MeV/u ^{16}O-induced reaction.

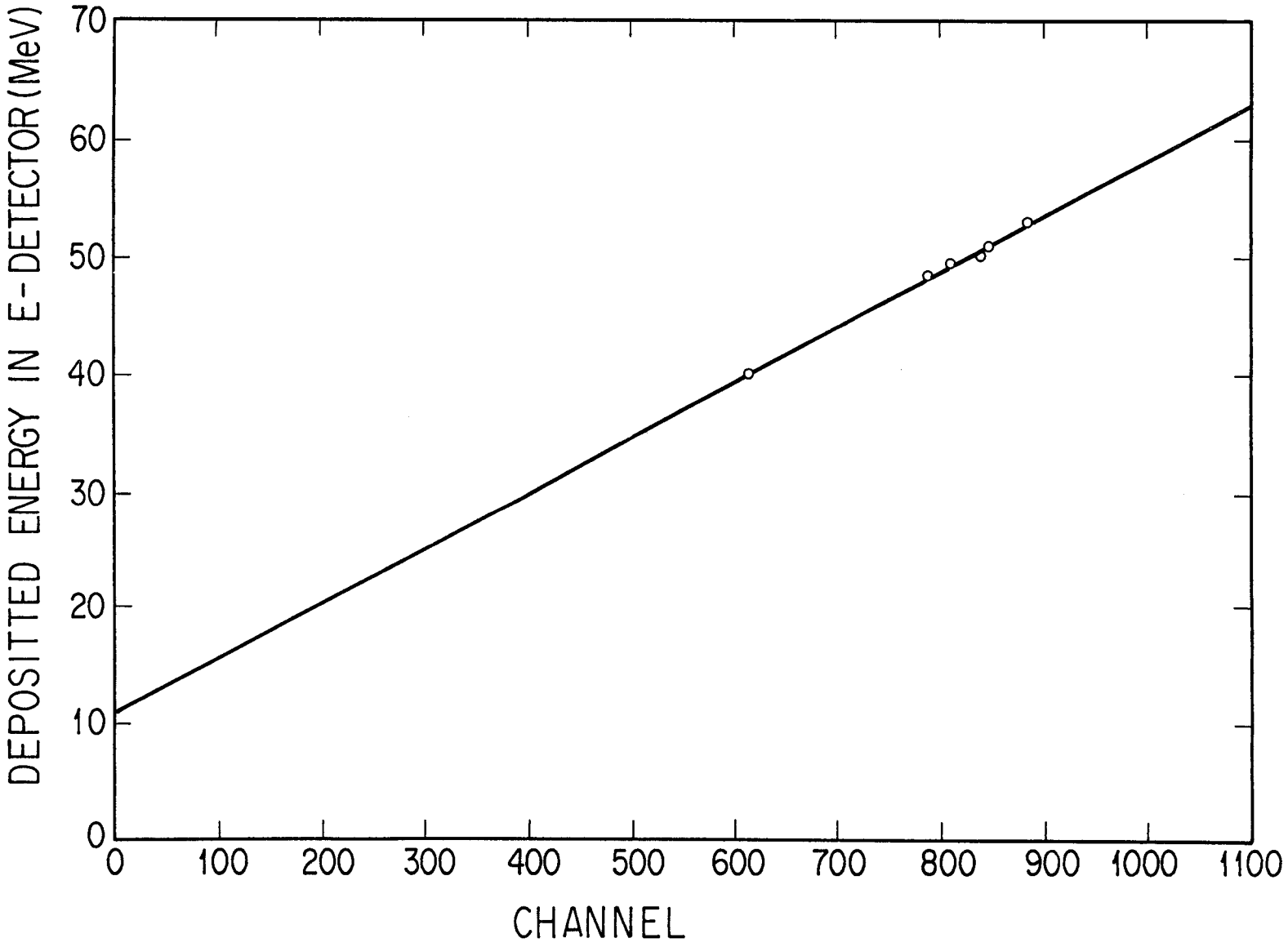

Fig.2.20. A typical calibration curve on energy for the E detector.

and

$$\sin\theta_{cm} = \sin\theta_{lab} \frac{\delta \cos\theta_{lab} \pm (1 - \delta \cos\theta_{lab})}{(1+\delta^2 - 2\delta \cos\theta_{lab})^{1/2}}, \qquad (2.11)$$

where

$$\delta = (A_P A_{PLP}/(A_P+A_T)^2 \, E_P/E_{lab})^{1/2}, \qquad (2.12)$$

A_P, A_T, and A_{PLP} represent masses of projectile, target, and projectile-like products, respectively, and E_P is the energy of projectile in the laboratory system.

The differential cross section at each angle was normalized through the elastic scattering cross section which was measured in detail and determined at the beginning of the experiment. The cross section of elastic scattering is calibrated by using the Rutherford scattering cross section at small angles where cross sections of elastic scattering agree with those of the Rutherford scattering. The differential cross section in the laboratory system $d\sigma/d\omega$ was converted to that in the center-of-mass system $d\sigma/d\Omega$ by the two-body-kinematics. The formula used for the conversion is as follows [36]:

$$d\sigma/d\Omega = (d\sigma/d\omega) \, | \, 1 - \delta \cos\theta_{lab} \, | \, (1+\delta^2 - 2\delta \cos\theta_{lab})^{1/2}. \qquad (2.13)$$

2.6. RESULTS OF THE COUNTER EXPERIMENT

2.6.1. Two-Dimensional Map for Particle Identification

Figure 2.19. shows a typical (E—ΔE)-ΔE map of emitted particles measured at 30° in the laboratory system. One can easily distinguish each nuclide of projectile-like products as mentioned in 2.5.2. Identification of each element is easily done owing to a strong elastic peak of ^{16}O appearing in the top-right corner of the map. It enables us to identify eight groups parted with solid curves as He through F as shown in the figure. An extraordinary component of the elastic scattering oxygen which shows an unusual ΔE-E dependence may be due to non-uniformity of the depth of the ΔE counter.

Identification of mass numbers is performed as follows. The lines of O group are easily identified owing to the line through elastic peak of ^{16}O. In order to indentify mass numbers of the other elements, I relied on a well-known relationship that a reaction product of a larger Q_{gg} value tends to be produced more preferentially in each element. Q_{gg} is the Q value of a reaction from ground state to ground state. The relationship is called Q_{gg} dependence, which is discussed in 2.7.3. in detail. This has been found in the same reaction system at a similar energy region. By taking the relationship into consideration, the lines seen in the map were identified as ^{20}F, ^{19}F, ^{18}O, ^{17}O, ^{16}O, ^{15}O (weak), ^{17}N, ^{16}N, ^{15}N, ^{14}N, ^{13}N (weak), ^{16}C (weak), ^{15}C, ^{14}C (strong), ^{13}C (strong), ^{12}C (strong), ^{11}C, ^{14}B, ^{13}B, ^{12}B,

^{11}B (strong), ^{10}B, ^{10}Be, ^{9}Be, ^{7}Be (weak), ^{8}Li, ^{7}Li, and ^{6}Li in the order of magnitude of energy loss in the ΔE detector. As for Be, defect of a line of ^{8}Be splitting into two α particles at the instant of production can be a guide of identification. Although He particles were observed, the lower energy region of He spectra was discriminated due to a certain threshold existing in the detecting system. The resulting He spectra are consequently insufficient to be competent for the discussion.

2.6.2. Angular Distributions of Elastic Scattering in the 6.6MeV/u and 8.8MeV/u ^{16}O-Induced Reactions on ^{197}Au

The angular distribution of elastic scattering tells us total reaction cross section σ_R and angular momentum ℓ_{gr} of the grazing reaction as follows. Total reaction cross section σ_R is expressed with a sum of partial reaction cross sections for orbital angular momenta ℓ weighted by transmission coefficient T_ℓ.

$$\sigma_R = \pi \lambda\!\!\!^{-2} \sum_{\ell=0}^{\infty} (2\ell+1) T_\ell \qquad (2.14)$$

where $\lambda\!\!\!^{-}$ ($= \lambda/2\pi$) is de Broglie wave length of relative motion divided by 2π. ℓ_{gr} is obtained as angular momentum at which T_ℓ is 0.5. Therefore ℓ_{gr} and σ_R are calculated with the T_ℓ's.

In order to obtain transmission coefficients fitting to the experimental angular distribution were performed by the ELASTII code [37] which uses a potential consisting of the Woods-Saxon nuclear potential V_N and the Coulomb potential V_C:

$$V(r) = V_N(r)+V_C(r)$$

$$V_N(r) = -V\{1+\exp[(r-R_R)/a_R]\}^{-1} - iW\{1+\exp[(r-R_I)/a_I]\}^{-1}$$

$$V_C(r) = Z_P Z_T e^2/(2R_C)(3-r^2/R_C^2) \quad \text{for } r \leqq R_C$$

$$= Z_P Z_T e^2/r \quad \text{for } r > R_C, \qquad (2.15)$$

where $R_R = r_R(A_P^{1/3}+A_T^{1/3})$, $R_I = r_I(A_P^{1/3}+A_T^{1/3})$, and $R_C = 1.2(A_P^{1/3}+A_T^{1/3})$. Fitting was performed with six optical parameters V, r_R, a_R, W, r_I, a_I to reproduce the cross sections of elastic scattering. Fitted curves are drawn in the Figs.2.21 and 2.22 together with experimental values. The optical parameters determined by the fits are given in Table 2.3. The values of ℓ_{gr} and σ_R were obtained as a result of the analysis for two projecting energies and presented in the same table. These values are used in the following data analysis and discussions of the reaction mechanism.

2.6.3. Angular Distributions of Projectile-like Products in the ^{16}O-

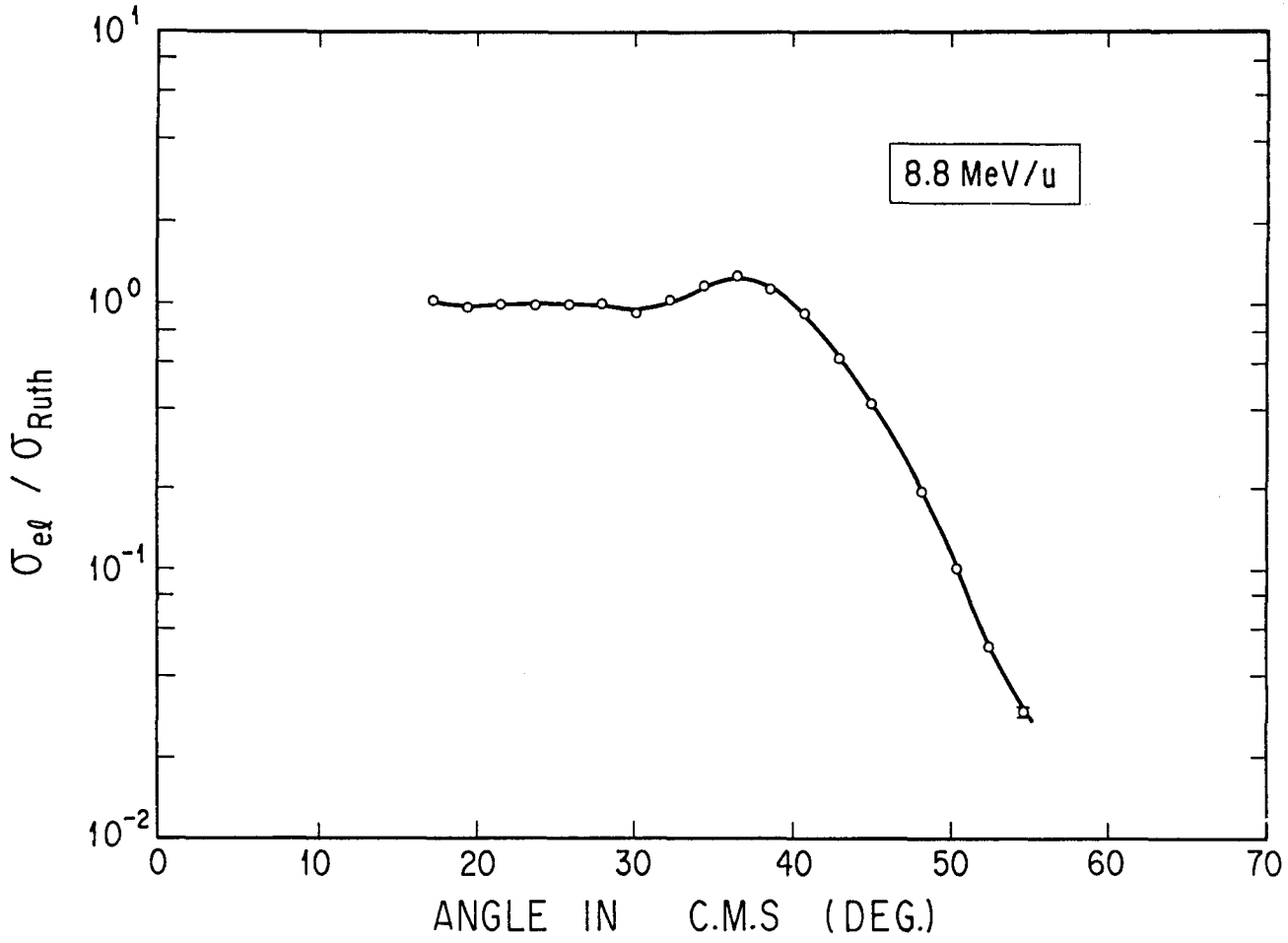

Fig.2.21. Angular distribution of elastic scattering for the 8.8MeV/u ^{16}O-induced reaction. Yields are plotted as relative values to cross sections of Rutherford scattering. A curve calculated with the ELASTII code is drawn in the figure.

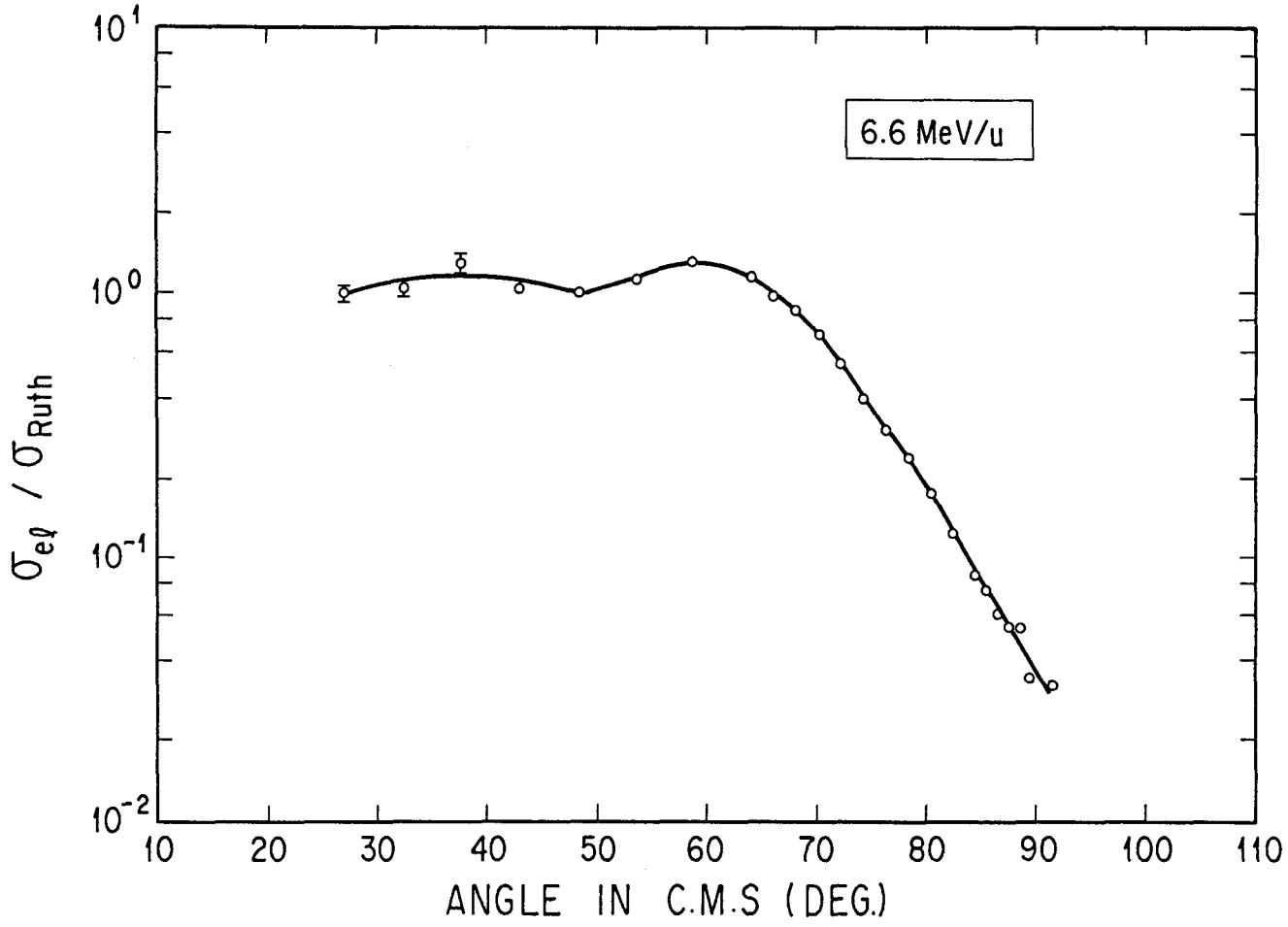

Fig.2.22. Same as Fig.2.21 but for the 6.6MeV/u ^{16}O-induced reaction.

Table 2.3. Nuclear potential parameters and total reaction cross section deduced from them.

$^{197}Au+^{16}O$	V (MeV)	r_R (fm)	a_R (fm)	W (MeV)	r_I (fm)	a_I (fm)	$\ell_{gr}(\hbar)$	σ_R (mb)
8.8MeV/u	46.8	1.14	0.823	19.2	1.20	0.499	75	2032
6.6MeV/u	47.6	1.17	0.694	10.5	1.28	0.400	49	1166

Induced Reactions

Angular distributions of elements except for O are shown for two projecting energies in Fig.2.23. Errors shown in the figures are due to statistical errors. The products at 8.8MeV/u exhibit a characteristic distribution of forward peaking, while those at 6.6MeV/u are distributed over a wide range of the angle as a general feature. Elements adjacent to projectile element show features somewhat different from the other elements.

Angular distributions of isotopes measured at 8.8MeV/u are shown in Figs.2.24-2.30. Forward-peaking angular distributions with a characteristic side-peaking which is the most prominant for ^{17}O (Fig.2.25) and ^{15}N (Fig.2.26) gradually changes to a more and more structureless distribution as the number of nucleons transferred increases.

2.6.4. Kinetic Energy Spectra of Projectile-like Products in the ^{16}O-Induced Reactions

Inclusive energy spectra of elements observed at 40° in the laboratory system are shown for the 8.8MeV/u ^{16}O-induced reaction as examples in Figs.2.31-2.37. One can see a narrow peak at a energy position lower than the elastic peak in the O spectrum in Fig.2.32 and at the higher energy region in the N spectrum in Fig.2.33 as well. There appears also a broad peak at an even lower energy region which exhibits essentially the same

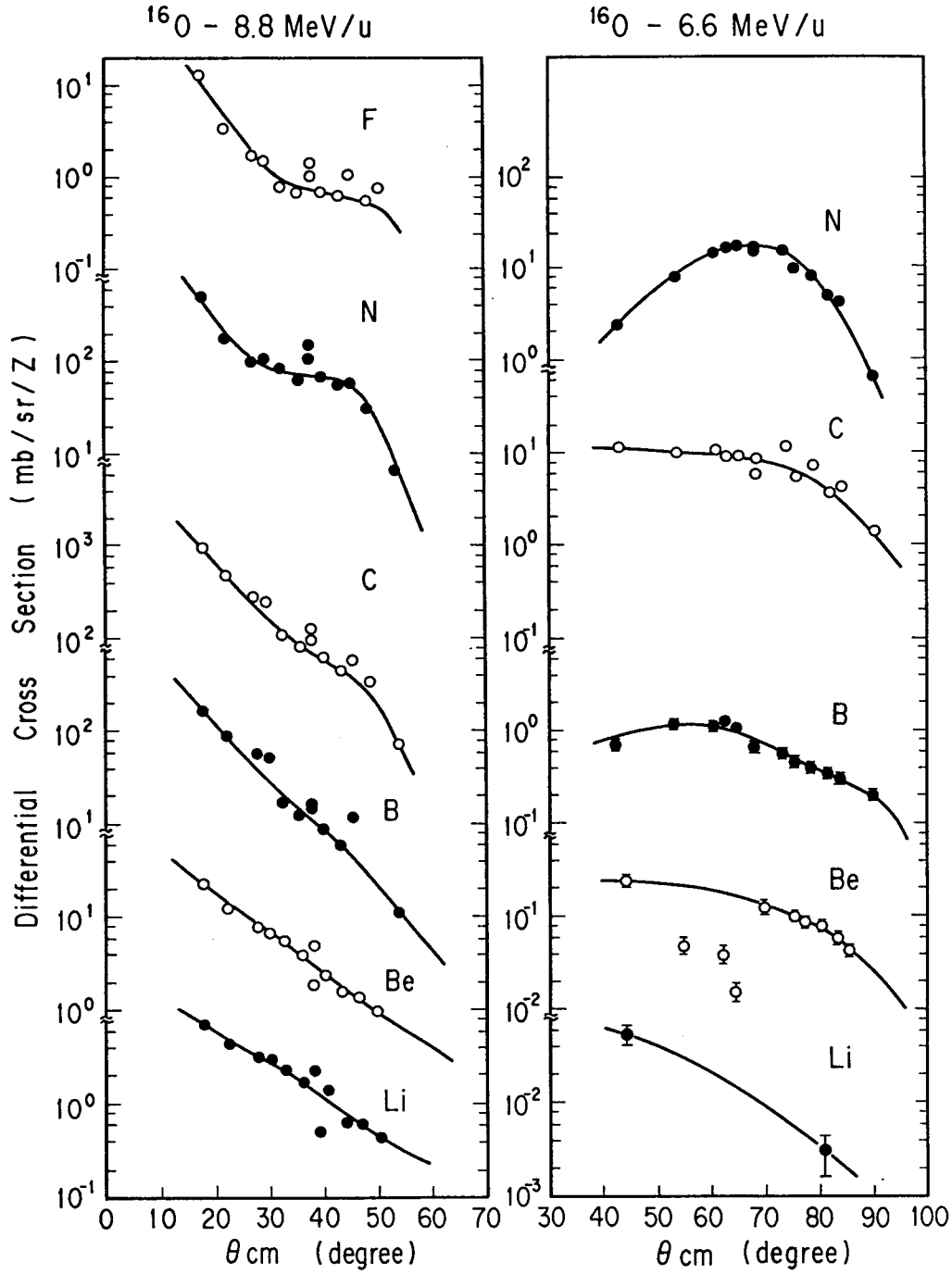

Fig.2.23. Angular distributions of elements of F, N, C, B, Be, and Li for the 8.8MeV/u and the 6.6MeV/u ^{16}O-induced reaction. Errors seen in the figure are due to statistical errors. Solid lines are drawn for a guide of the eye.

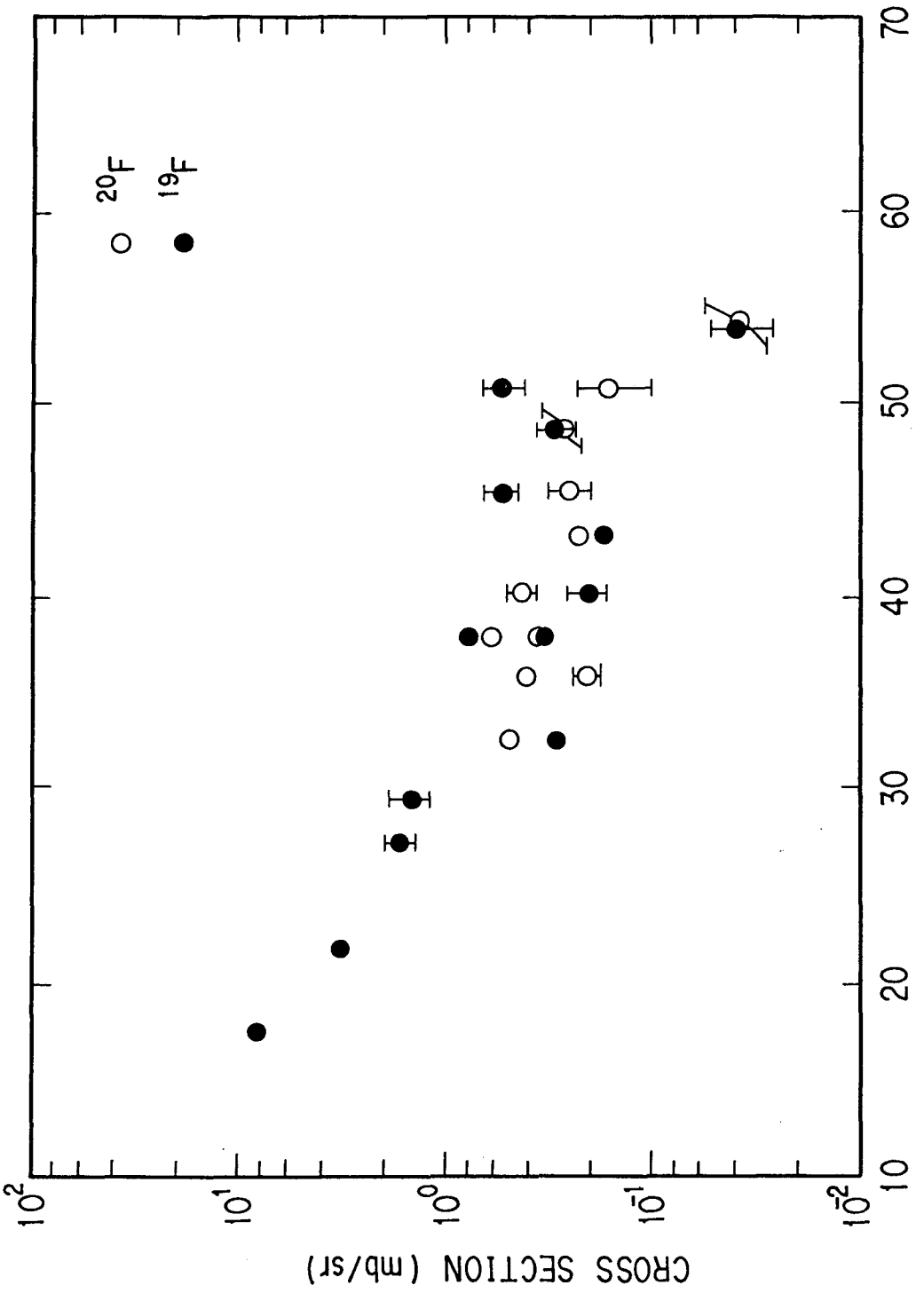

Fig.2.24. Angular distributions of F isotopes for the 8.8MeV/u ^{16}O-induced reaction.

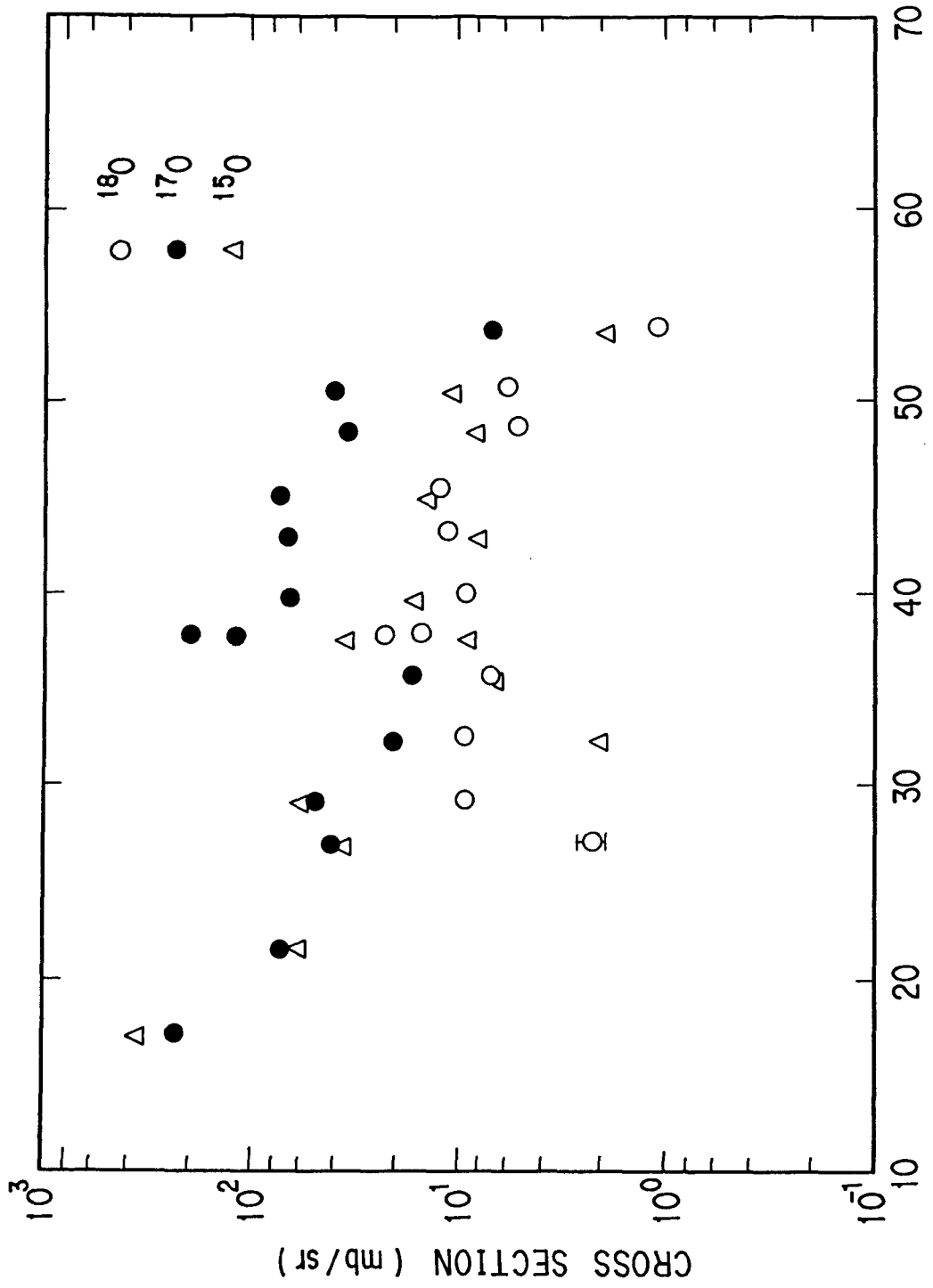

Fig.2.25. Angular distributions of O isotopes for the 8.8MeV/u ^{16}O-induced reaction.

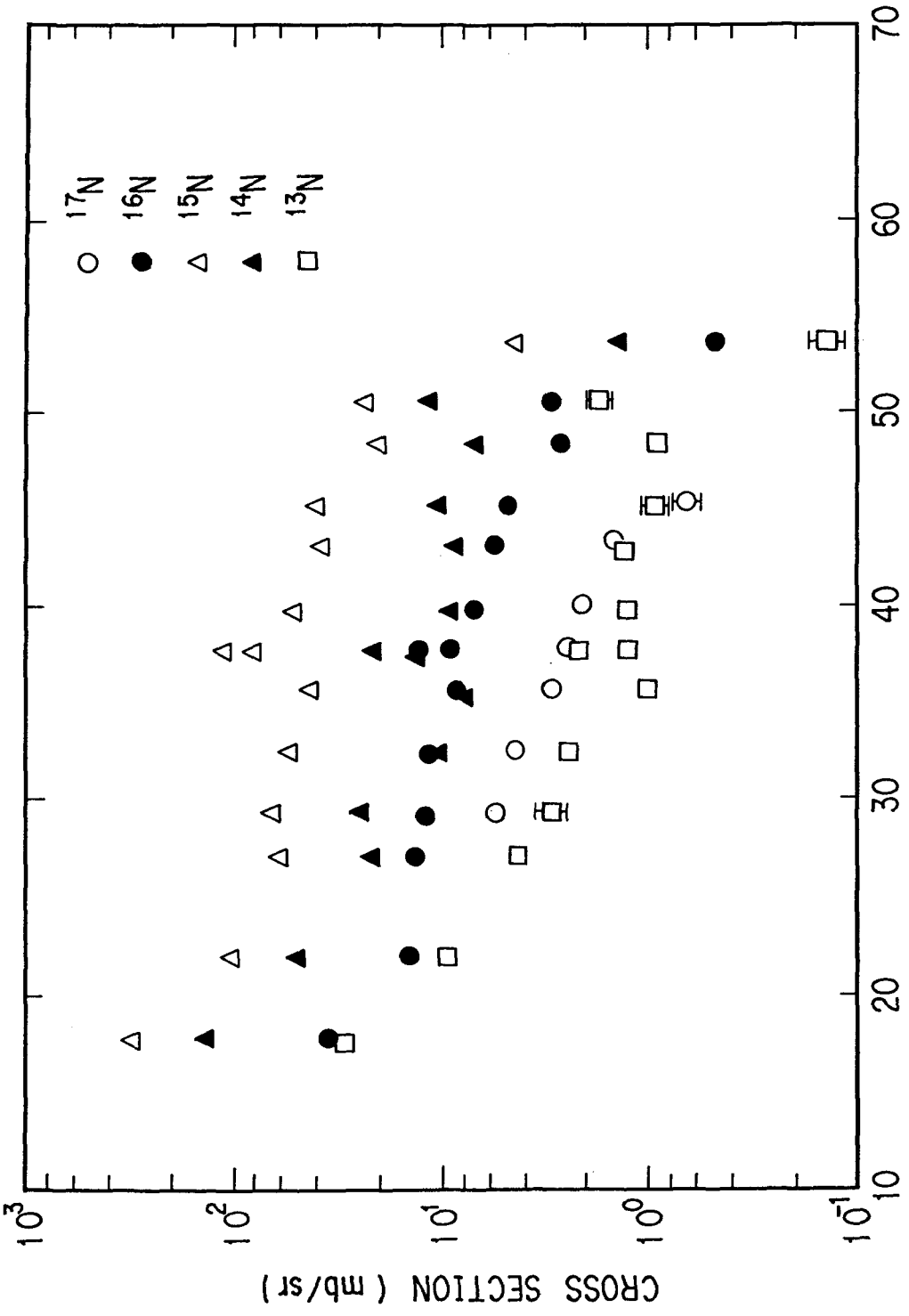

Fig.2.26. Angular distributions of N isotopes for the 8.8MeV/u ^{16}O-induced reaction.

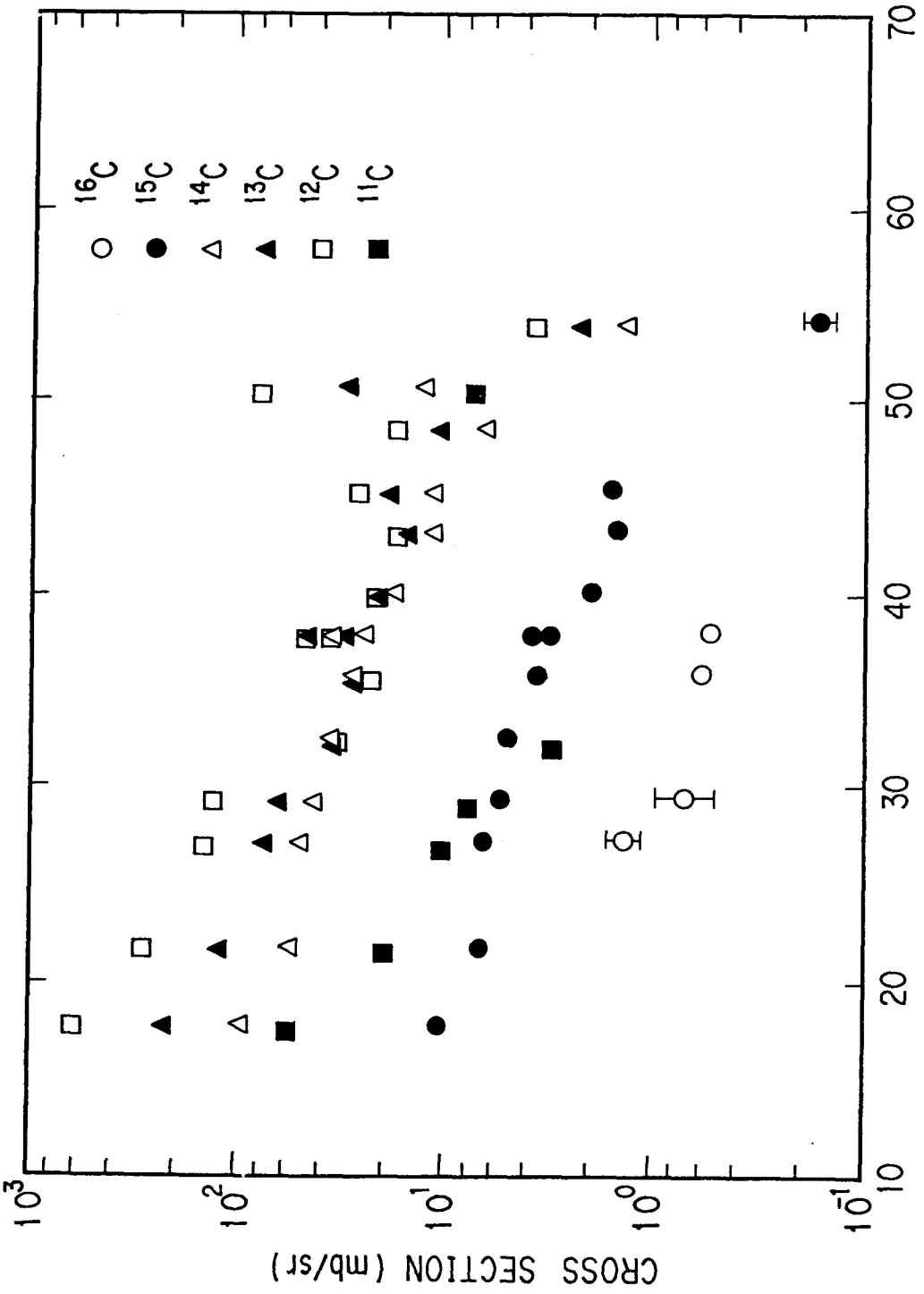

Fig.2.27. Angular distributions of C isotopes for the 8.8MeV/u ^{16}O-induced reaction.

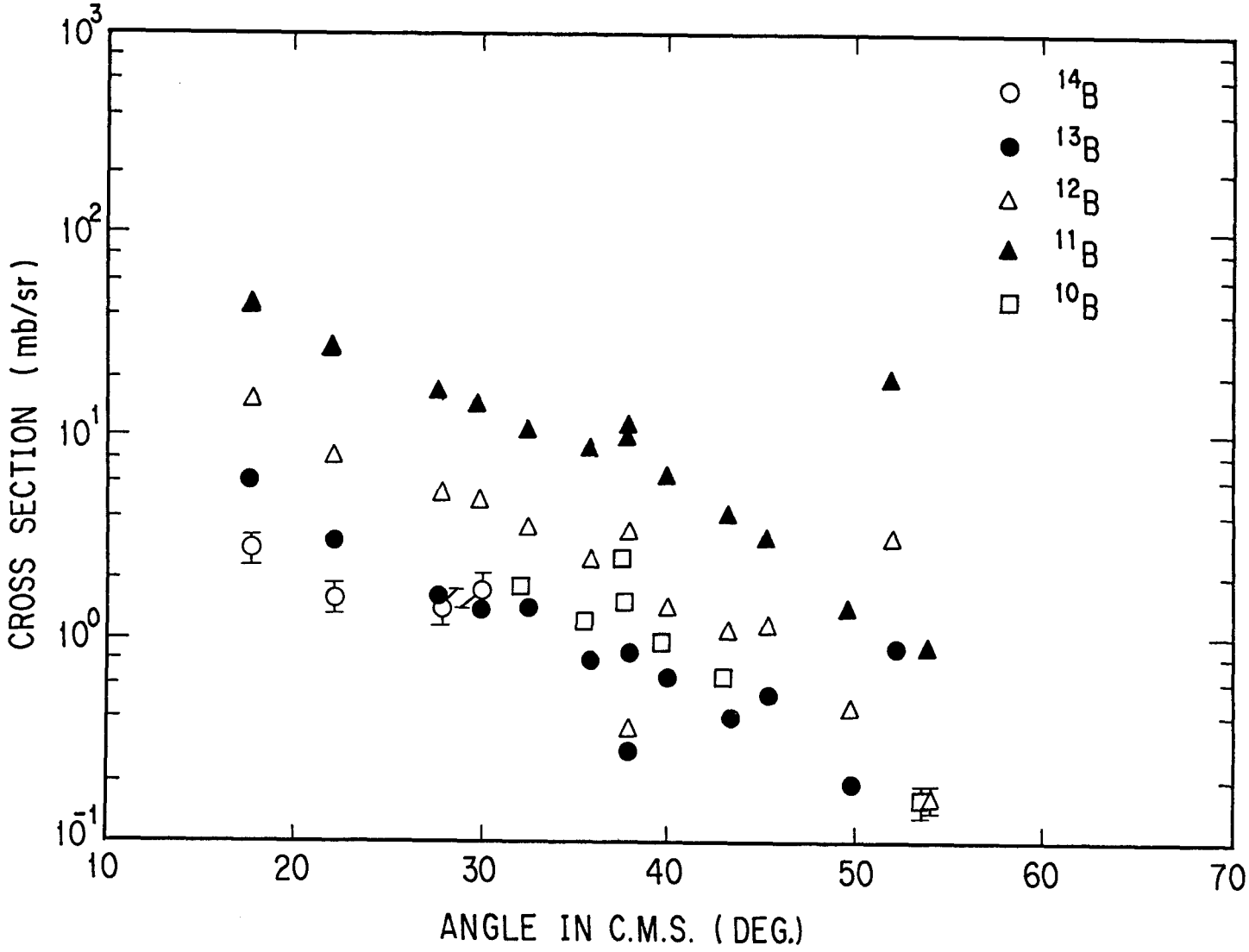

Fig.2.28. Angular distributions of B isotopes for the 8.8MeV/u ^{16}O-induced reaction.

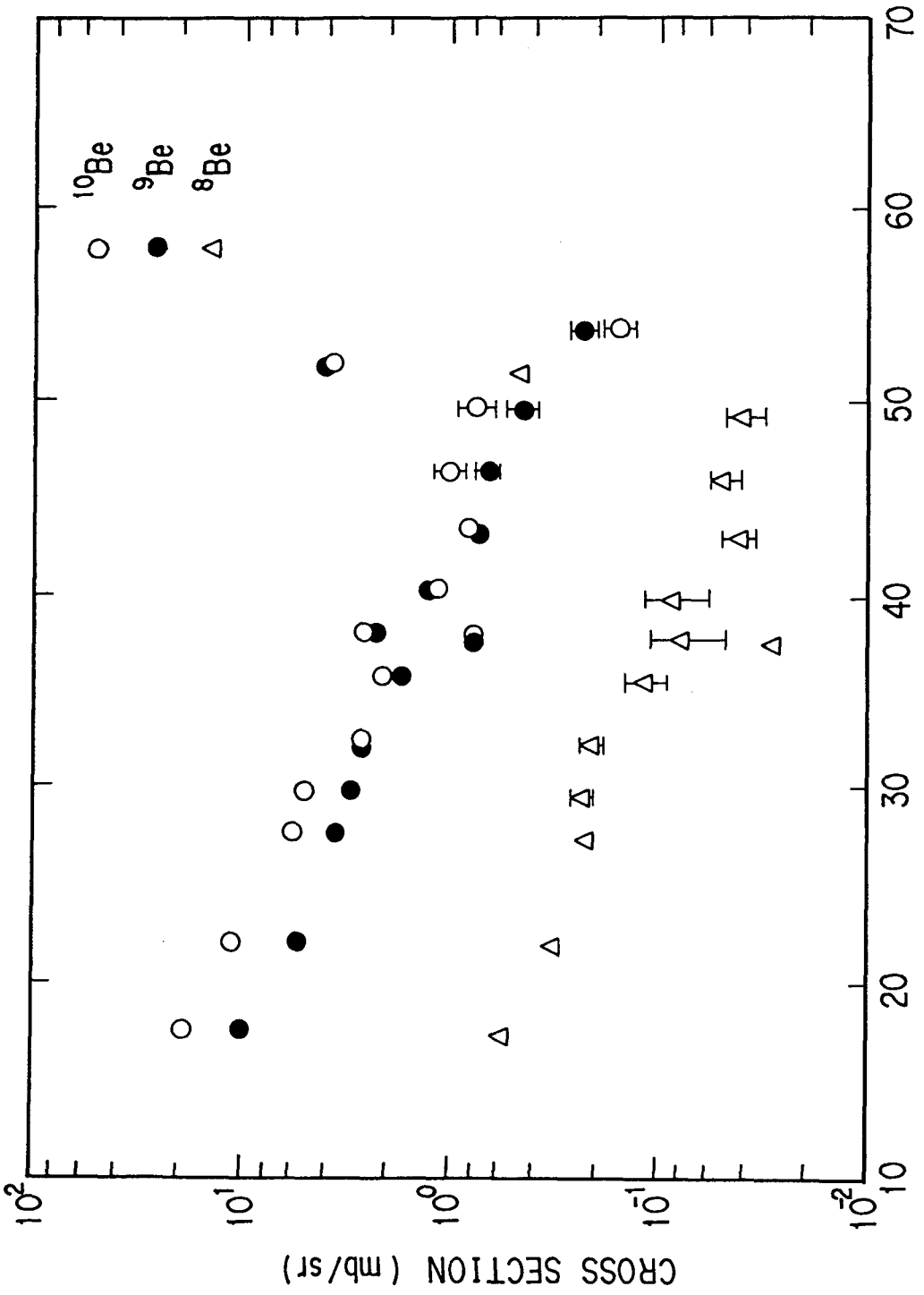

Fig.2.29. Angular distributions of Be isotopes for the 8.8MeV/u ^{16}O-induced reaction.

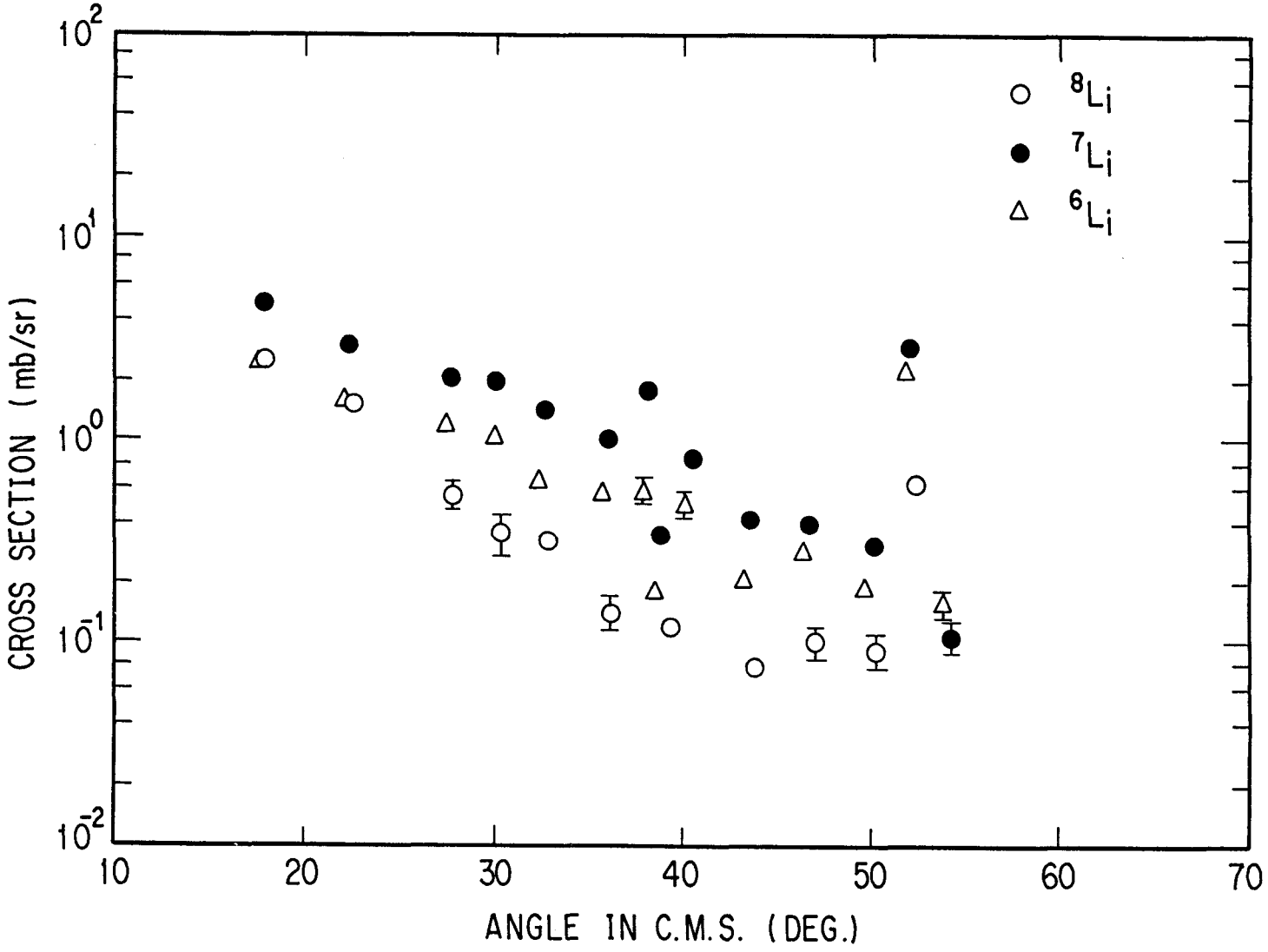

Fig.2.30. Angular distributions of Li isotopes for the 8.8MeV/u ^{16}O-induced reaction.

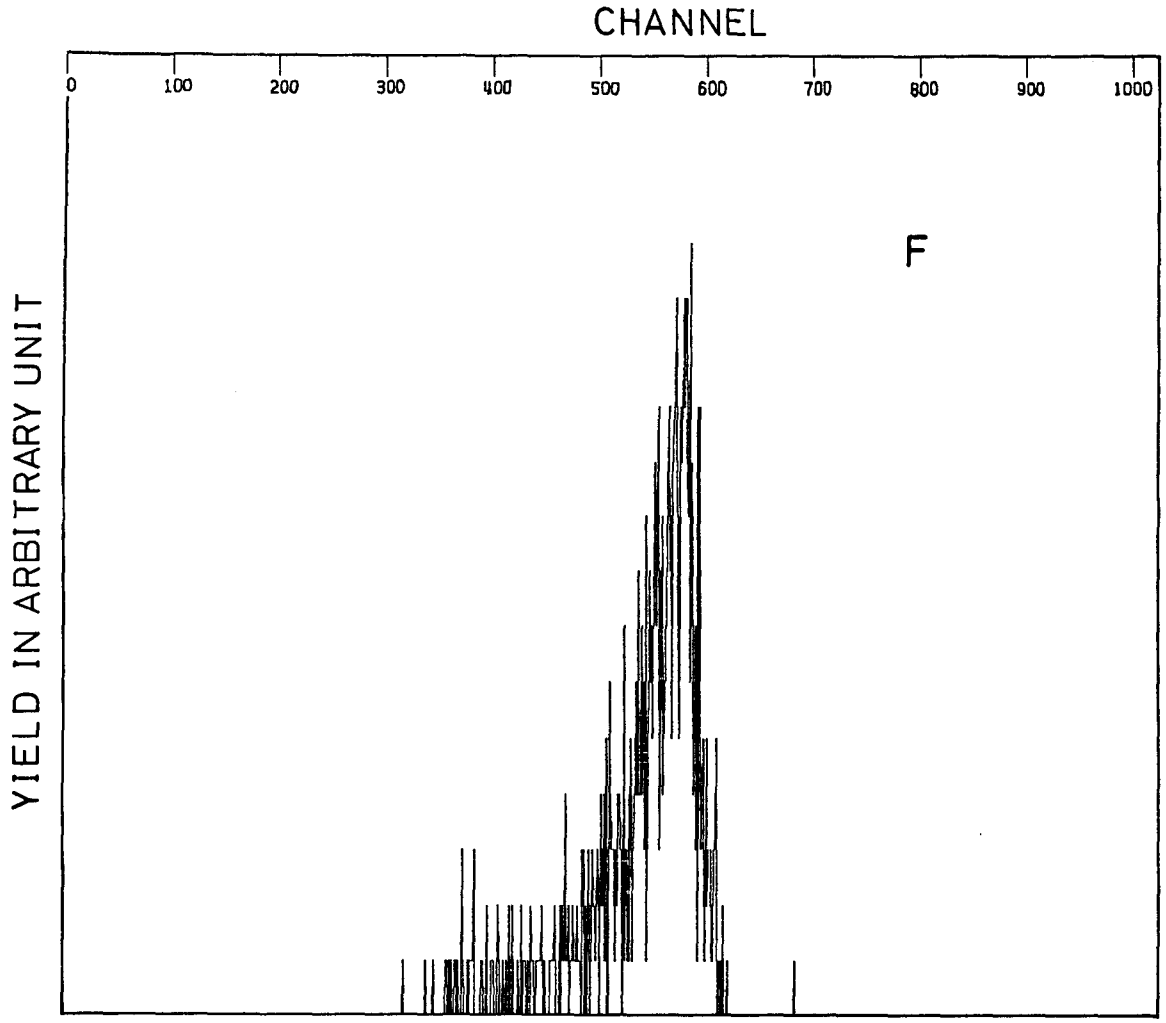

Fig.2.31. An inclusive energy spectrum of the F element observed at 40° in the labolatory system for the 8.8MeV/u ^{16}O-induced reaction.

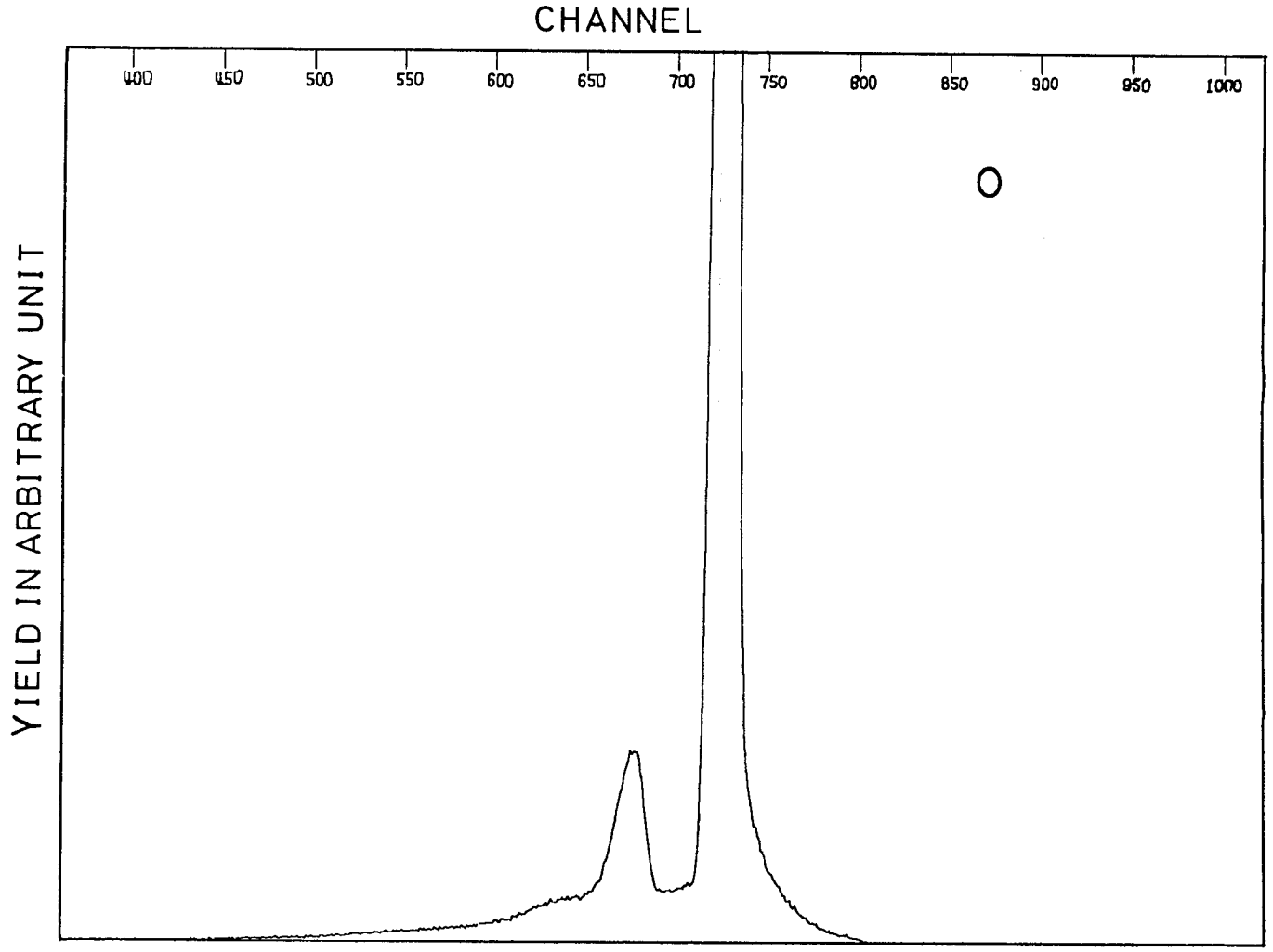

Fig.2.32. An inclusive energy spectrum of the O element observed at 40° in the labolatory system for the 8.8MeV/u ^{16}O-induced reaction.

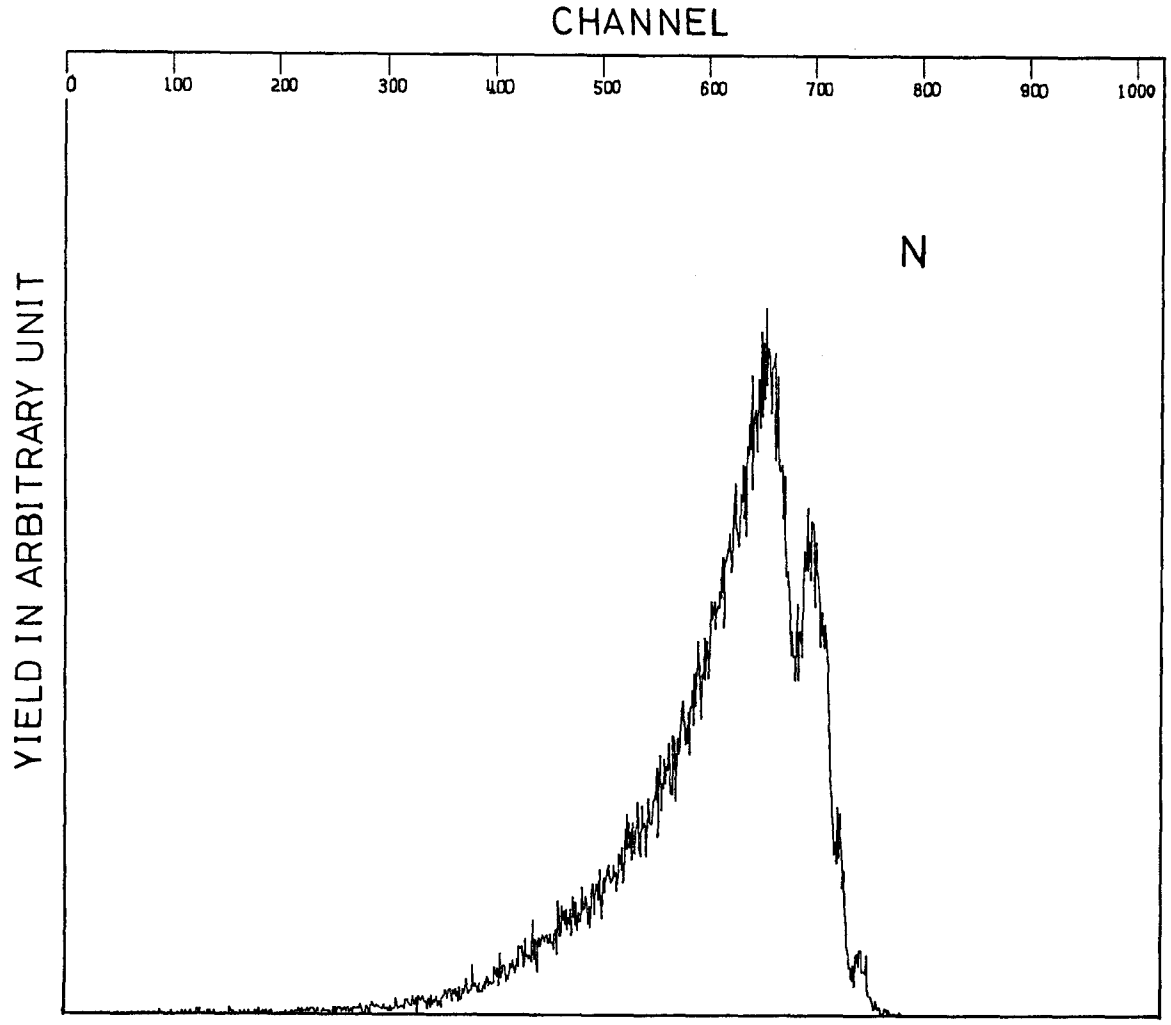

Fig.2.33. An inclusive energy spectrum of the N element observed at 40° in the labolatory system for the 8.8MeV/u ^{16}O-induced reaction.

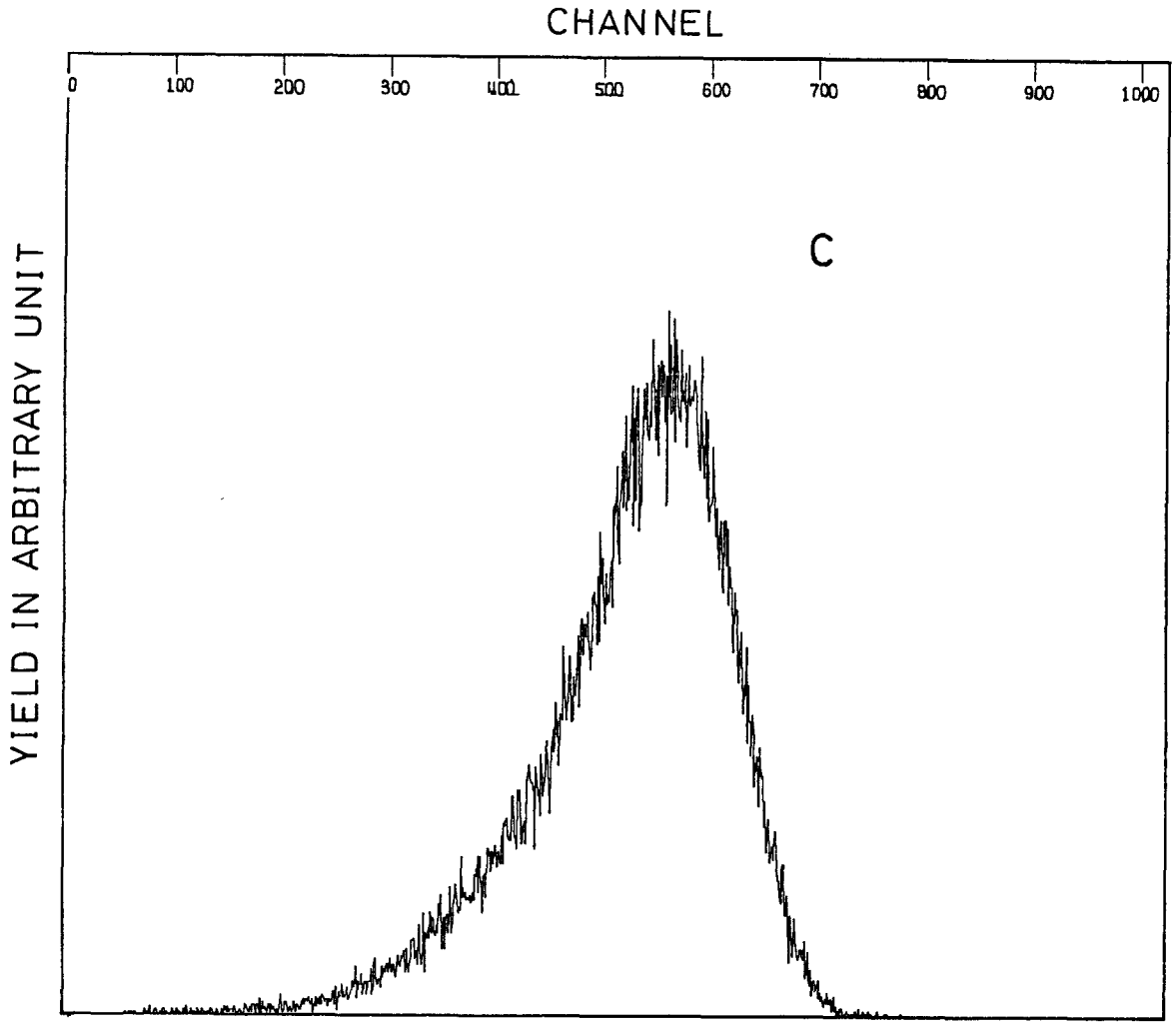

Fig.2.34. An inclusive energy spectrum of the C element observed at 40° in the labolatory system for the 8.8MeV/u ^{16}O-induced reaction.

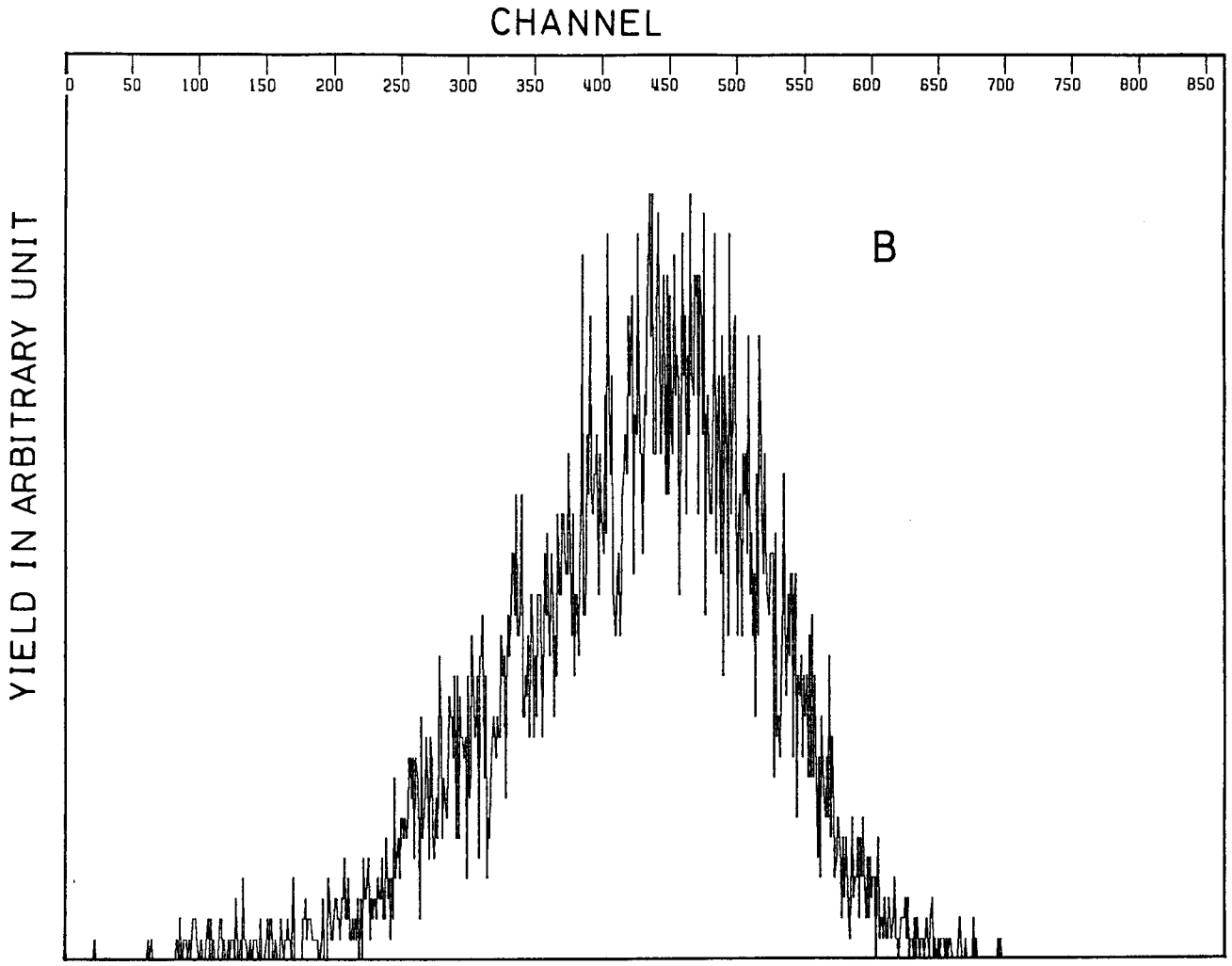

Fig.2.35. An inclusive energy spectrum of the B element observed at 40° in the labolatory system for the 8.8MeV/u ^{16}O-induced reaction.

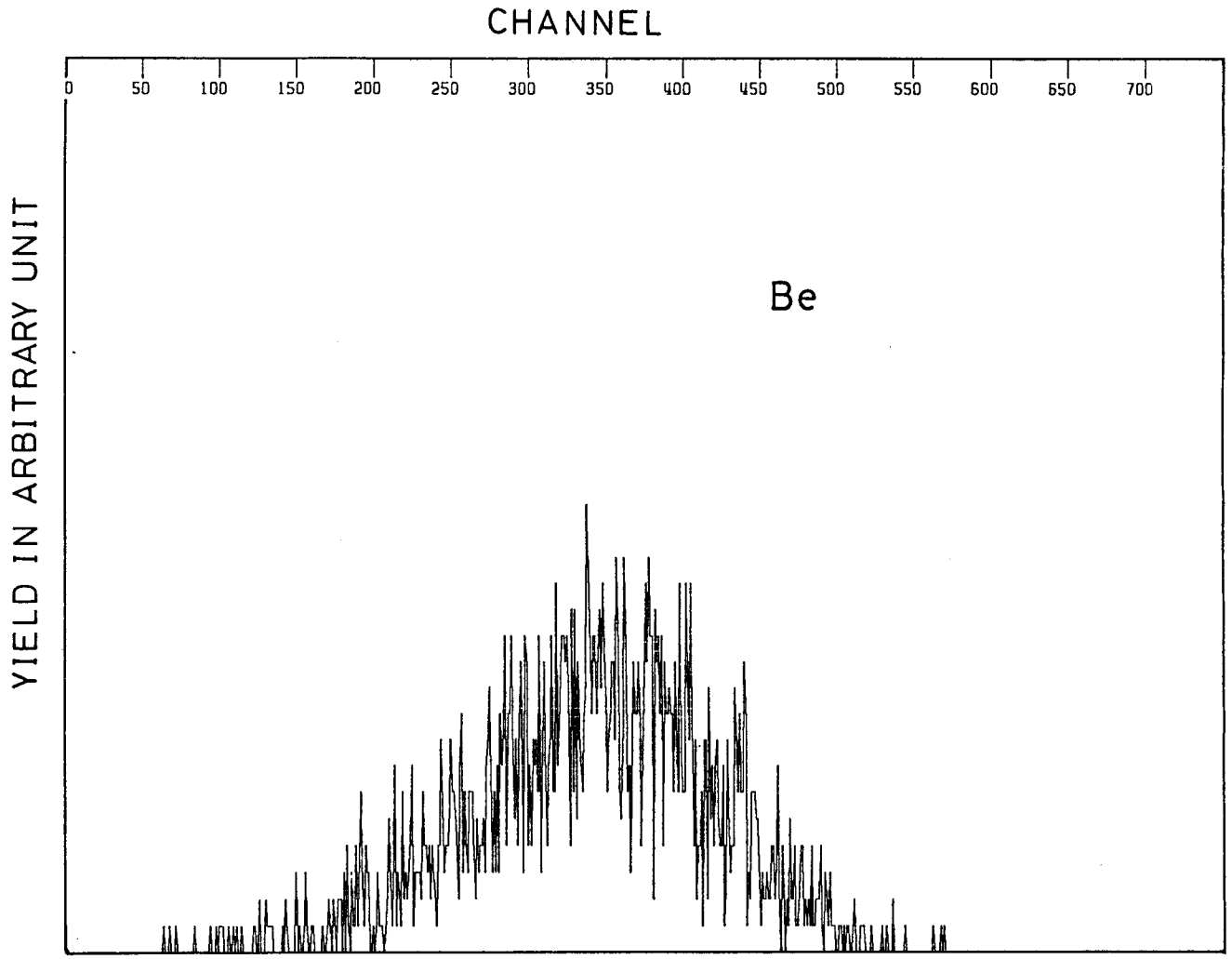

Fig.2.36. An inclusive energy spectrum of the Be element observed at 40° in the labolatory system for the 8.8MeV/u ^{16}O-induced reaction.

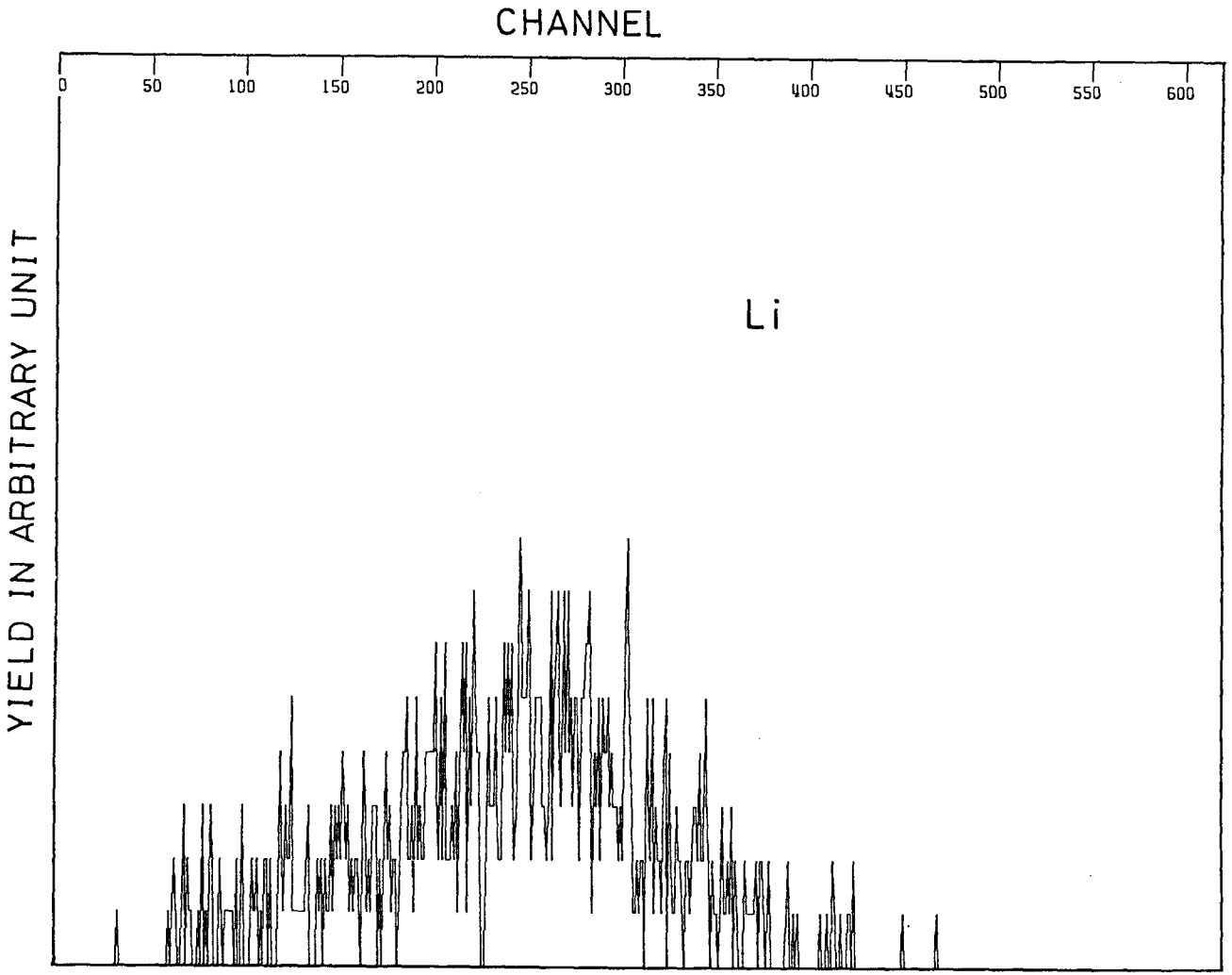

Fig.2.37. An inclusive energy spectrum of the Li element observed at 40° in the labolatory system for the 8.8MeV/u ^{16}O-induced reaction.

characteristics among the energy spectra of all observed elements. They are, however, different from each other in their energy positions and widths of the distributions, which will be discussed in detail in 2.7.1. The results described in 2.6.3 and 2.6.4 suggest that at least two kinds of reaction mechanisms are associated with nucleon transfer reactions producing the projectile-like products in the present systems.

2.6.5. Angular Distribution of the Quasi-Elastic Transfer Reaction

Differential cross sections of the component of the narrow peak in the O or N spectra are plotted with open circles as a function of the scattering angle for both of the 8.8MeV/u and the 6.6MeV/u systems in Fig.2.38. As to the N products, the broad-peaked components are plotted with solid circles as well. Angular distributions depicted with open circles for O and N products are close to each other and they are concentrated on the narrow region near the grazing angle indicated with arrows in the figure for the two observed energies. It corresponds to the grazing trajectory of QET discussed in 2.4.2. Besides narrow peaks are associated with a few nucleon transfer and have characteristics of a small dissipation energy. Their narrow widths may be indicative of a simple mechanism of interaction, an interaction as shallow as QET.

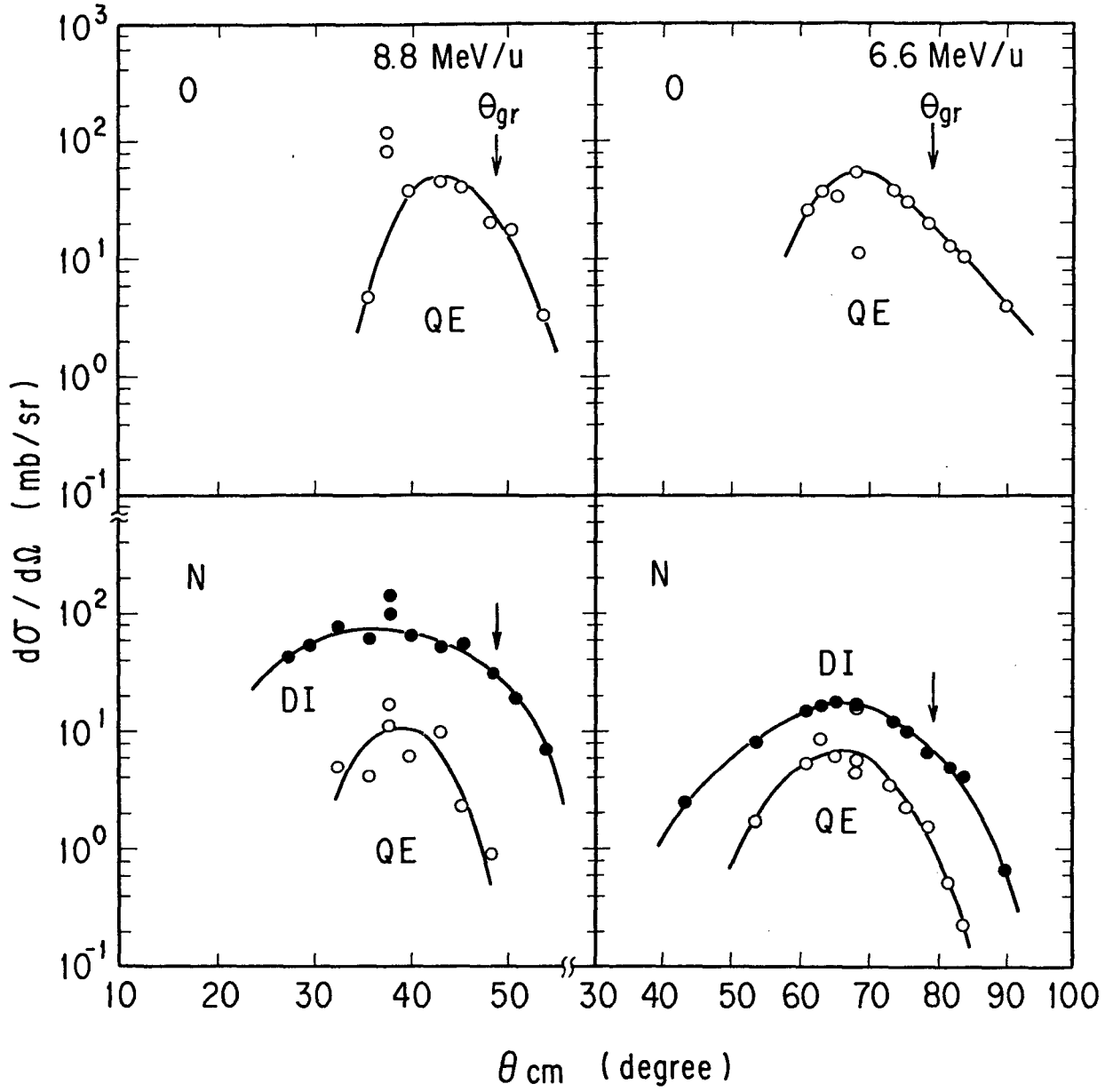

Fig.2.38. Angular distributions of components of the narrow peaks in the O and N spectra plotted with open circles for both of the 8.8MeV/u and the 6.6MeV/u systems. As to the N products, components of the broad peaks are plotted with solid circles as well. Solid lines are drawn for a guide of the eye. Grazing angles are given with arrows for each of the systems.

2.7. DISCUSSION ON PROJECTILE-LIKE PRODUCTS

2.7.1. Total Kinetic Energies and Widths of the Projectile-like Products

Figures 2.39 and 2.40 show the most probable total kinetic energy (TKE) of each element of PLP and the width (FWHM) of the distribution as a function of the scattering angle for the 8.8MeV/u and the 6.6MeV/u ^{16}O-induced reactions, respectively. The total kinetic energy and width are obtained as peak position and width of the Gaussian distribution fitted to the energy spectra. An example of Gaussian fitting for a N spectrum is shown in Fig.2.41. For the N spectrum three Gaussians were required to fit calculation to the data. The Gaussian at the lowest position of the three in channel have the same dependence on scattering angle as the second lowest one. Therefore these two Gaussians are considered to be one component. Therefore the results from the higher two Gaussians will be further discussed.

Open circles in Fig.2.40 represent the QET component which were observed as the narrow peak in the O or N spectrum, while closed circles in Figs.2.39 and 2.40 give the damped component. Such damped components are regarded as those due to DIT [3,5]. As shown in Figs.2.39 and 2.40, QET components show narrower distributions than those of DIT and their damped energies are less than those of DIT. Both of the reactions are, however, nearly independent on the scattered angle. Noting the recoil ranges of Tl anf Hg nuclides in Fig.2.9, which correspond to the counterparts of C and N

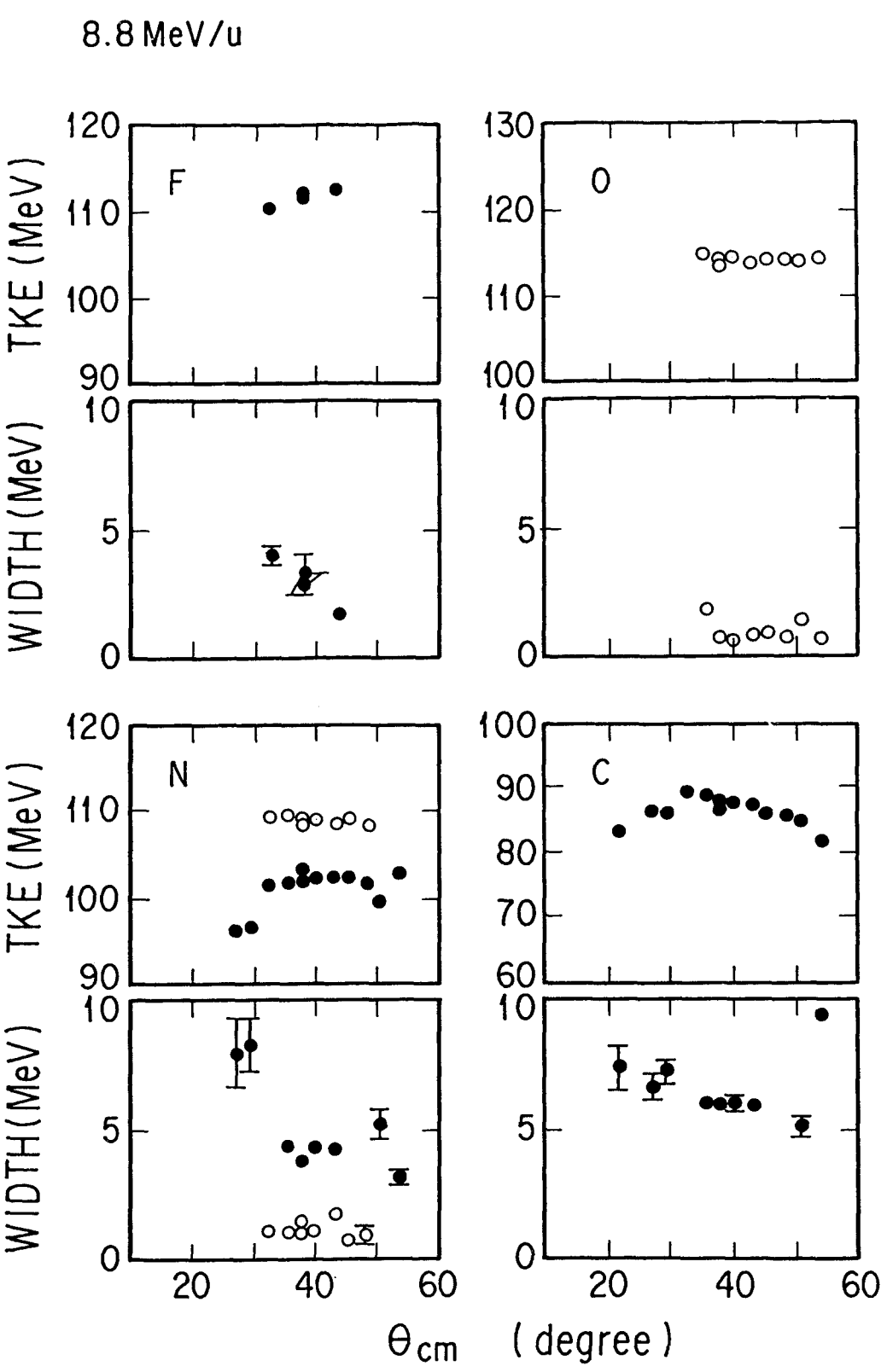

Fig.2.39(a). The most probable total kinetic energy (TKE) of each element of PLP and the width (FWHM) of its distribution as a function of the scattering angle for the 8.8MeV/u ^{16}O-induced reactions.

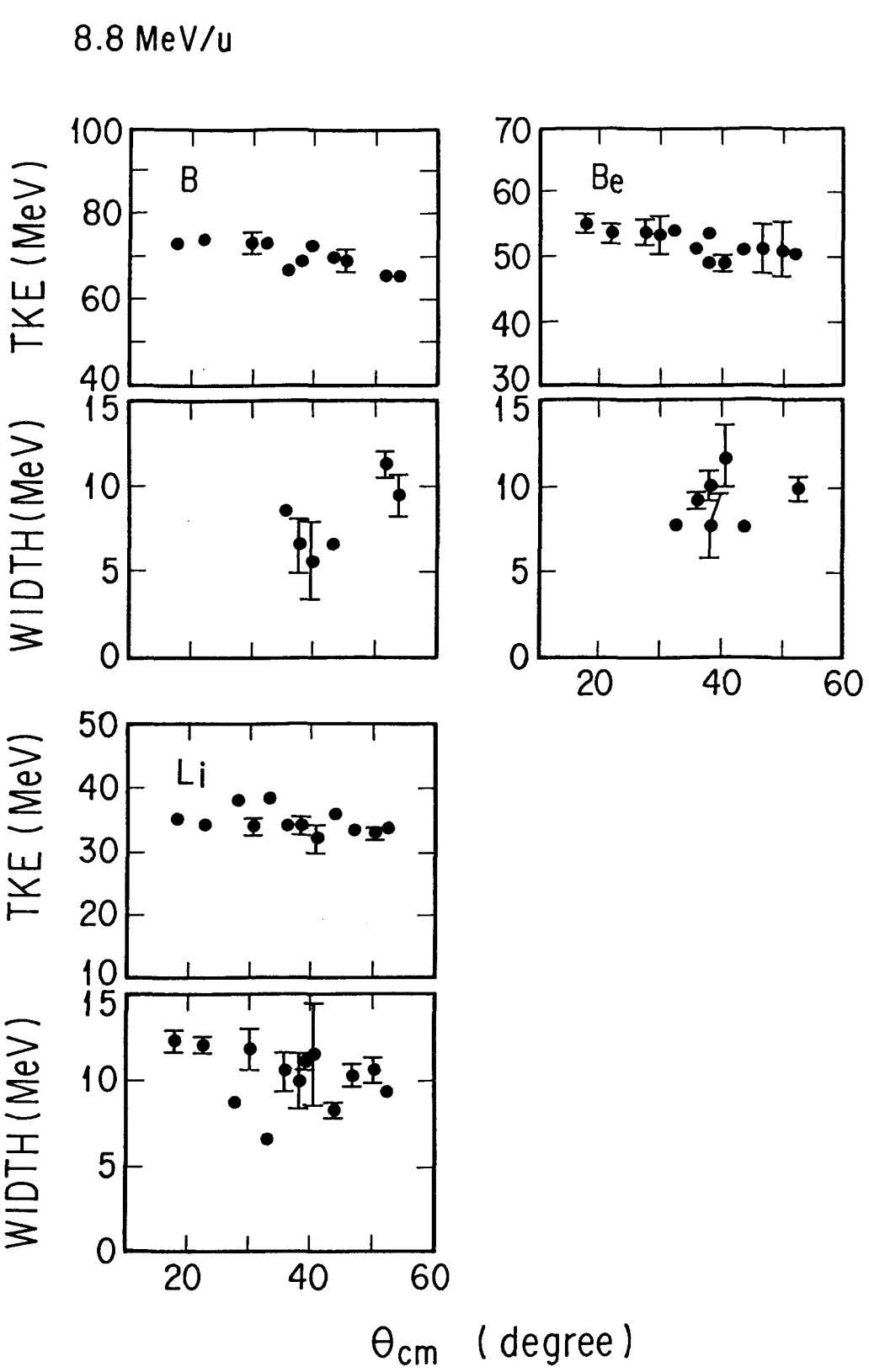

Fig.2.39(b). The most probable total kinetic energy (TKE) of each element of PLP and the width (FWHM) of its distribution as a function of the scattering angle for the 8.8MeV/u ^{16}O-induced reactions.

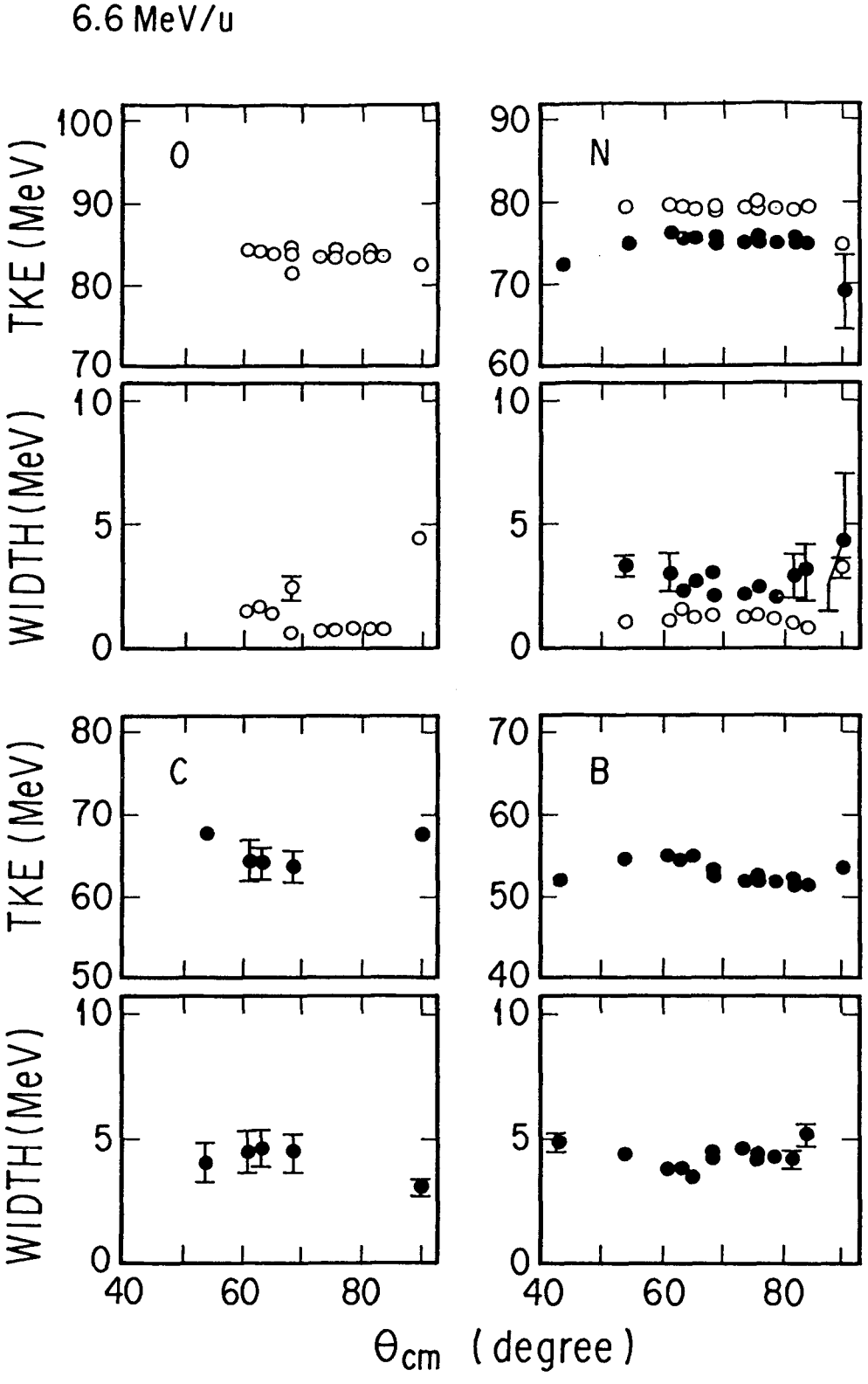

Fig.2.40. Same as Fig.2.39 but for the 6.6MeV/u ^{16}O-induced reactions

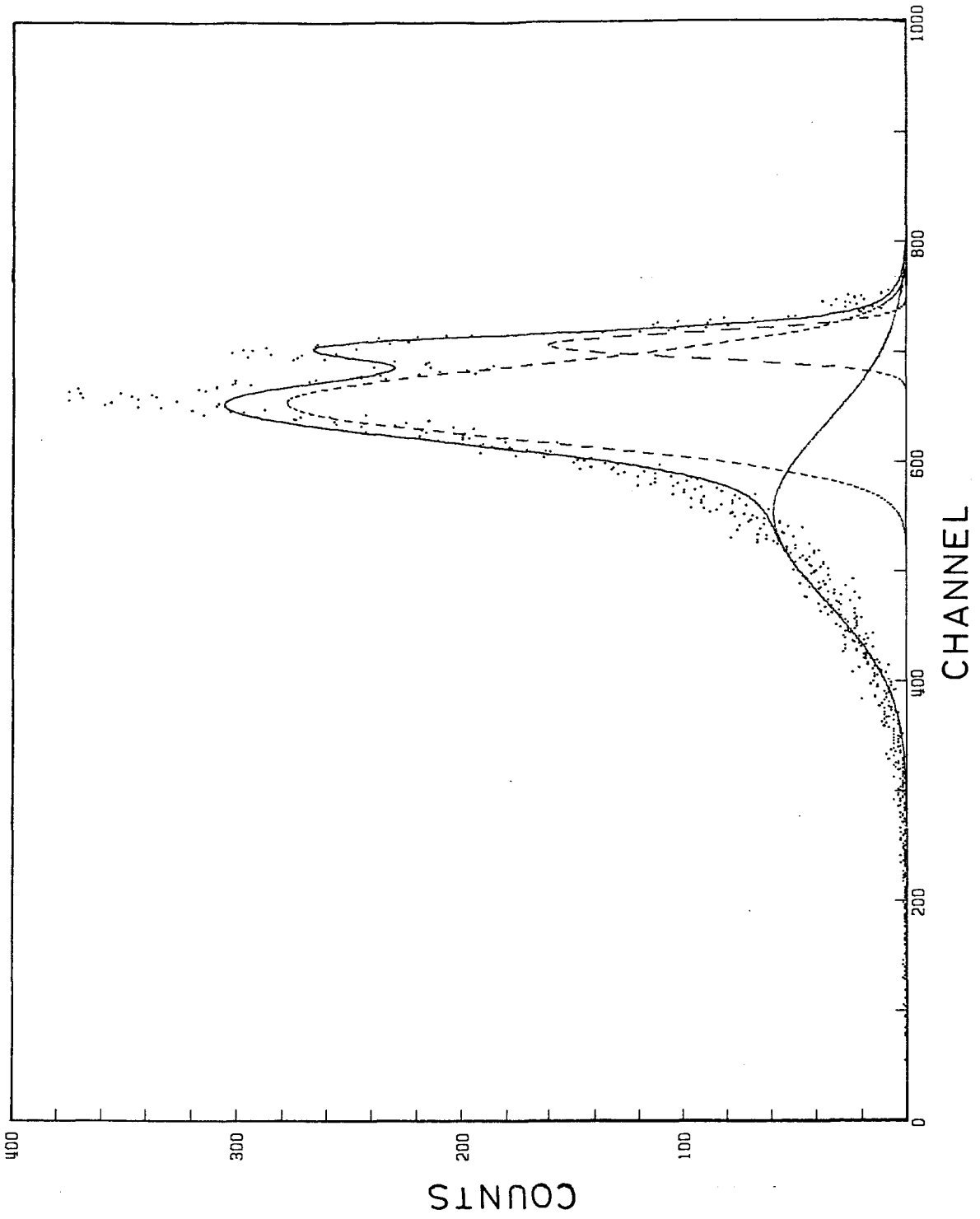

Fig.2.41. An example of the results fitted with three gaussians for the N spectrum.

products, it was found that they were quite similar to the recoil ranges of QET whereas products of DIT show quite a different angular distribution and possess much lower kinetic energies. The recoil ranges of DIT shall be discussed in 2.7.4.

The light fragments produced in the transfer reaction emit some particle if they are sufficiently excited [20]. Let me raise here a question whether the light fragments decay sequentially after the transfer reaction is completed, namely, whether the primary yields of the transfer reaction are preserved among the products. The excitation energies of representative projectile-like products deduced by using the experimental kinetic energies are shown with solid lines in Fig.2.42. They are obtained with the assumption of sharing of the excitation energy according to the mass ratio as follows:

$$E_x = (E_{cm} + Q_{gg} - E_{obs})\, A_{PLP}/(A_P+A_T), \tag{2.16}$$

where E_x is the excitation energy, E_{cm} is the center-of-mass kinetic energy at the entrance channel, E_{obs} is the observed total kinetic energy of a transfer reaction. Q_{gg} is the Q-value for a transfer reaction and calculated with the formula described below:

$$Q_{gg} = (M_P + M_T) - (M_{PLP} + M_{TLP}), \tag{2.17}$$

where M_P and M_T are the masses of projectile and target, and M_{PLP} and M_{TLP} are the masses of projectle-like product and the complementary target-like

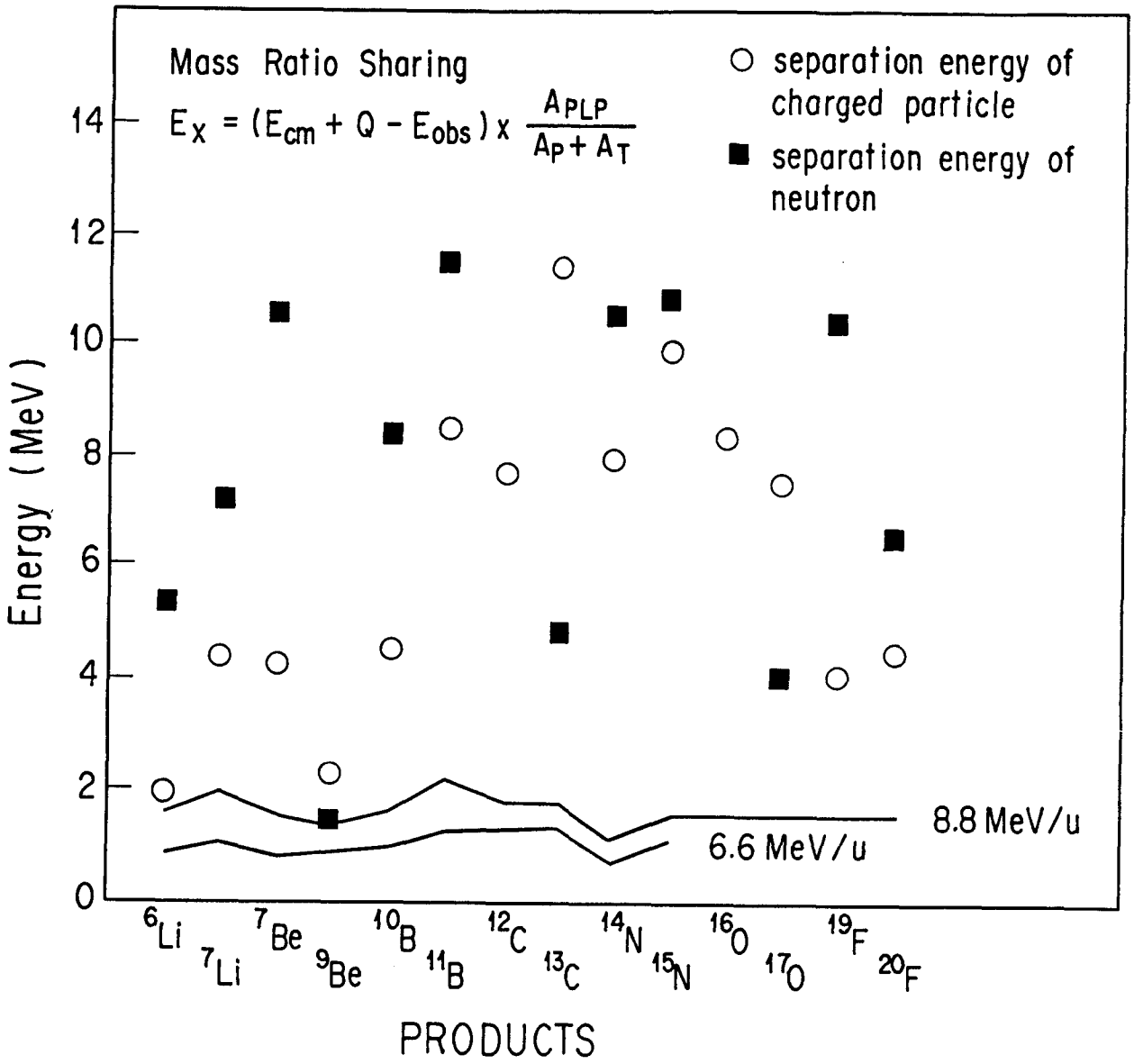

Fig.2.42. Excitation energies of representative projectile-like products deduced by using the experimental kinetic energies. Deduced values are shown with solid lines together with the lowest separation energies of a charged particle (circle) and a neutron (square).

product with the assumption of two-body reaction, respectively. Q_{gg} is the energy required to produce a given pair of products in the ground states in the transfer reaction. The mass data of [38] are referred to for the calculation. The assumption of energy sharing on the mass ratio has been justified in the 11MeV/u and 17MeV/u $^{20}Ne+^{197}Au$ reactions [20] which are expected to be more or less similar to the reaction of this work. The lowest separation energies of a charged particle and a neutron are also plotted in Fig.2.42. It is concluded from the figure that the excitation energy is not enough to undertake a sequential particle emission among the products. Therefore the primary yields are concluded to be directly observed as the final yields and the transfer reaction of the present study is considered to be simply a two-body reaction.

2.7.2. Charge Distributions of Differential Cross Sections of the Deep Inelastic Transfer Reaction

As described in 2.7.1, neither the total kinetic energy nor the width of DIT products depends on the scattering angle. It is therefore likely that the kinetic energy is damped within a fairly short time interval compared to the time scale of rotation of the dinuclear system. In Fig.2.43, charge distributions of the DIT products at three representative angles are shown for each of the 8.8MeV/u and the 6.6MeV/u ^{16}O-induced reactions. One can find that the charge distributions are quite similar to each other among the systems. It may imply that nucleon exchange is also completed

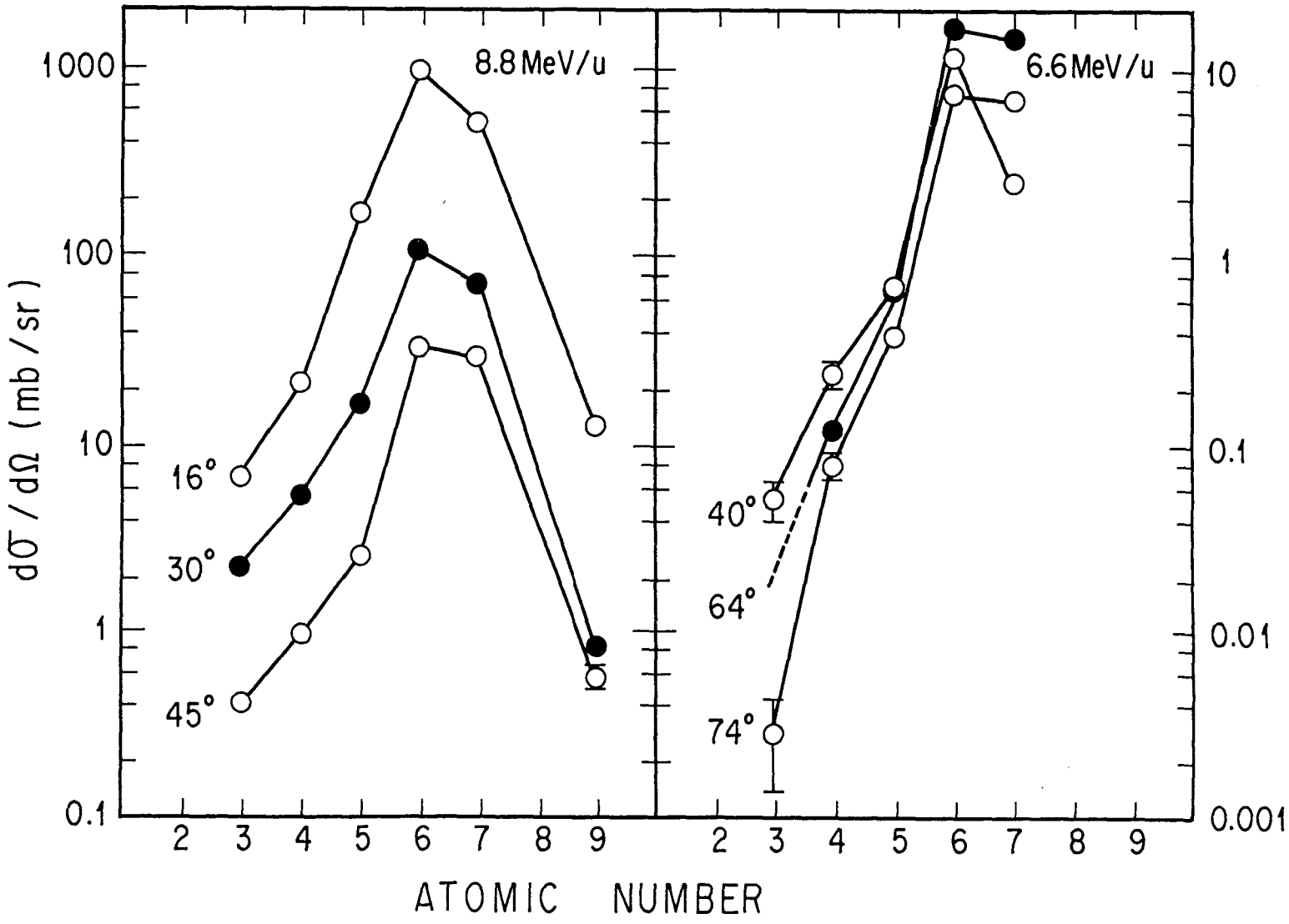

Fig.2.43. Charge distributions of the DIT products at three representative angles for both of the 8.8MeV/u and the 6.6MeV/u ^{16}O-induced reactions.

almost instantaneously as compared with the rotational time scale of the dinuclear system. These results exhibit that the dynamic process within the time scale of rotation of the dinuclear system does not play a significant role in the production of damped components, which may be produced in a rather short interaction time after the nuclear collision.

2.7.3. N/Z Ratio and Dependence of Isotopic Differential Cross Sections on the Q_{gg} Value

In many reaction systems it has been experimentally observed that the N/Z value, the ratio of the neutron number to proton number, of the most probable isotope in each element produced in DIT takes nearly the same value as the N/Z value of the composite system of projectile and target regardless the emission angles. This was interpreted as follows: The distribution of nucleons in a dinuclear system attains equilibration at the early stage of the reaction after the system was composed. An evidence of such equilibration has been given in 2.4.1 for the Au products. The most probable N/Z values of the PLP are plotted versus atomic number in Fig.2.44, in which data of [39] are also shown for comparison. The figure shows that the DIT products of atomic numbers more than 10 have nearly constant N/Z values which are near $(N/Z)_c$ of the composite system, while those of atomic numbers less than 10 vary drastically with the atomic number. Especially the N/Z values in the present system are very different from the $(N/Z)_c$. Therefore equilibration of the N/Z value does not seem to be

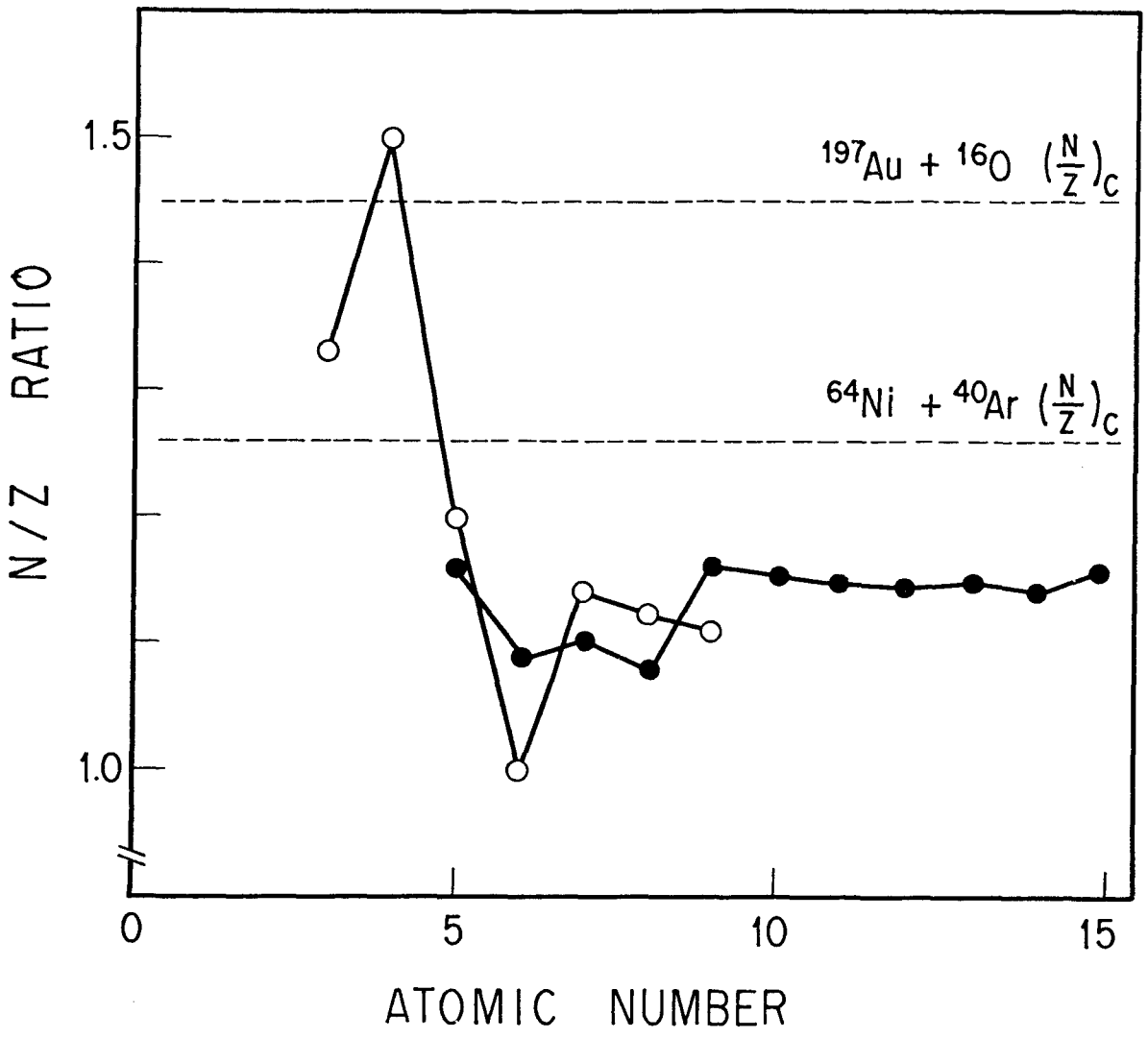

Fig.2.44. The most probable N/Z value of the PLP in the 8.8MeV/u ^{16}O-induced reactions (open circles). Data of [37] are also shown with solid circles for comparison. Solid lines are drawn through the data.

attained among the products in a highly mass-asymmetric system. This may be because the shell effect plays an important role in the light nucleus which has a small number of bound states.

In Fig.2.45 differential cross sections are plotted versus $-Q_{gg}$ value for the production of the relevant isotope at a typical angle for each element. The Q_{gg} value is calculated with eq.(2.17). The slopes of straight lines drawn through isotopic cross sections are nearly the same for these elements as shown in Fig.2.45. This feature is called Q_{gg} systematics [3,40] which was proposed by Artukh et al.

I like to describe here derivation of an expression of the Q_{gg} systematics, which was first proposed by Bondorf et al. [41]. The derivation follows the procedure by Volkov [3]. The probability of formation of a pair of fragments $p(f_{PLP}, f_{TLP})$ may be proportional to the products of the level densities of the fragments, namely, ρ_{PLP} and ρ_{TLP}.

$$p(f_{PLP}, f_{TLP}) \propto \rho_{PLP} \cdot \rho_{TLP} \tag{2.18}$$

The level density of a final product is associated with the excitation energy which is determined by the total excitation energy of the system U_f and its partition between the fragments. U_f will be expressed in the form described below:

$$U_f = U_i + Q_{gg} - Q_c + \Delta E_{rot}, \tag{2.19}$$

where U_i is the excitation energy by dissipation of kinetic energy, Q_c is

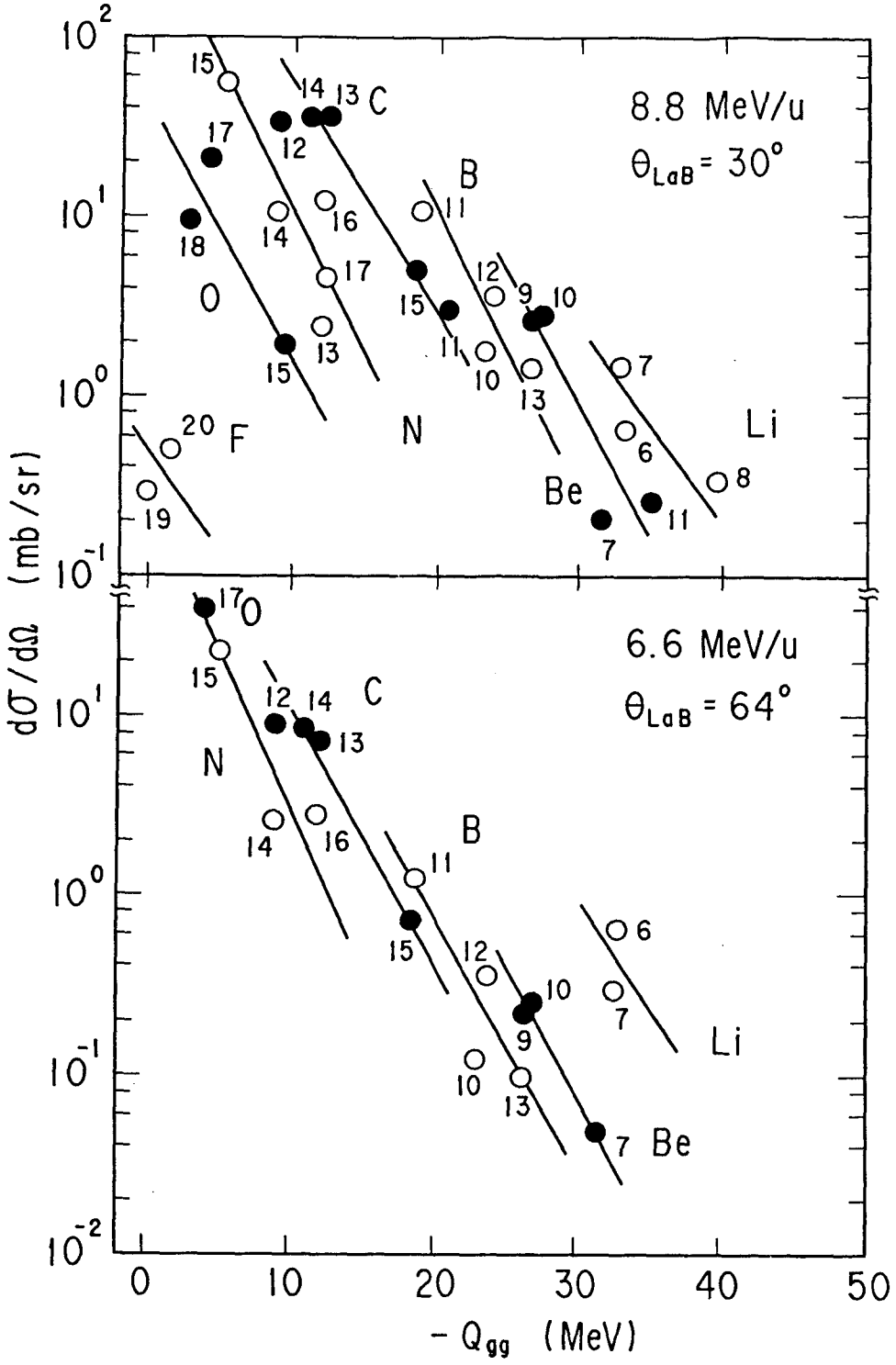

Fig.2.45. Q_{gg} systematics of the isotopic differential cross sections at 30° for the 8.8MeV/u system and at 64° for the 6.6MeV/u system. The straight lines are drawn through the isotopic cross sections.

the energy change of the Coulomb energy due to the transfer of charge. Q_c is given by

$$Q_c = (Z_P Z_T - Z_{PLP} Z_{TLP}) e^2 / R_c \qquad (2.20)$$

where R_c is an effective relative distance where the transfer of charge takes place. ΔE_{rot} is the change of the rotational energy during nucleon transfer in the system, which is associated with variation in its moment of inertia. The level density ρ which is associated with the probability in statistical treatment is expressed in relation to excitation energy U and temperature T.

$$\rho = \exp(U/T)/T \qquad (2.21)$$

This is called a constant-temperature formula which is useful for a low excitation energy [42]. It should be noted that for a dinuclear system the value of T may be somewhat different from the temperature of the corresponding compound nucleus since full statistical equilibration is not attained in DIT. In the present system, almost all of the excitation energy will be concentrated in the target-like products since the projectile-like products have only a small numbers of bound states. Consequently, the product of level densities is expressed as below:

$$\rho_{PLP} \rho_{TLP} \propto \exp(U_f/T). \qquad (2.22)$$

Finally, the probability of the formation of a pair of a projectile-like product and a target-like product is expressed as follows.

$$p(f_{PLP}, f_{TLP}) \propto \exp[(Q_{gg} - Q_c)/T]. \quad (2.23)$$

A theoretical ground of the Q_{gg} systematics is thus obtained. In the derivation, the rotation energy E_{rot} can be neglected since it is small compared to the other terms in U_f in the present system. U_i is also neglected since dissipation energies of the collision may not be significantly different among different exit channels. This will be confirmed in the discussion in 2.7.6. According to Eq.(2.23), Q_{gg} systematics is interpreted as an indication that those nuclides are produced via a common hot zone with a well-defined temperature. The feature is characteristic in the mass-asymmetric transfer reaction.

2.7.4. E_{cm}/B_{coul} as a Determining Factor of the Angular Distribution of the Deep Inelasic Transfer Reaction

Mathews et al. have pointed out that small values of E_{cm}/B_{coul} ($\leqq 1.5$) are generally associated with the side-peaked angular distribution while larger values of E_{cm}/B_{coul} are associated with the forward-peaked angular distribution [43,44]. I did observe side-peaked distributions in the 6.6MeV/u ^{16}O-induced reaction where E_{cm}/B_{coul} was about 1.3, and forward-peaked distributions in the 8.8MeV/u ^{16}O-induced reaction where E_{cm}/B_{coul}

was about 1.7 as shown in Fig.2.23. Inclusive angular distributions in Fig.2.23 are expected to consist predominantly of the DIT products because the yields of QET are much less than those of DIT as shown in Fig.2.38. Mathews et al. insist that this happens because E_{cm}/B_{coul} should be a measure of the life time of the dinuclear system which in turn determine the scattering angle of the products. However, I like to point out importance of the grazing angle θ_{gr}. Generally speaking, θ_{gr} is about 60° when E_{cm}/B_{coul} is 1.5 . Scattering angles of the products are expected to be near the θ_{gr} if the interaction time is shorter than the time of rotation of the dinuclear system as shown in Fig.2.46, where solid lines represent the Coulomb trajectories of a projectile with angular momenta of 0ħ, 20ħ, 40ħ, 60ħ, 80ħ, and 100ħ for the 8.8MeV/u system and those of 0ħ, 20ħ, 40ħ, and 60ħ for the 6.6MeV/u system at the entrance channel. Exit trajectories are drawn only for their angular momenta larger than ℓ_{gr}. A circle is drawn with a radius equal to the sum of radii of target and projectile nuclei. As stated before, the observed angular distribution indicates that the interaction time is much shorter than the time scale of rotation of the dinuclear system. The figure tells that the determining factor of the angular distributions of DIT may be the variation of θ_{gr}. Furthermore recoil ranges of Tl and Hg shown in Fig.2.9 exhibit a QET-like energy dependence which would be a strong evidence that the grazing angle plays a rather direct role in the damped reaction.

2.7.5. Comparison of Experimental Cross Sections with Model Calculations

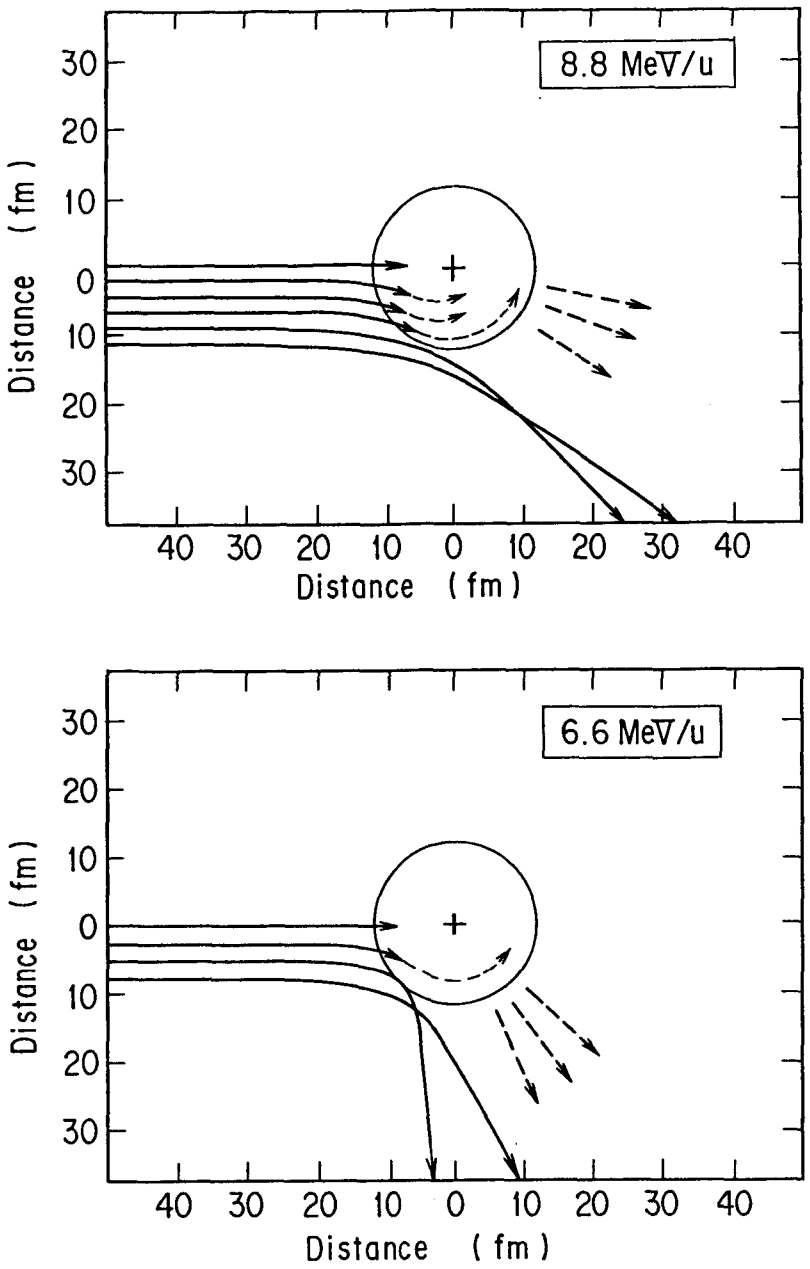

Fig.2.46. Relation of Coulomb trajectories of a projectile and angular distribution of the DIT products. The Coulomb trajectories are depicted for angular momenta of 0ħ, 20ħ, 40ħ, 60ħ, 80ħ, and 100ħ for the 8.8MeV/u system and those of 0ħ, 20ħ, 40ħ, and 60ħ for the 6.6MeV/u system at the entrance channel. Exit trajectories are drawn only for their angular momenta larger than ℓ_{gr}. A circle is drawn with a radius equal to the sum of radii of target and projectile nuclei.

Angle-integrated cross sections of projectile-like products produced in DIT are plotted with circles for the incident energies of 8.8MeV/u (Fig.2.47) and 6.6MeV/u (Fig.2.48). The integration was carried out by extrapolation and interpolation in the angular distributions. The error bars seen in the figures include errors of uncertainties in the integration.

I will describe in this subsection comparison of these data with model calculations in order to confirm the relation of the DIT products yields of projectile-like products with their characteristic features such as the Q_{gg} systematics and the short interaction time. Wilczyński et al. proposed a sum rule model [21,22] which is based on the Q_{gg} systematics [3,40] and an assumption of the limiting angular momentum. Cross section of a projectile-like product is expressed as follows:

$$\sigma(i) = \pi \lambda^2 \sum_{\ell=0}^{\ell_{max}} [(2\ell+1) \frac{T_\ell(i)p(i)}{\sum_j T_\ell(j)p(j)}] , \qquad (2.24)$$

where

$$T_\ell(i) = [\ 1+\exp((\ell - \ell_{lim}(i))/\Delta\ )]^{-1}, \qquad (2.25)$$

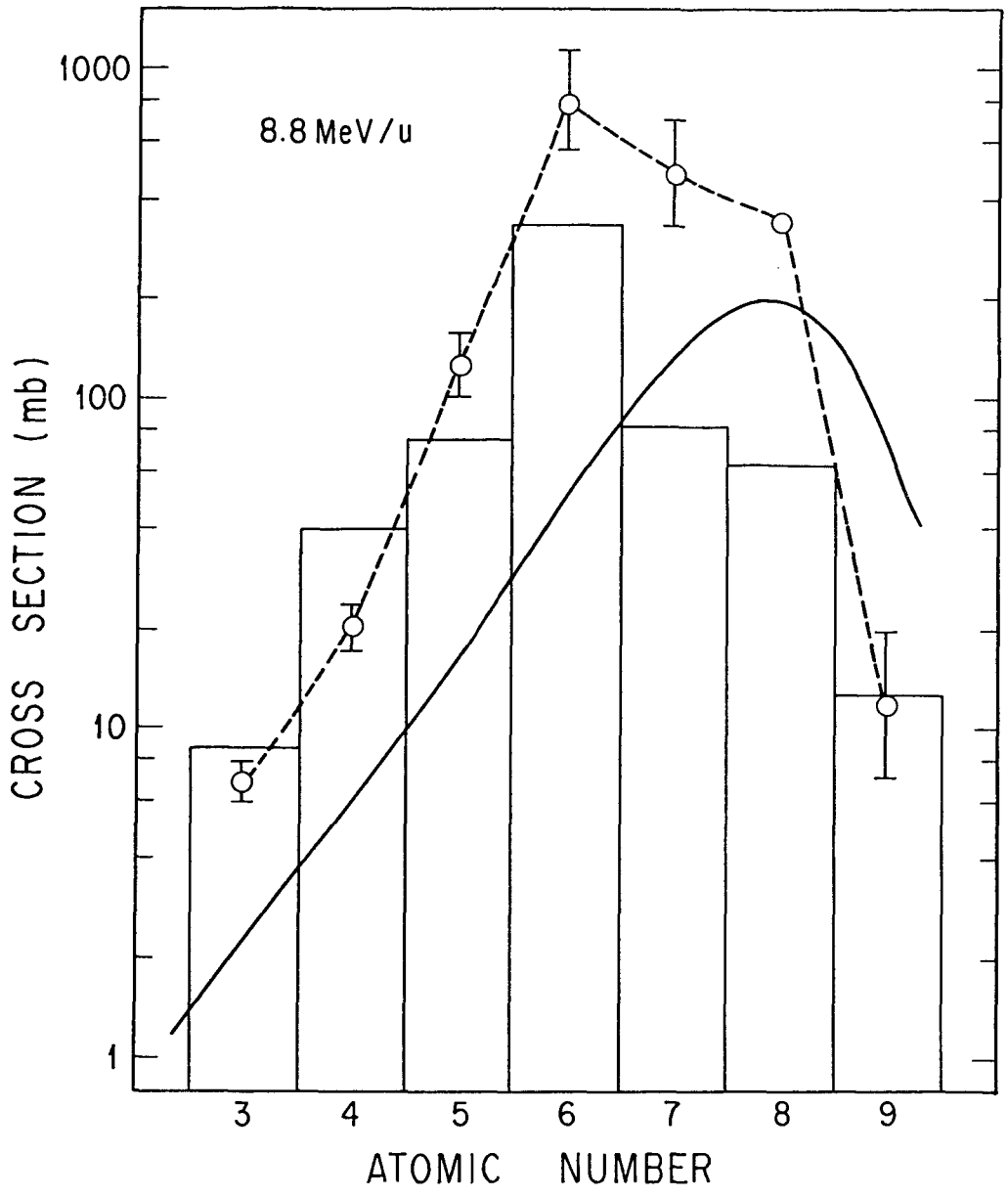

Fig.2.47(a). Angle-integrated cross sections of the elements produced in DIT for the 8.8MeV/u ^{16}O-induced reaction. Calculation with a sum rule model [21,22] and that with a diffusion model [15-17] are drawn with a histogram and a solid line, respectively. A dashed line is drawn through the experimental cross sections plotted with circles.

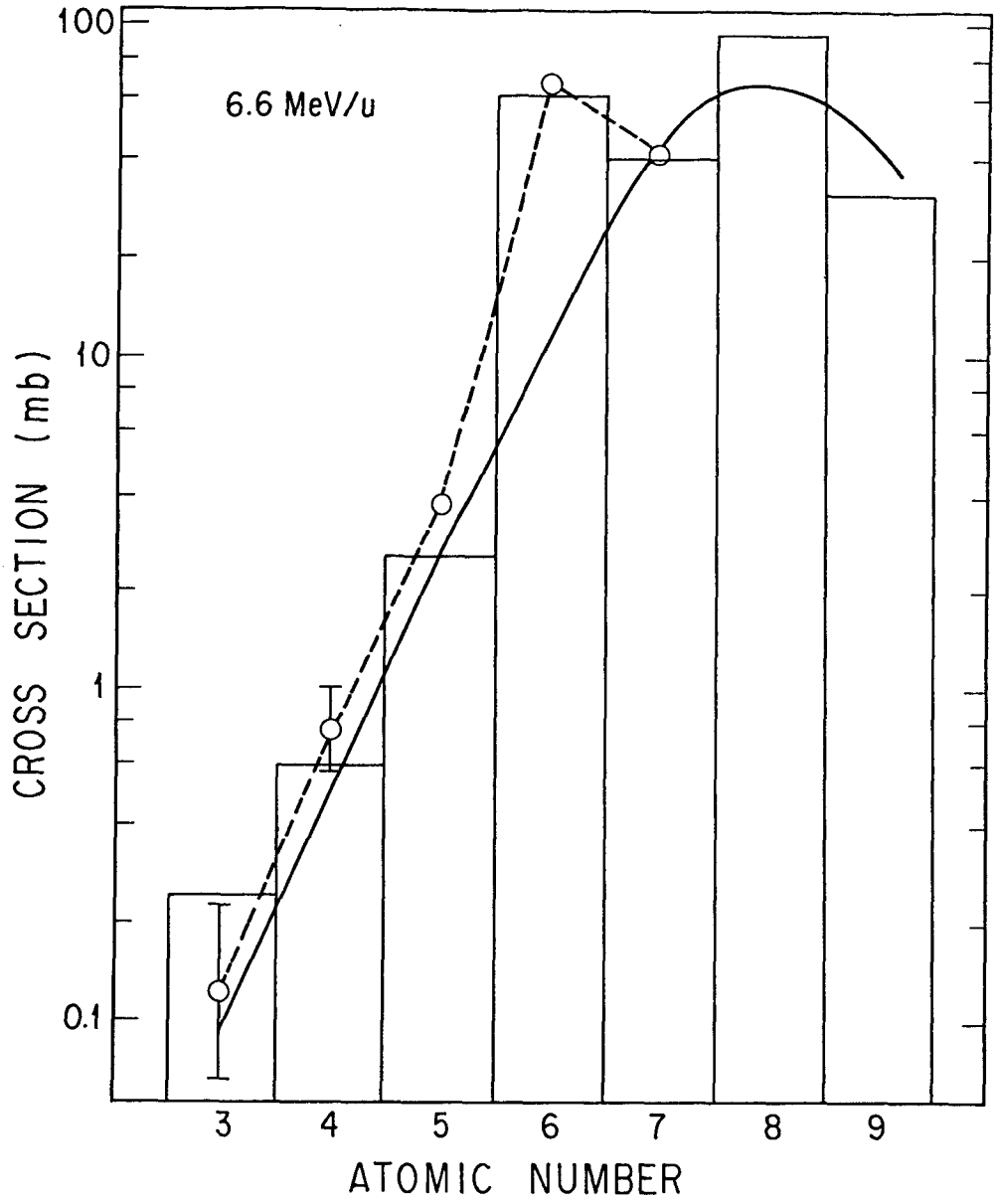

Fig.2.47(b). Angle-integrated cross sections of the elements produced in DIT for the 6.6MeV/u ^{16}O-induced reaction. See caption Fig.2.47(a).

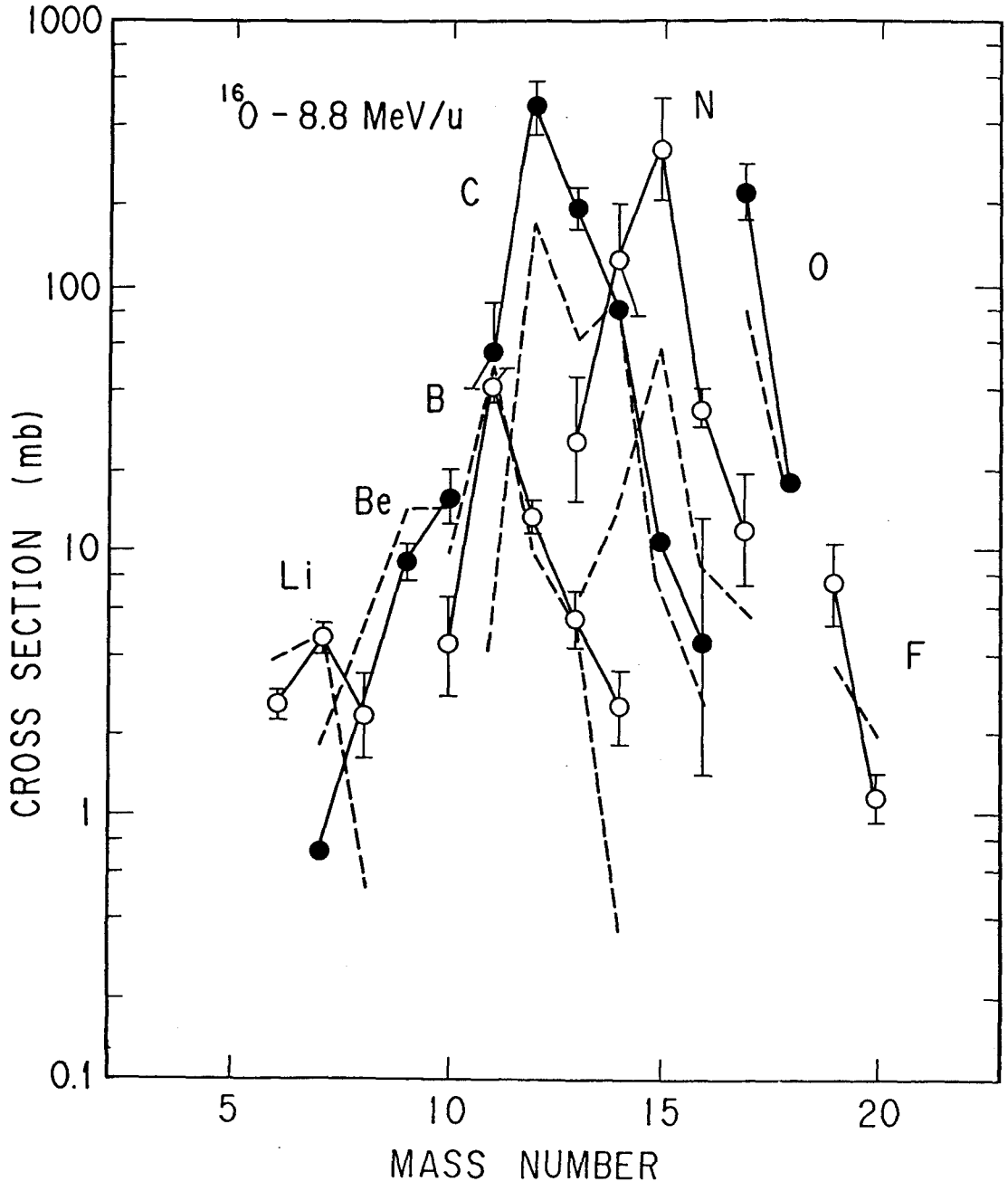

Fig.2.48. Angle-integrated cross sections of the isotopes produced in DIT for the 8.8MeV/u ^{16}O-induced reactions. Calculation with the sum rule model is depicted with a dashed line while a solid line is drawn through the experimental cross sections.

$$\ell_{lim(i)} = \frac{A_P A_T}{mA_P + nA_T} \ell_{crit}, \qquad (2.26)$$

and p(j) is given by Eq.(2.23). T_ℓ is the transmission coefficient, ℓ_{lim} and ℓ_{crit} are limiting angular momenta of the product and of fusion, respectively. Δ is a parameter that represents the diffuseness of the T_ℓ distribution. m is a number of nucleons transferred from target to projectile and n is a number of nucleons transferred but in the opposite direction. I fitted calculation to the data by adjusting several parameters listed in Table 2.4.

For comparison, the diffusion model calculation [10-17], which was proposed to explain the dynamic process of DIT and have been applied to a large body of data successfully in relatively mass-symmetric systems, was also performed. According to the diffusion model, a differential cross section of an element is calculated as follows [15-17]:

$$\frac{d^2\sigma}{d\theta\, dZ_{PLP}} = 2\pi /k^2 \int_{\ell_{crit}}^{\ell_{gr}} \ell\, P(Z_{PLP}, \theta)\, d\ell, \qquad (2.27)$$

where

$$P(Z_{PLP}, \theta) = \sum_{n=1}^{\infty} \exp\{-\ln 2/t_{1/2}(\tau_{int}(\ell))_n\, P\{Z_{PLP}, (\tau_{int}(\ell))_n\} \qquad (2.28)$$

Table 2.4. Parameters of the sum rule model.

$^{197}Au+^{16}O$	T (MeV)	Δ ($\hbar$)	Rc (fm)	ℓ_{max} ($\hbar$)
8.8MeV/u	3	2	15	75
6.6MeV/u	2	2	27	48

Table 2.5. Parameters of the diffusion model calculation.

$^{197}Au+^{16}O$	ℓ_{crit}	ℓ_{gr}	Dz (s^{-1})	Vz (s^{-1})	$t_{1/2}$(s)
8.8MeV/u	61	75	3.2×10^{21}	$-0.8\sim -1.0\times 10^{21}$	2×10^{-22}
6.6MeV/u	43	48	0.7×10^{21}	$-3.0\sim -3.2\times 10^{21}$	2×10^{-22}

and

$$P\{Z_{PLP},(\tau_{int}(\ell))_n\} = \{4\pi D_z \tau_{int}(\ell)\}^{-1/2} \times \exp\{-(Z_{PLP}-Z_P-v_z\tau_{int}(\ell))^2/(4D_z\tau_{int}(\ell))\} \quad (2.29)$$

k is the wave number of relative motion. v_z and D_z are the drift velocity and the diffusion coefficient of charge, respectively [12-16]. τ_{int} is the interaction time. $t_{1/2}$ is the half life of the dinuclear system [17]. Used parameters for the calculation are listed in Table 2.5.

In Fig.2.48 isotopic cross sections calculated by the sum rule model are plotted with a dashed line while solid lines are drawn through the experimental cross sections. One can see that they reproduce well the isotopic distribution of each element. In Fig.2.47, a dashed line is drawn through the experimental cross sections. The solid line represents the cross sections calculated by the diffusion model, while histograms give those calculated by the sum rule model. One can say from the figure that the sum rule model reproduces the experimental cross sections better than the diffusion model. This is because the Q_{gg} dependence, which was clearly observed among isotopic cross sections, is taken into consideration in the sum rule model. The nucleon transfer reaction studied in the present work is therefore concluded to display the features of partial equilibration rather than those of the dynamic process.

2.7.6. Comparison of the Total Kinetic Energies and Siemens Recoil

Formula

Total kinetic energies of the emitted particles were tried to be calculated with an assumption that dissipation of the kinetic energy occurs only at the instant of nuclear collision. A formula described below [22] was used for calculation.

$$TKE = U_f(D)+\mu_f/\mu_i K^2(E_{cm}-U_i(D)-E_{diss}), \tag{2.30}$$

where

$$U(D) = U_{coul}(D) + U_{nucl}(D) \tag{2.31}$$

and

$$K = (1 - n/(A_T-m+n)- m/(A_P+m-n)). \tag{2.32}$$

Here U_{coul} and U_{nucl} represent the Coulomb and the nuclear potential, respectively. I used the nuclear potential of [45,46]. n is the number of nucleons transferred from the projectile to the target and m is the number of nucleons transferred in the opposite direction. K is the recoil term by Siemens et al. [47]. μ is the reduced mass. The suffixes i and f stand for the entrance and exit channels, respectively. The distance of collision D was assumed to be equal to the sum of the half density radii. E_{diss} denotes the dissipation energy which is taken to be an adjustable parameter. Values of 20MeV and 10MeV were adopted as E_{diss} for 8.8MeV/u and 6.6MeV/u systems, respectively. The calculated TKEs are given with a dashed line in Figs.2.49

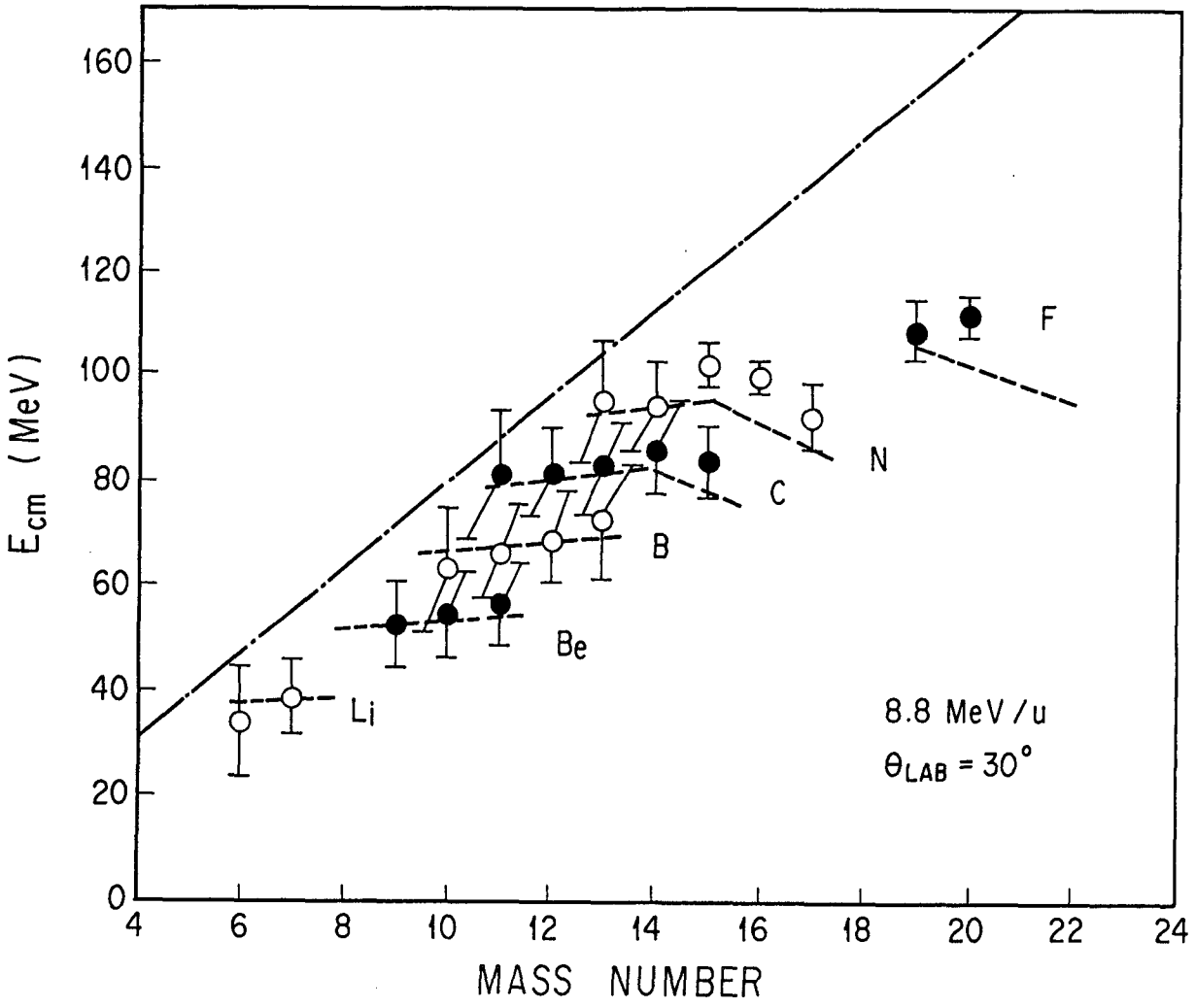

Fig.2.49(a). The most probable total kinetic energies of the isotopes produced in DIT at 30° for the 8.8MeV/u ^{16}O-induced reaction. Calculation with eq.(2.30) is depicted with a dashed line. The dot-dashed line in the figure represents the energies which the products would acquire if they are not damped at all.

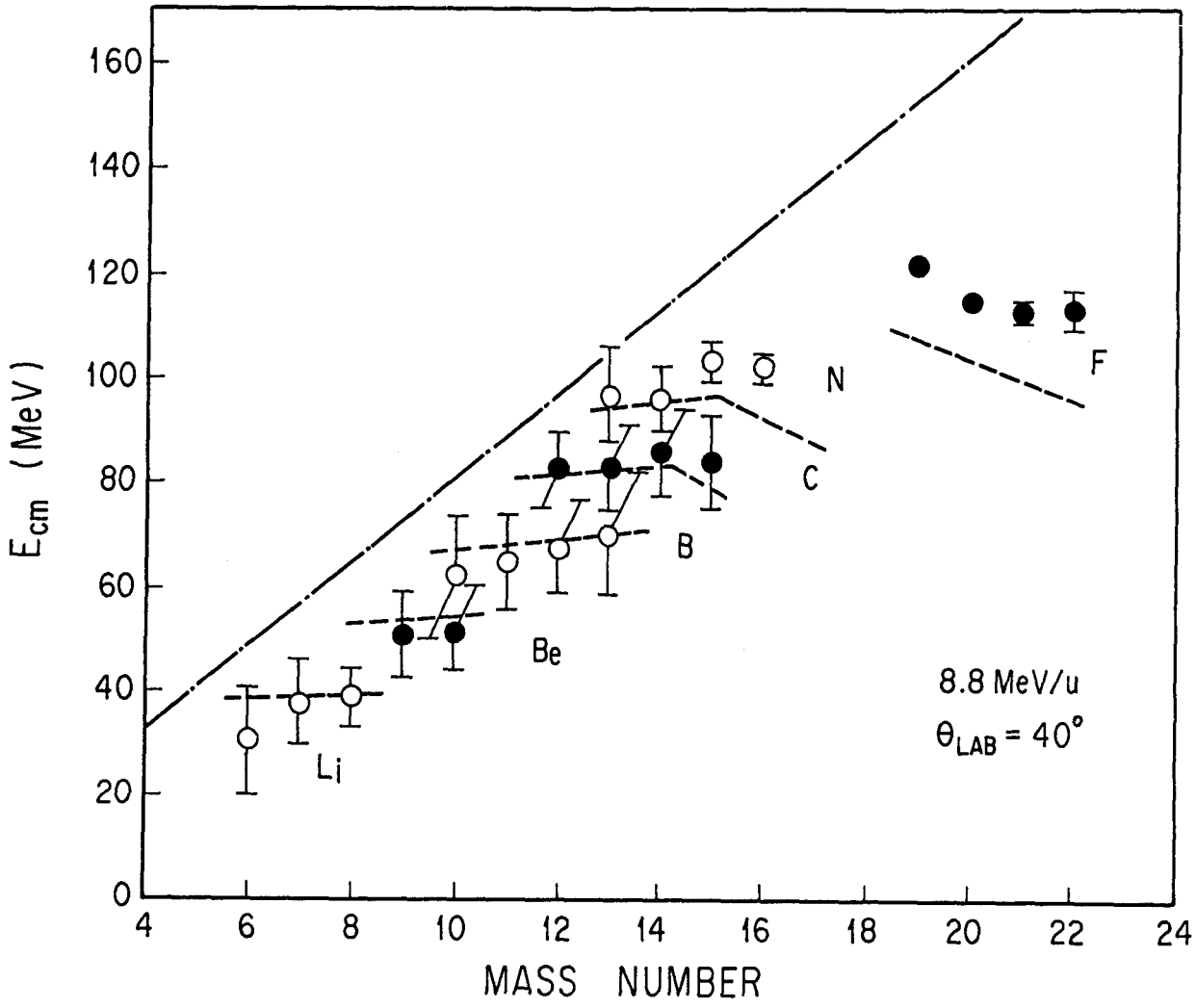

Fig.2.49(b). The most probable total kinetic energies of the isotopes produced in DIT at 40° for the 8.8MeV/u ^{16}O-induced reaction. See caption Fig.2.49(a).

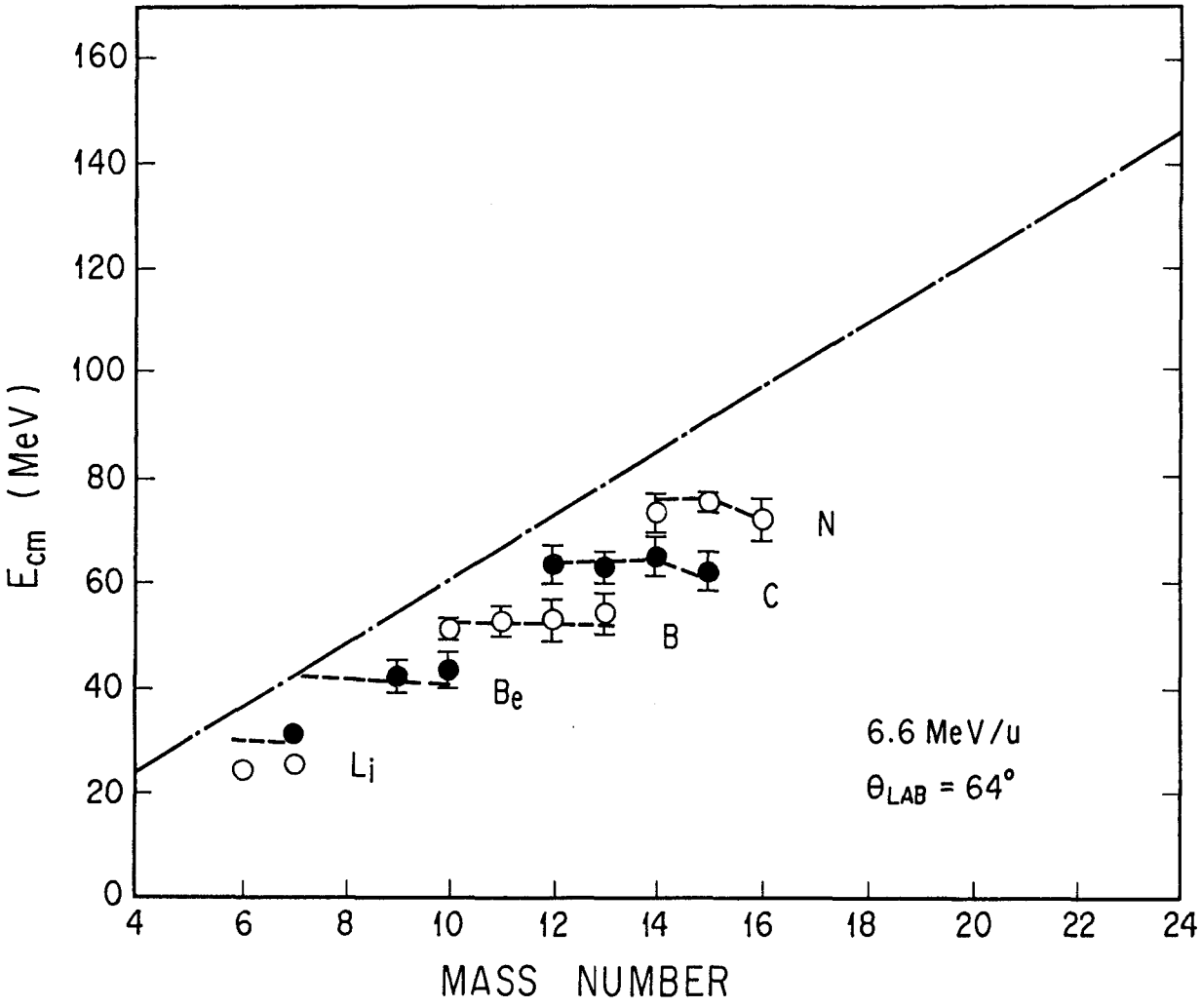

Fig.2.50. Same as Fig.2.49. but at 64° for the 6.6MeV/u ^{16}O-induced reaction.

and 2.50 in comparison them with the most probable kinetic energies measured for each of the isotopes. Dotted and dashed lines in the figures represent the energies which the products would acquire when they are not damped at all. The figure exhibits that the calculated values reproduce fairly well the experimental ones. This would be a strong evidence that the amount of dissipation of the kinetic energy is determined in the interaction for a very short time.

2.8. CONCLUSION

Both quasi-elastic transfer (QET) and deep inelastic transfer (DIT) reactions were observed in the mass-asymmetric nucleon transfer reaction of heavy-ions on ^{197}Au. Observations indicate that QET takes place along a trajectory near the Coulomb trajectory. QET are made to be connected with interaction radius and most of the cross section ratios were reproduced well by an extended tunneling model.

The tendency towards equilibration of the N/Z value and the energy damping, which are the characteristic features of DIT, are found only in the production of Au isotopes. Damped components of projectile-like products observed exhibited a behavior resembling that of QET; the features of the reaction had little dependence on the scattering angle. Then it was concluded that they were produced in a very short interaction time. Cross sections of those products were reproduced by the sum rule model better than by the diffusion model and their total kinetic energies can also be explained well by a model using recoil formula by Siemens et al. with an assumption of short time interaction. All the consequencies presently obtained strongly indicate that the interaction between projectile and target takes place almost instantaneously in a highly mass-asymmetric composite system. The interaction time is so short that the effect of rotation of the dinuclear system or diffusion of nuclear matter is not prominent even in the strongly damped collision like DIT.

REFERENCES TO SECTION 2

1. Schröder, W. U., Huizenga, J. R.: Ann. Rev. Nucl. Sci. 27, 465 (1977)
2. Lefort, M., Ngô, Ch.: Ann. Phys. (Paris) 3, 5 (1978)
3. Volkov, V. V.: Phys. Rep. 44, 93 (1978)
4. Gobbi, A., Nörenberg, W.: Heavy Ion Collisions. Bock, R. (ed.), Vol. 2, pp. 127-273. Amsterdam, New York, Oxford: North-Holland 1980
5. Bass, R.: Nuclear Reactions with Heavy Ions. Texts and Monograghs in Physics. Berlin, Heidelberg, New York: Springer-Verlag 1980
6. Moretto, L. G., Schmitt, R. P.: Rep. Prog. Phys. 44, 533 (1981)
7. Moretto, L. G.: Nucl. Phys. A409, 115c (1983)
8. Breit, G., Ebel, M. E.: Phys. Rev. 103, 679 (1956)
9. Breit, G., Ebel, M. E.: Phys. Rev. 104, 1030 (1956)
10. Nörenberg, W.: Phys. Lett. 52B, 289 (1974)
11. Nörenberg, W.: Z. Phys. A274, 241 (1975)
12. Ayik, S., Schürmann, B., Nörenberg, W.: Z. Phys. A279, 145 (1976)
13. Ayik, S., Schürmann, B., Nörenberg, W.: Z. Phys. A277, 299 (1976)
14. Schmidt, R., Toneev, V. D., Wolschin, G.: Nucl. Phys. A311, 247, (1978)
15. Wolschin, G., Nörenberg, W.: Z. Phys. A284, 209 (1978)
16. Riedel, C., Wolschin, G., Nörenberg, W.: Z. Phys. A290, 47 (1979)
17. Agarwal, S.: Z. Phys. A297, 41 (1980)
18. Běták, E., Toneev, V. D.: J. Phys. G: Nucl. Phys. 9, 147 (1983)
19. Gelbke, C. K., Olmer, C., Buenerd, M., Hendrie, D. L., Mahoney, J., Mermaz, M. C., Scott, D. K.: Phys. Rep. 42, 311 (1978)
20. Wald, S., Gazes, S. B., Albiston, C. R., Chan, Y., Harvey, B. G.,

Murphy, M. J., Tserruya, I, Stokstad, R. G., Countryman, P. J., Van Bibber, K., Homeyer, H.: Phys. Rev. C32, 894 (1985)

21. Wilczyński, J., Siwek-Wilczyńska, K., Van Driel, J., Gonggrijp, S., Hageman, D. C. J. M., Janssens, R. V. F., Łukasiak, J., Siemssen, R. H.: Phys. Rev. Lett. 45, 606 (1980)
22. Wilczyński, J., Siwek-Wilczyńska, K., Van Driel, J., Gonggrijp, S., Hageman, D. C. J. M., Janssens, R. V. F., Łukasiak, J., Siemssen, R. H., Van der Werf, S. Y.: Nucl. Phys. A373, 109 (1982)
23. Hata, K.: to be published in INDC report.
24. Reus, U., Westmeier, W.: At. Data Nucl. Data Tables 29, 1 (1983)
25. Shirley, V. S.:Nucl. Data Sheets 32, 593 (1981)
26. Lederer, C. M., Shirley, V. S. ed.: Table of Isotopes, 7th ed. New York, Chichester, Brisbane, Toronto: Wiley 1978
27. Ishimori, T., Kimura, K., Nakamura, E., Watanabe, K., Fujino, T. Akatsu, J., Ono, R., Murakami, H., Izumi, T., Tsukuechi, K., Kobune, T., Osakabe, T., Ueno, K., Chang, C.-T., Cheng, W.-P., Chen, Y.-M., Sammour, H. M.: JAERI 1047 (1963)
28. Emery, J. F., Leddicotte, G. W.: NAS-NS 3036 (1961)
29. Ewart, A., Valentine, C., Blann, M.: Nucl. Phys. 69, 625 (1965)
30. Kratz, J. V., Poitou, J., Brüchle, W., Gäggeler, H., Schädel, M., Wirth, G., Lucas, R.: Nucl. Phys. A357, 437 (1981)
31. Friedlander, G., Kennedy, J. W., Macias, E. S., Miller, J. M.: Nuclear and Radiochemistry, 3rd ed., pp. 319-321. New York, Chichester, Brisbane, Toronto: Wiley 1981
32. Bohr, N.: Phil. Mag. 25, 10 (1913)

33. Kikuchi, S., Tomita, Y., Kawarasaki, Y., Ohuchi, I., Takeuchi, S., Maruyama, M.: JAERI-M 9136 (1980)

34. Tomita, Y.: JAERI-M 9283 (1980)

35. Knoll, G. F.: Radiation Detection and Measurement, pp. 399-401. New York, Chichester, Brisbane, Toronto, Singapore: Wiley 1979

36. Bass, R.: Nuclear Reactions with Heavy Ions. Texts and Monograghs in Physics. pp. 401-402. Berlin, Heidelberg, New York: Springer-Verlag 1980

37. Igarashi, M.: INS-PT-26 (1970)

38. Wapstra, A. H., Audi, G.: Nucl. Phys. A432, 1 (1985)

39. Gatty, B., Guerreau, D., Lefort, M., Pouthas, J., Tarrago, X., Galin, J., Cauvin, B., Girard, J., Nifenecker, H.: Z. Phys. A273, 65 (1975)

40. Artukh, A. G., Adveichikov, V. V., Erö, J., Gridnev, G. F., Mikheev, V. L., Volkov, V. V., Wilczyński, J.: Nucl. Phys. A160, 511 (1971)

41. Bondorf, J. P., Dickmann, F., Gross, D. H. E., Siemens, P. J.: J. de Phys. Colloq. 32, C6-145 (1971)

42. Gilbert, A., Cameron, A. G. W.: Can. J. Phys. 43, 1446 (1965)

43. Mathews, G. J., Wozniak, G. J., Schmitt, R. P., Moretto, L. G.: Z. Phys. A283, 247 (1977)

44. Moretto, L. G., Schmitt, R. P.: J. Phys. Suppl. C5, 109 (1976)

45. Wilczyński, J., Siwek-Wilczyńska, K.: Phys. Lett. 55B, 270 (1975)

46. Wilczyński, J., Siwek-Wilczyńska, K.: Phys. Lett. 74B, 313 (1978)

47. Siemens, P. J., Bondorf, J. P., Gross, D. H. E., Dickmann, F.: Phys. Lett. 36B, 24 (1971)

3. COMPOUND FORMATION CROSS SECTION AND ANGULAR MOMENTUM DEPENDENT FISSION BARRIER

3.1. INTRODUCTION

Compound formation is a most elementary idea of the nuclear reaction, which has met much success in the light-ion induced reaction. The idea conceives the process that the projectile kinetic energy is distributed randomly among all nucleons in the fused system and the memory of the entrance channel is completely lost in the compound nucleus. The resulting nucleus called the compound nucleus is in an excited quasi-stationary state. The compound nucleus at the excited state decays via either particle emission such as photon (γ-ray radiation), neutron, proton, α particle, etc. or nuclear fission. The life time of the compound nucleus is relatively long (typically 10^{-14} to 10^{-19} s) compared to the time for a nucleon to traverse the nucleus (typically 10^{-20}-10^{-23} s) [1].

In the heavy-ion induced reaction, the compound nucleus is considered to be formed also although there are features somewhat different from the light-ion induced reaction. Both the target and the projectile must be treated as nuclei having internal degrees of freedom in the case of heavy-ion reactions. Then kinetic energy and angular momentum of the relative motion are transferred into the intrinsic degrees of freedom in the composite system formed when nuclear matter distributions of the two nuclei overlap. Finally the composite system evolves to a compound nucleus [2]. The inter-

nuclear potential related to the process is a function of the separation of the two nuclei, the angular momentum of the system, and the deformation of the two nuclei or the composite system . In addition, there should be a critical angular momentum for fusion, at which the two interacting nuclei fail to fuse, and it is associated with the internuclear potential [2]. Therefore the fusion cross section, which is determined by the critical angular momentum, is an important clue to investigate the internuclear potential.

Nuclear fission is also a noticeable object since it is an important decay process of the compound nucleus with a high angular momentum, which is a characteristic feature of the heavy-ion induced reaction. The fission barrier height of a nucleus decreases with increase of its intrinsic angular momentum through the effect of the centrifugal force as shown schematically in Fig.3.1. The fission barrier dependent on angular momentum was formulated for the first time in a rotating liquid drop model (RLDM) proposed by Cohen et al. [3]. In order to confirm validity of the model, many authors compared observed excitation functions of fission and/or evaporation residue formation [4-17] with prediction by statistical calculations with the RLDM barriers. The calculations are, however, not found to reproduce observed data in the mass region lighter than about 200 and the authors are contented with reduction of the barrier height by an appropriate factor which changes rather arbitrarily from work to work. Generally speaking the factor is between 0.55 and 0.85 [14]. Recently a rotating finite range model (RFRM) [18,19] which was proposed as a refinement of RLDM gave a theoretical foundation for the reduction of the RLDM

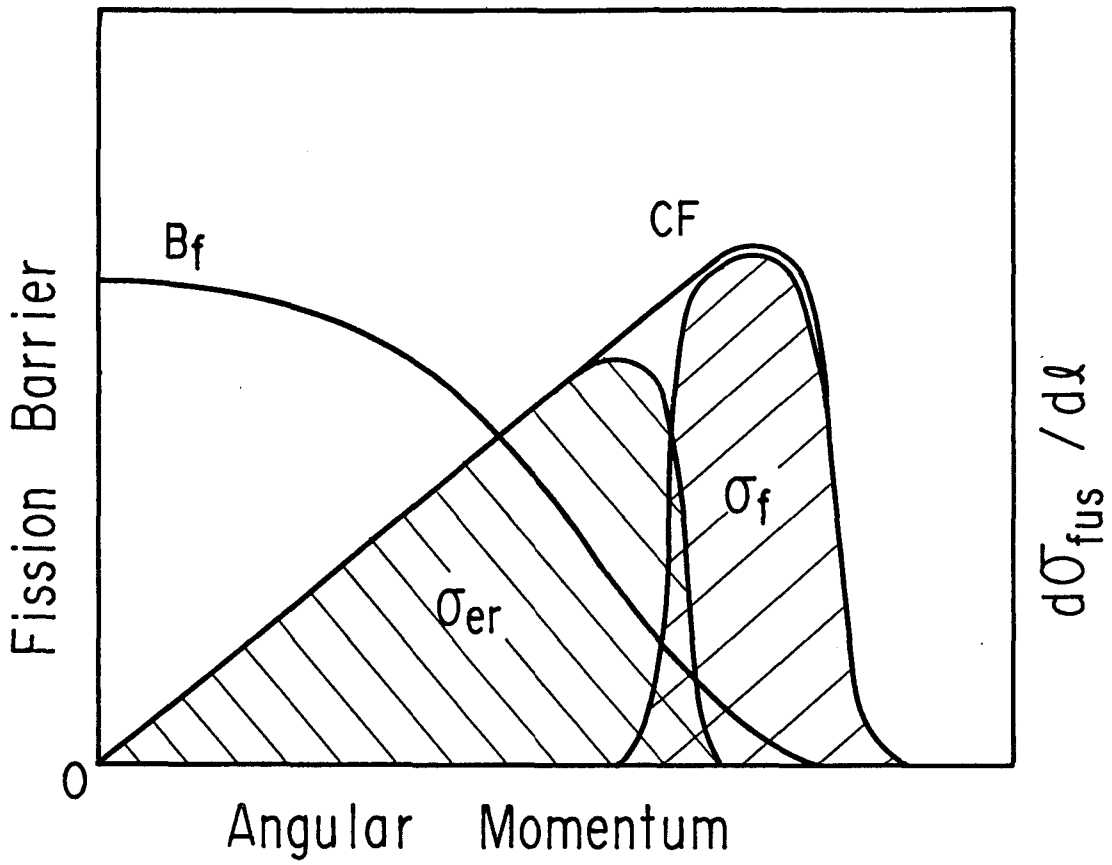

Fig.3.1. Schematic illustration of dependence on the angular momentum of the fission barrier height (B_f) and the partial cross section for compound formation (CF). The symbols σ_{er} and σ_f represent the cross sections of evaporation residue formation and fission, respectively.

barrier. Fission barriers predicted by the model were also applied to analysis of fission data in various composite systems [14,20-22] and good agreement between calculation and experiment was attained without any scaling.

In this section, I like to mark two combinations of target and projectile, namely, ^{16}O on ^{197}Au and ^{12}C on ^{197}Au for which fairly reliable data of the fission excitation function [23,24] are already available, while there are also some works on the excitation functions of evaporation residues. For the $^{197}Au+^{16}O$ reaction, Natowitz [25] and Hinde et al. [26] have measured total evaporation cross sections, yet there are large discrepancies between the cross sections in the two works. I felt that it might need to be reexamined. For the $^{197}Au+^{12}C$ reaction, there are three radiochemical works [27-29] published on the excitation functions of evaporation residues. There are, however, considerable deviations among them and furthermore amendment of the published data may be necessary according to the alteration of the decay properties of some astatine isotopes.

Excitation functions of (HI,xn), (HI,pxn), and (HI,α xn) reactions for the above two reaction systems were measured to deduce the total evaporation cross section σ_{er}. Recoil range measurements were also carried out in order to eliminate the possible admixture of non-fusion-evaporation components in σ_{er}.

The fusion cross section obtained as the sum of the evaporation cross section and the fission cross section is discussed for the two reaction systems with the calculation by the Bass model [30] and the extra-push

model [31]. Then the obtained data were also analyzed from the viewpoint of the fission-evaporation competition. This is attained by a statistical calculation with the RFRM fission barriers. Moreover a fission barrier at a specified J window will be deduced experimentally and compared with the fission barriers by model prediction.

3.2. EXPERIMENTAL

3.2.1. Radiochemical Method

The activation method was applied to the measurement of compound formation cross sections. The method was described in detail in the measurement of target-like products in 2.2. 1μm-thick Au target and an Al catcher foil were mounted on a Faraday cup at the R-2 course and bombarded with ^{16}O or ^{12}C beam from the tandem accelerator of JAERI. The energies incident to the Au target ranged from 5 to 8MeV/u. The cumulative cross sections were measured by γ-ray spectrometry for $^{209-207}Rn$, $^{209-203}At$, $^{207-203}Po$ and $^{205-202}Bi$ nuclides in the ^{16}O-induced reaction. Yields of nuclides are determined for each piece of the Au target foil and the Al catcher foil. Chemical separation was applied in the yield measurement when it was needed.

For the ^{12}C-induced reaction, γ-rays of At, Po, and Bi nuclides in the target and the catcher were also measured. The independent yields were measured for At nuclides produced in the xn reactions while the others were determined as cumulative yields. Decay properties given in [32] were used for deduction of cross sections of the nuclides.

3.2.2. Measurement with ISOL and a He-Jet Transport System

Fr nuclides produced in the (^{16}O, xn) reactions are α-ray emitters of short half-lives (< 3 min); some of them possess similar half-lives and consequently emit α rays with similar energies to one another as presented in Table 3.1 [33]. Individual yields of Fr can not be determined by off-line spectrometry. In the present work relative yields of the Fr nuclides were measured with an isotope separator on-line (ISOL) [34] installed at the R-1 course of the tandem Van de Graaff accelerator as shown in Fig.3.2(a). The ISOL experiment was performed as follows. Produced nuclei of Fr recoiling out from the gold target were stopped in a catcher foil in the surface-ionization ion source easily ionizing alkali metal elements (see Fig.3.2(b)). The Fr ions were transported into the electromagnetic field and separated with the resolution $\Delta A/A$ of 400, and Fr nuclei of a given mass were collected on a aluminum-coated Mylar tape for 60 seconds. Then they were moved to the detecting position faced by a silicon semiconductor detector (SSD) and measurement of the emitted α rays was performed as shown in Fig.3.2(c). The sweep time of the ionization source was estimated to be about 1 sec, which was sufficiently short compared to the half-lives of the $^{206-210}$Fr nuclides. The amount of the contaminated isotope was estimated from the α-ray intensity of its daughter nuclide, when it could not be distinguished from the nuclide of interest by the decay properties. Admixture with the nuclei of adjacent mass was less than 0.1% of the total yield of the adjacent isotope.

Measurement of the correct yields of Fr requires constancy of the beam intensity incident to the target and the collection efficiency in the ISOL because they could not be observed during the measurement. Stability of the

Table 3.1. Decay properties of Fr nuclides [33]

Nuclides	Half life	Eα (MeV)	Emission rate of α-ray per decay	Daughters
^{210}Fr	3.18 m	6.572	1.00*	^{206}At
^{209}Fr	50 s	6.646	0.89	^{205}At, ^{209}Rn
^{208}Fr	58 s	6.636	0.74	^{204}At, ^{208}Rn
^{207}Fr	14.8 s	6.761	0.93	^{203}At, ^{207}Rn
^{206}Fr	16.0 s	6.785	0.85	^{202}At, ^{206}Rn

* This is a tentative value.

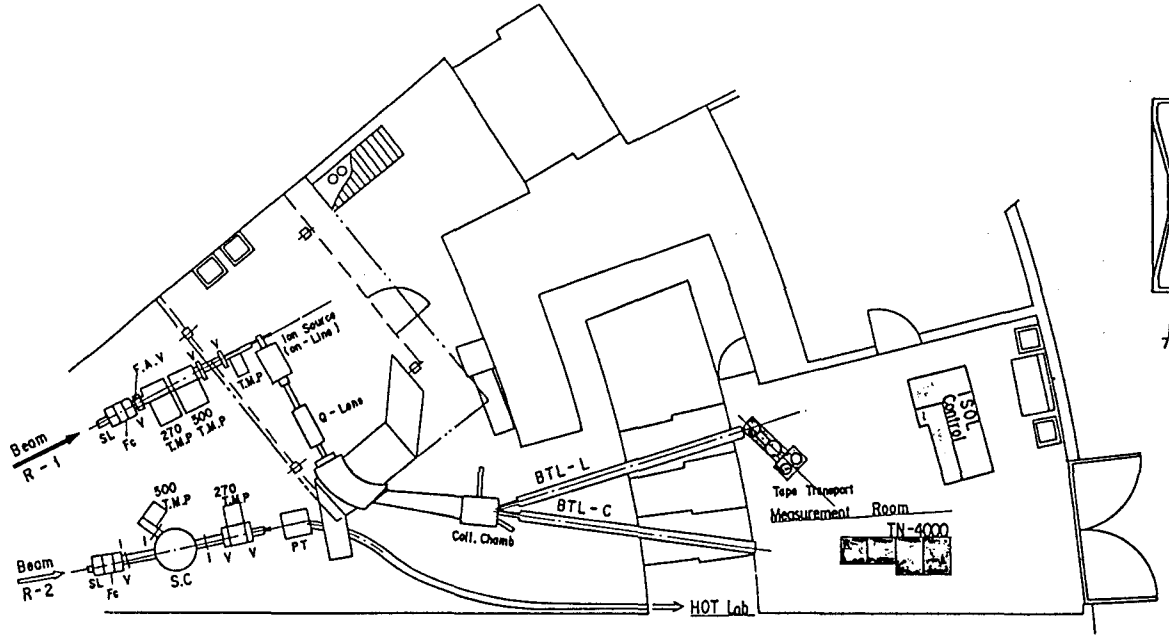

(a)

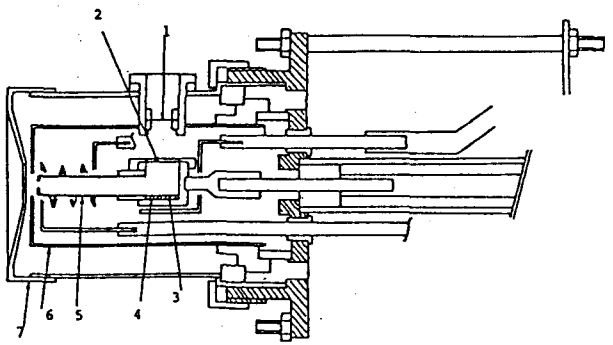

(b) Surface ionization source (1) target, (2) carbon foil, (3) carbon catcher, (4) vaporizer, (5) ionizer, (6) inner heat-shield, (7) outer heat-shield

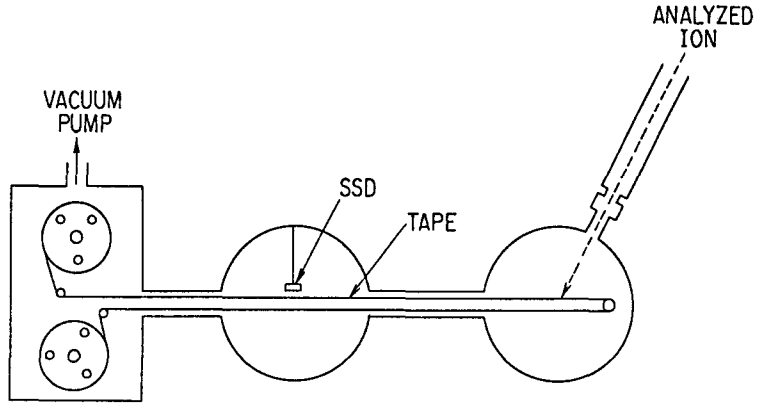

(c)

Fig.3.2. A system for the measurement of Fr nuclides. An isotope separator on line (ISOL) installed at R-1 course of the tandem Van de Graaff accelerator (a), a surface-ionization ion source of the ISOL (b), and a tape transport system furnished with a silicon semiconductor detector (c) are shown.

beam intensity was monitored with the electric current of the Faraday cup during the intermission of the measurements. The measurement was repeatedly carried out to estimate the fluctuation of the over-all collection efficiency in the ISOL although the efficiency itself could not be determined. Finally, this method was found to be useful in the measurement of the relative yields of Fr.

Besides the ISOL experiment a supplementary measurement of the Fr nuclides was carried out with a He-jet transport system [35] to obtain the relative yields of ^{209}Fr and ^{210}Fr and to confirm the results of the ISOL experiment. As depicted in Fig.3.3, produced nuclei recoiled into a chamber filled with He gas and stopped there. Then nuclei attached to aerosol particles, which were made of vaporized NaCl and vaporized dioctyl phthalate, and were transported through Teflon capillary (2mm in diameter and 30m long) by He-gas flow due to suction by a vacuum pump. Then He jet was blown to the tape for collection of aerosol particles for an appropriate time. Finally the tape was moved in front of a silicon semiconductor detector for the measurement of α rays from the Fr nuclides. The sweep time is estimated to be about 5s. Correction due to the decay of the products was taken into account to deduce relative yields of Fr.

3.2.3 Rapid α-ray Measurement

α-ray measurements were also carried out by means of a detection system of Fig.3.4 for all the α emitters which recoiled out from the target

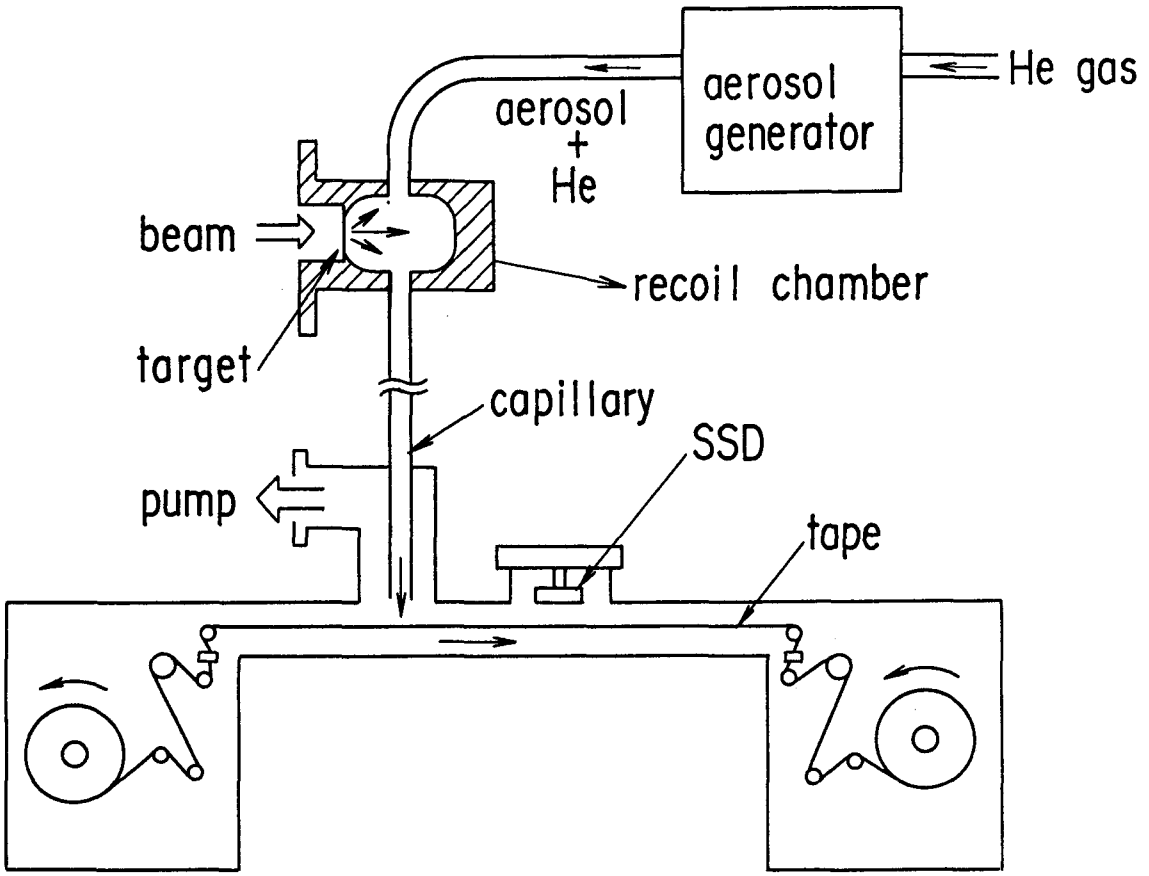

Fig.3.3. Experimental set-up of a He-jet transport system.

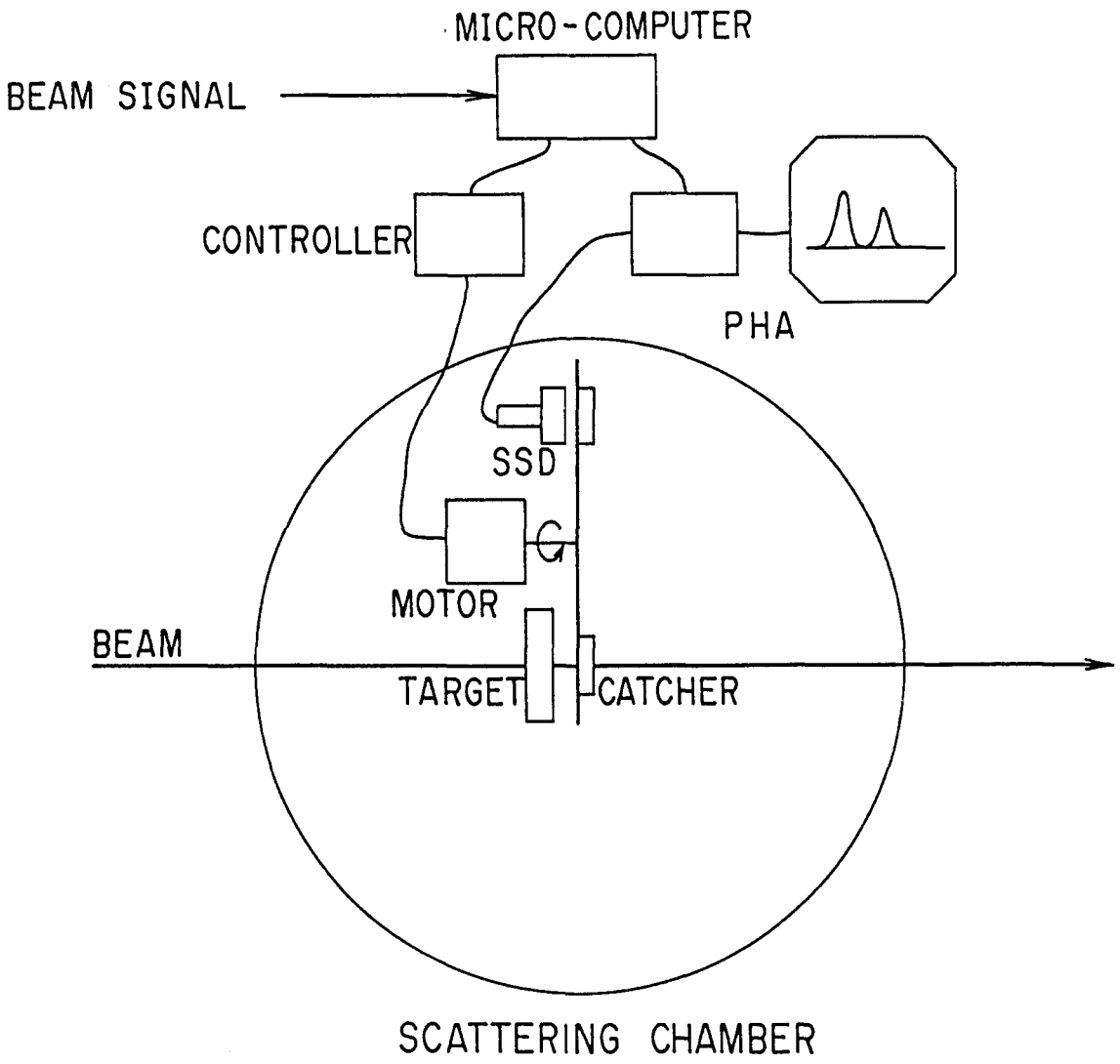

Fig.3.4. Experimental set-up in a scattering chamber for the measurement of α ray from all α emitters which recoiled out from the target and were caught by an Al foil.

and were caught by an Al foil. The catcher foil mounted on a rotating wheel was moved to the position of the silicon semiconductor detector after the irradiation for 60 sec, and the α-ray measurement was started one second later. From the decay analysis of the α-ray activity, the yields of $^{206}Fr+^{207}Fr$, $^{208}Fr+^{209}Fr$ and ^{210}Fr were determined relative to that of the Rn or At nuclide whose cumulative cross section was known from the γ-ray spectrometry. The fraction of recoiling nuclei for all the evaporation residues was assumed to be the same.

Finally, the absolute cross sections of the Fr nuclides were deduced from the relative yields descrived in 3.2.2 together with the results of this experiment and the relevant cumulative yields by γ-ray spectrometry. The decay data of Fr listed in Table 3.1 [33] were used for the calculation.

3.3. RESULTS

3.3.1. Excitation Functions of Evaporation Residues by γ-ray Spectrometry in the ^{16}O- and ^{12}C-Induced Reactions

Figure 3.5 shows the cumulative yields of $^{203-207}Po$ and $^{208,209}At$ nuclides used for deduction of the total cross section of evaporation residues in the ^{16}O-induced reaction. Details of the procedure are described in 3.3.4. One can see in the figure complicated shapes of the excitation functions especially for Po nuclides. It implies that they are produced via several reaction paths.

As for the ^{12}C-induced reaction, excitation functions for At nuclides produced in the xn reactions (x=3-6) are shown in Fig.3.6. The absolute errors for cross sections are within the size of the marks in the figure. Of the published works for the reactions up to date [27-29], the data by Bimbot et al. [28] agreed best with the present work, if their results are corrected with the decay properties given in [32]. Their data are also presented in Fig.3.6. As shown in the figure, the xn reactions have regularity in relation to the projecting energy. The xn reactions with x=3-6 occur successively as peaks with similar widths. Fig.3.7 shows cumulative yields of $^{203-206}Po$, most of which are likely to be produced in the decay of the At precursors.

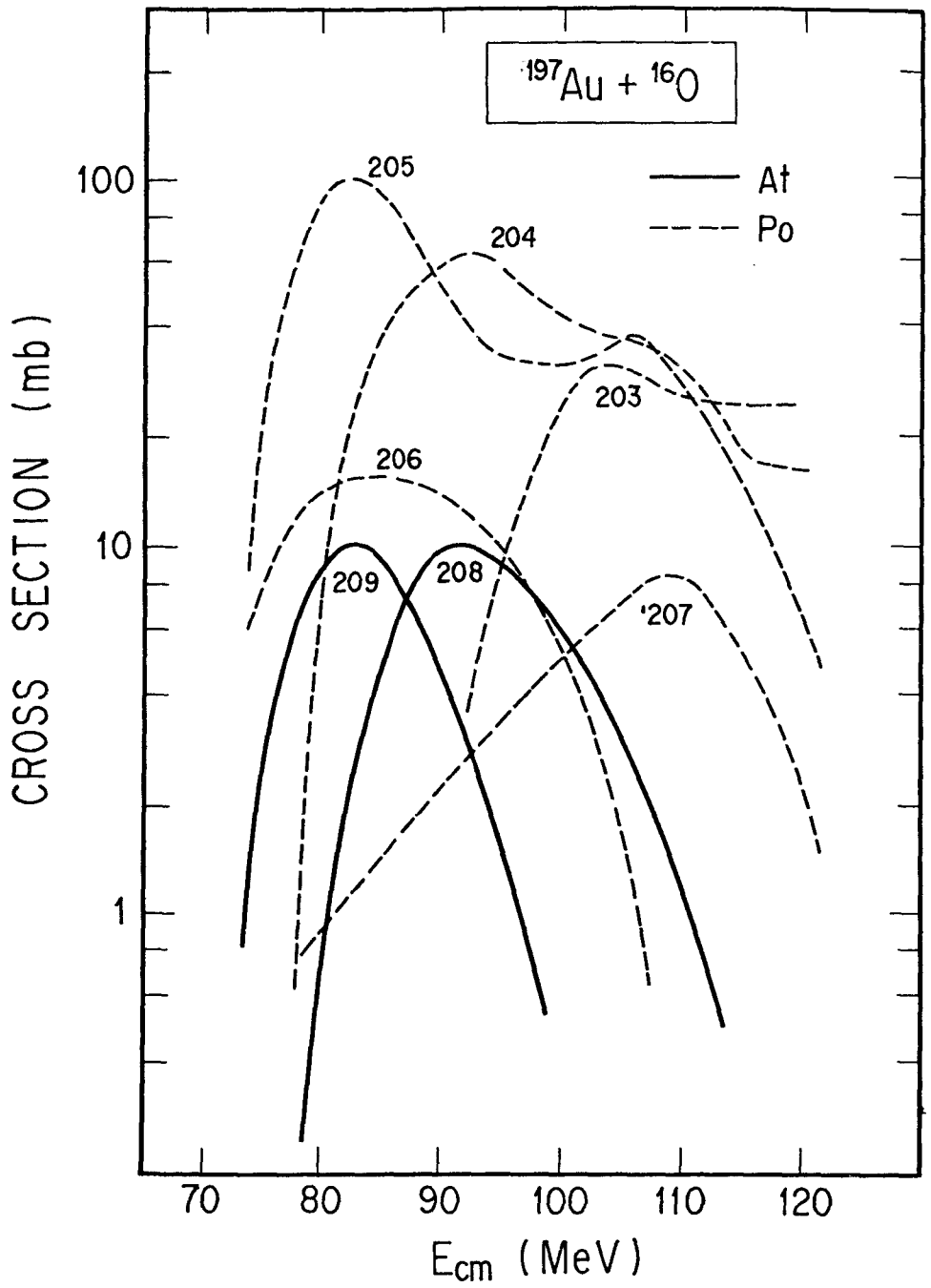

Fig.3.5. Cumulative yields of At and Po nuclides used for deduction of the total cross section of evaporation residues in the ^{16}O-induced reaction.

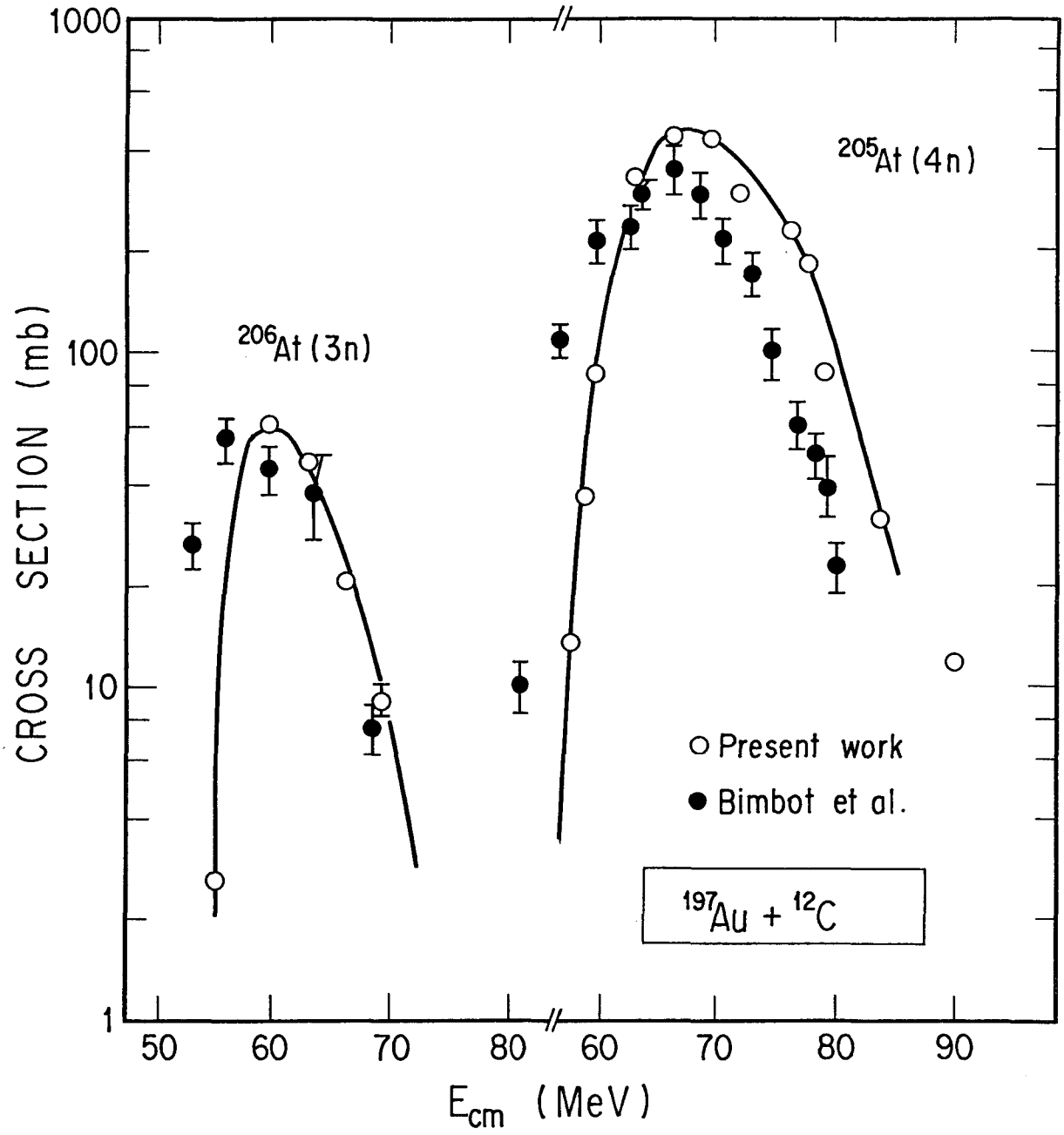

Fig.3.6(a). Excitation functions for At nuclides produced in the xn reactions (x=3,4) induced by ^{12}C. Absolute errors for the cross sections are within the size of the marks in the figure. The data by Bimbot et al. [28] corrected with the decay properties in [33] are shown as well.

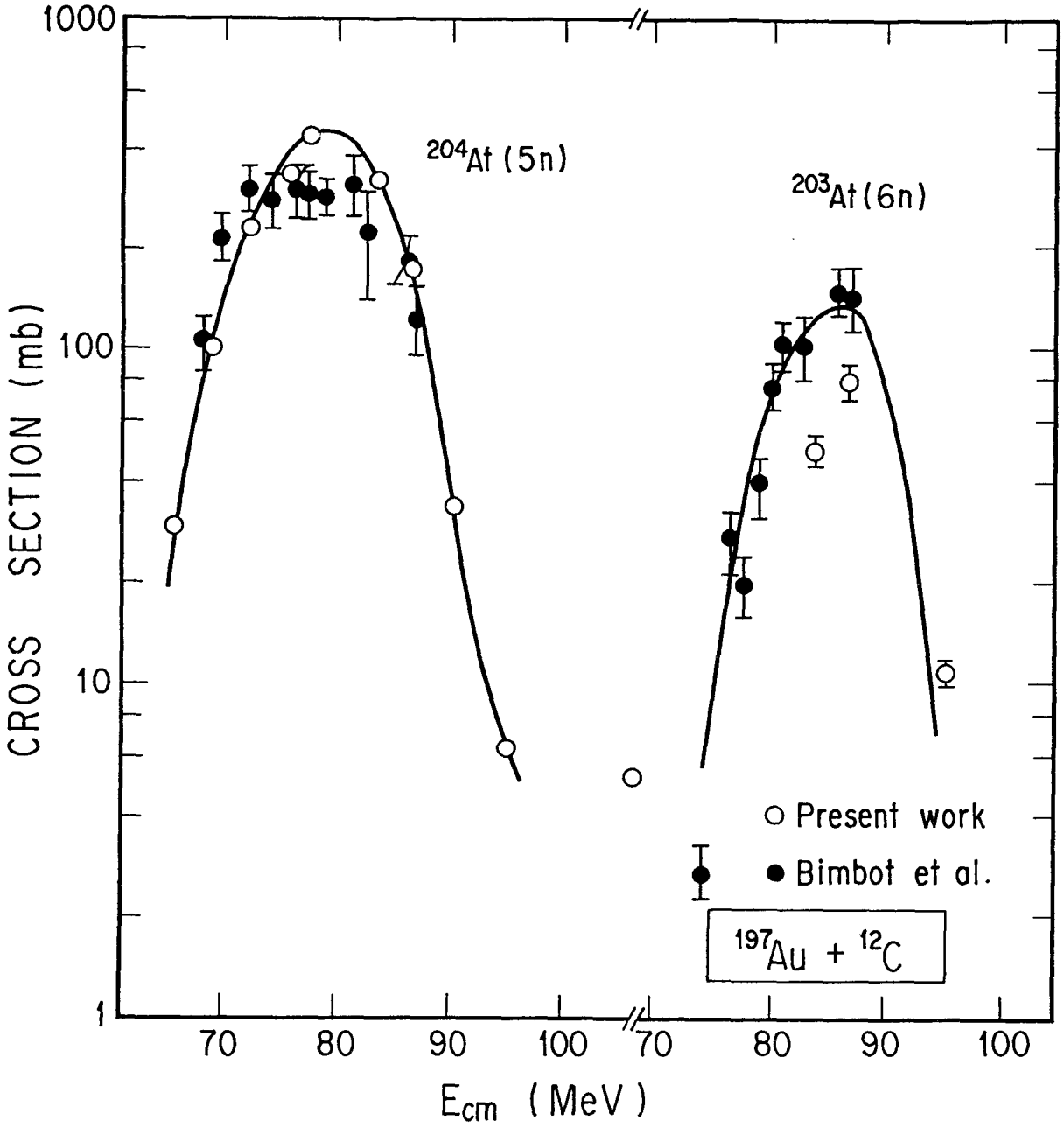

Fig.3.6(b). Excitation functions for At nuclides produced in the xn reactions (x=5,6) induced by ^{12}C. See caption Fig.3.6(a).

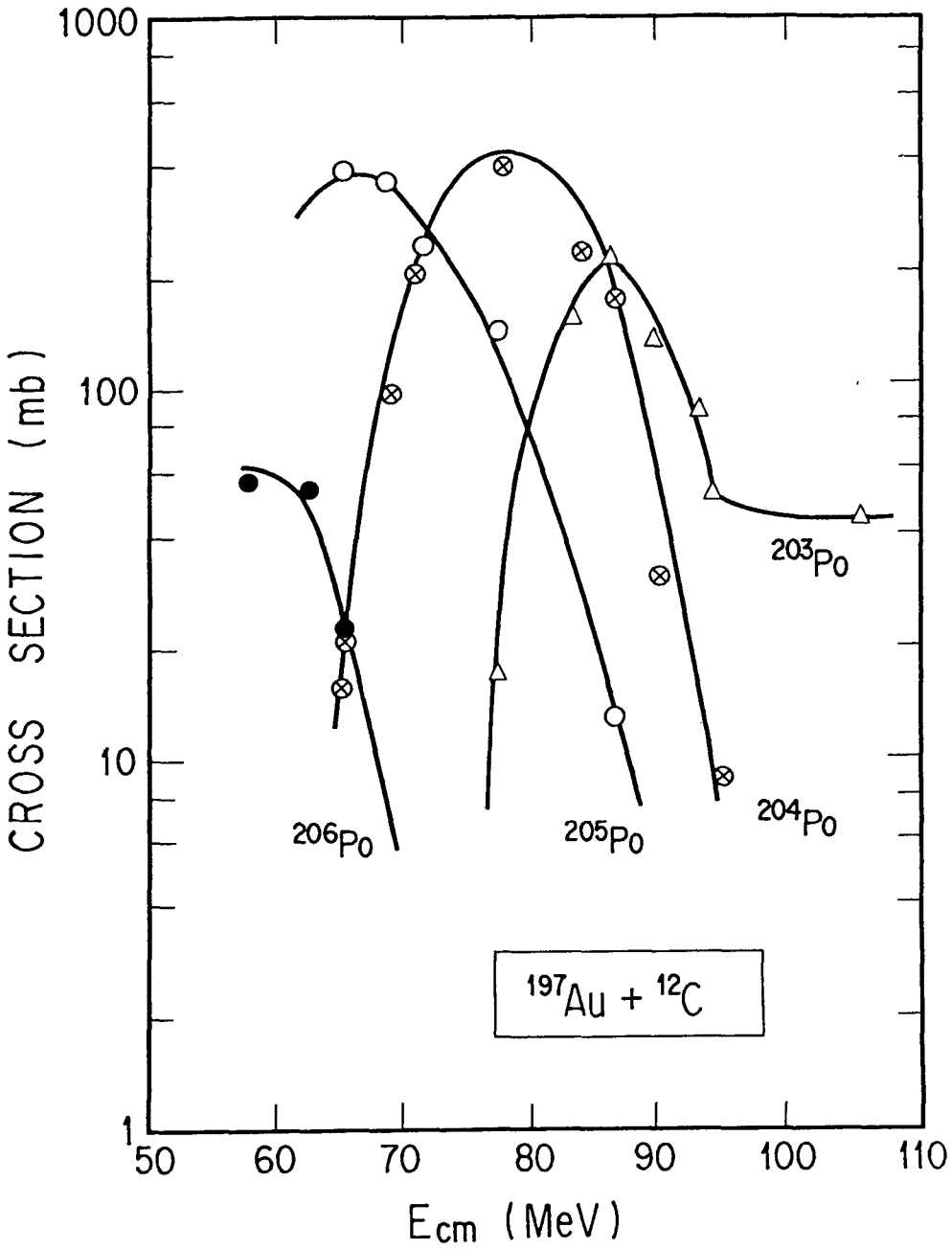

Fig.3.7. Cumulative yields of $^{203-206}$Po nuclides for the ^{12}C-induced reaction.

3.3.2. Projected Recoil Ranges of Evaporation Residues in the ^{16}O- and ^{12}C-Induced Reactions

Projected mean recoil ranges calculated with Eq.(2.6) [36] are shown in Fig.3.8 for the same nuclides as those presented in 3.3.1 in the ^{16}O-induced reaction. They agree with calculation on the basis of the full momentum transfer reaction within the experimental uncertainties, except for ^{207}Po and ^{203}Po whose yields were too small to give reliable consequences. The calculation was carried out with the formula:

$$E_R = A_P/(A_P + A_T)E_P, \qquad (3.1)$$

where E_R and E_P are the recoil energy of the product and the projectile energy, respectively, and A_P and A_T are the masses of projectile and target, respectively. The calculated energy was depicted as ranges in the matrix of Au in the figure. Conversion from energy to range was performed with the OSCAR code [37]. Agreement of calculation and the data represents that the nuclides are produced via the compound nuclues in which the projecting kinetic energy was completely damped. As to ^{207}Po and ^{203}Po, they are also likely to be produced predominantly via the compound nucleus considering that surrounding nuclides in the nuclear chart provide a well-established ground for the almost complete contribution of the compound decay. Therefore $^{203-207}Po$ and $^{208,209}At$ nuclides are concluded to be produced in the compound formation.

Dependence of the recoil ranges for $^{203-206}Po$ in the ^{12}C-induced

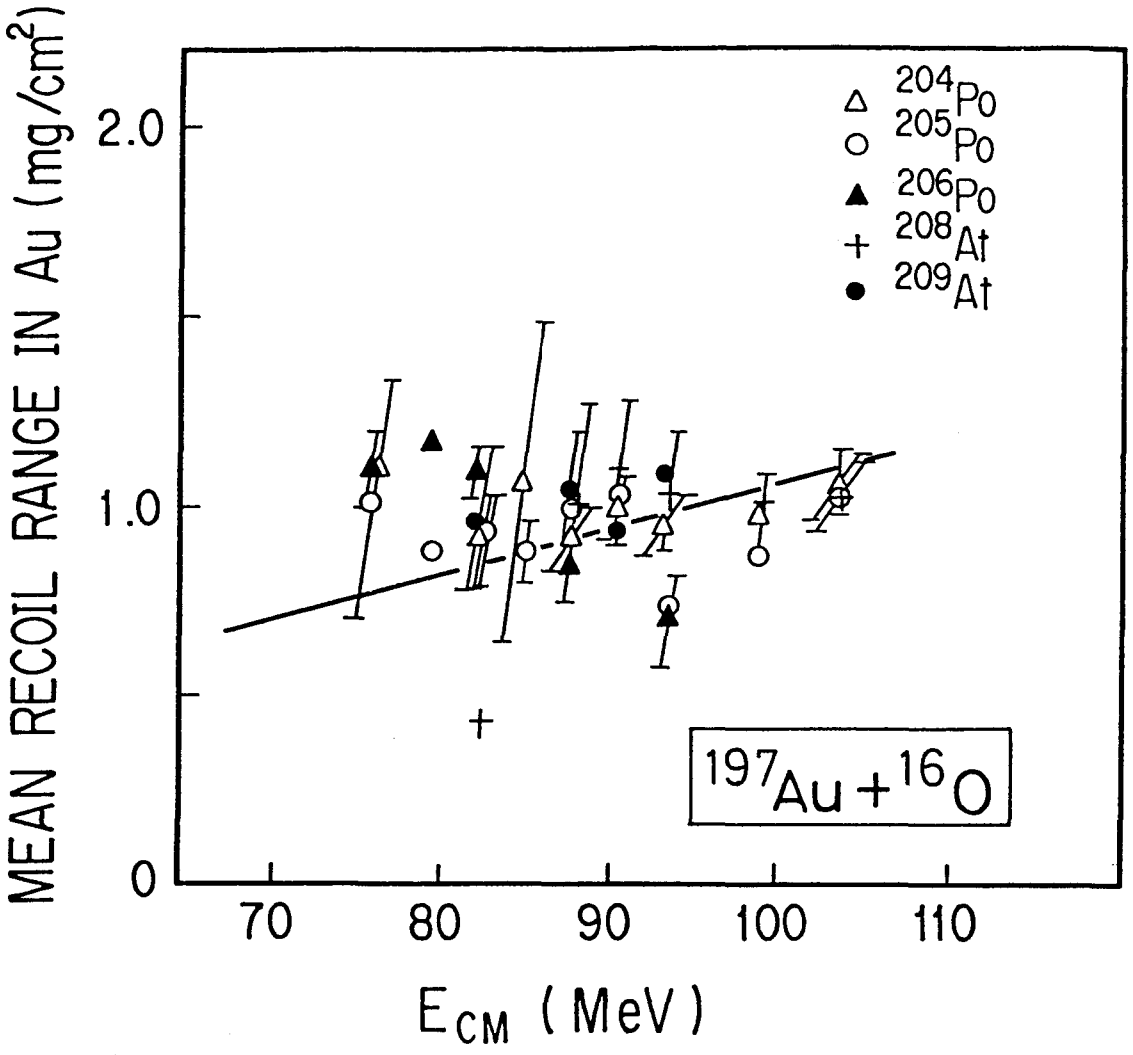

Fig.3.8. Mean projected recoil ranges for At and Po nuclides used for deduction of the total cross section of evaporation residues in ^{16}O-induced reaction. A solid line represents the calculated range on the assumption of full momentum transfer.

reaction exhibits a feature of full-momentum transfer reactions as presented in Fig.3.9(a). The Ranges of ^{202}Bi are shown in Fig.3.9(b) as an example of products via the transfer process. The feature that the range decreases with increase of the energy is characteristic among products in the transfer reaction as described in 2.3.3. Therefore the observed Po nuclides are concluded to be produced via the compound nucleus because of the same reason as for the ^{16}O-induced reaction.

3.3.3. Excitation Functions of Fr nuclides in the ^{16}O-Induced Reaction

Fig.3.10 shows yield ratios between several pairs of Fr nuclides obtained from the measurement with the ISOL and the above-mentioned He-jet transport system. The overall uncertainties of the cross sections are about ± 20%, a large part of which comes from the ISOL measurement. As to the ratio of ^{210}Fr/^{209}Fr, the result with the He-jet transport system reproduced the result with ISOL. Figure 3.11 shows excitation functions of Fr nuclides produced in the (^{16}O,xn) reactions (x=3 to 7) which were deduced by using the yields ratios shown in Fig.3.10. Excitation functions of the xn reactions show a fairly regular relationship with respect to the projecting energy as well as those for the ^{12}C-induced reaction.

3.3.4. Deduction of the Total Cross Section of Evaporation Residues

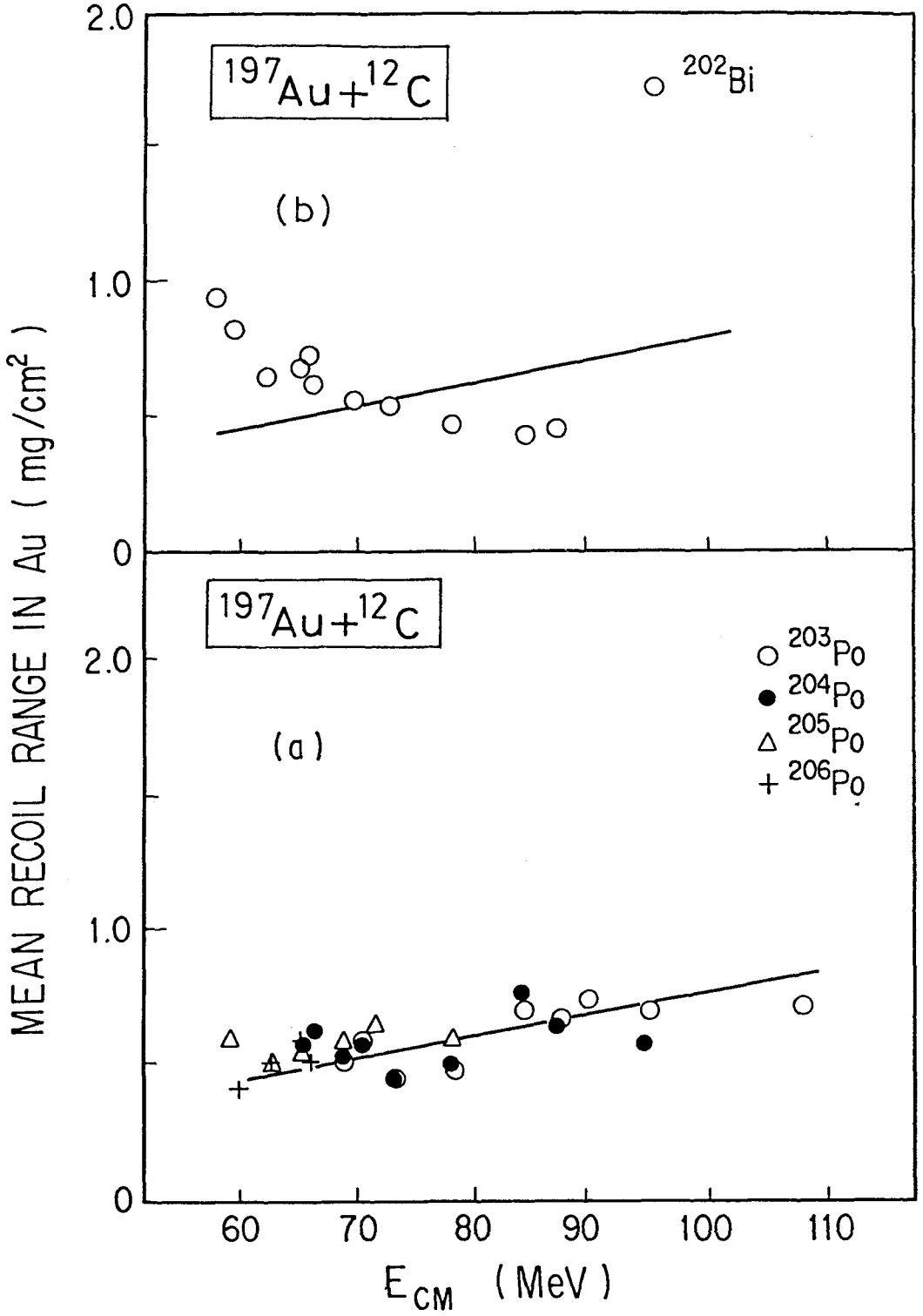

Fig.3.9. Mean projected recoil ranges for $^{203\text{-}206}$Po nuclides (a) and ^{202}Bi nuclide (b) in the ^{12}C-induced reaction. A solid line represents the calculated range on the assumption of full momentum transfer.

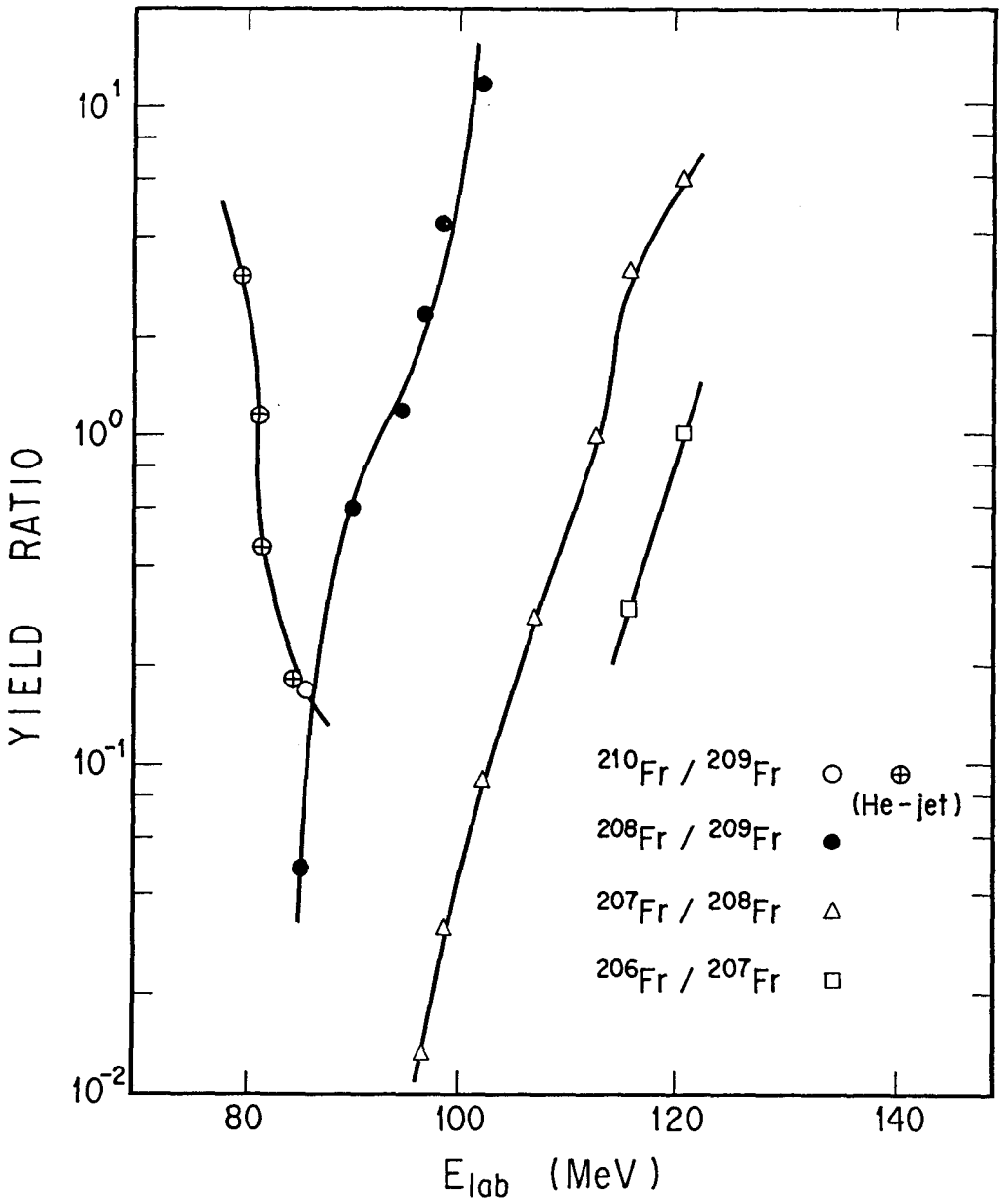

Fig.3.10. The yield ratios between several pairs of Fr nuclides obtained from the measurement with the ISOL and the He-jet transport sytem.

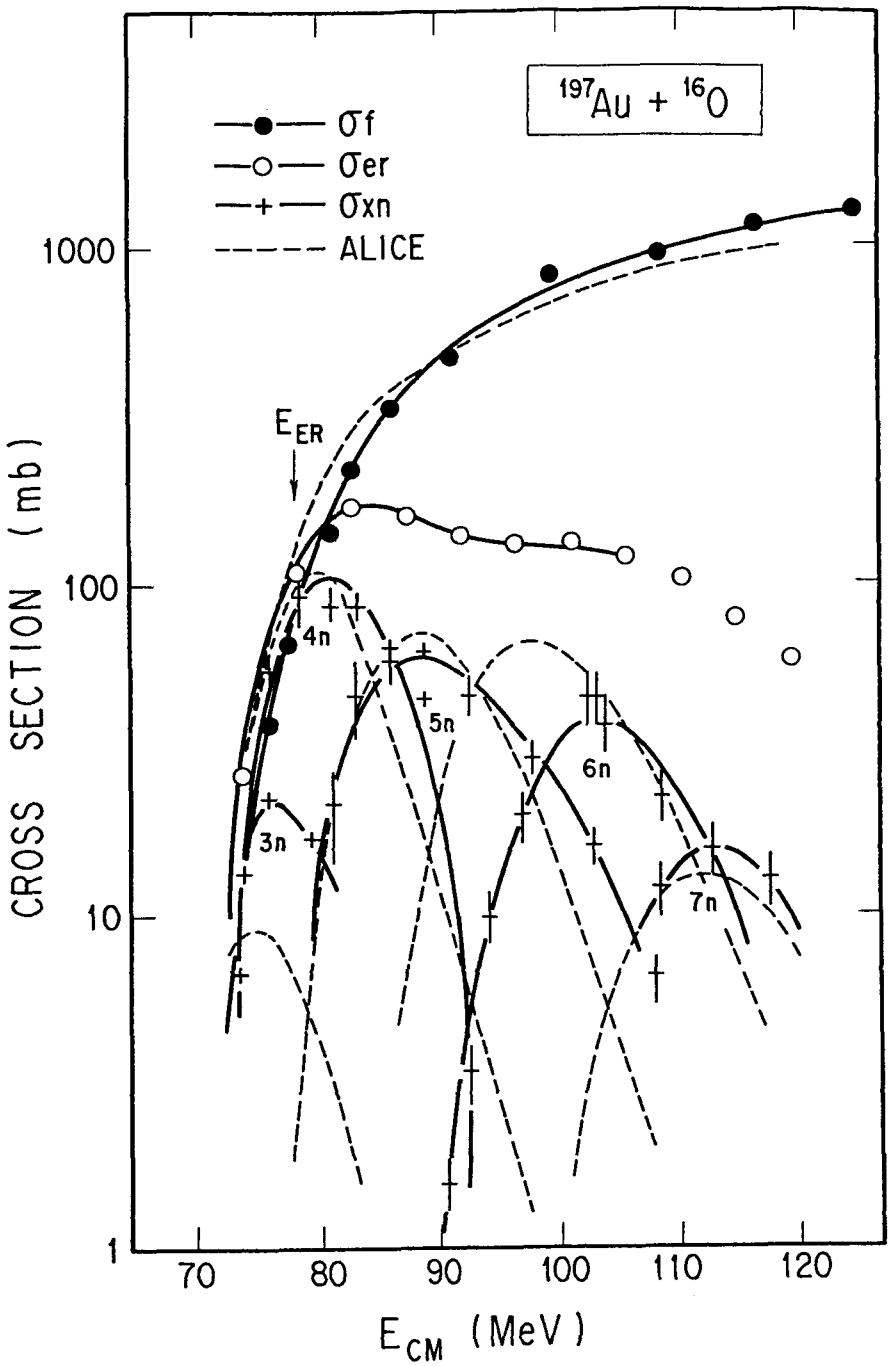

Fig.3.11. Excitation functions of xn reactions (σ_{xn}), formation of total evaporation residues (σ_{er}) and fission (σ_f) [23] for the ^{16}O-induced reaction. See 3.4.4 for the symbol E_{ER} marked with arrow. Solid lines are drawn through the experimental values. Dashed lines represent the excitation function calculated by the ALICE code with the parameters a_f/a_ν = 1.03 and P_{LD} = 18.

For the ^{16}O-induced reaction, the total cross section σ_{er} of evaporation residues was deduced by summing up the cross sections of (^{16}O,xn), (^{16}O,pxn), and (^{16}O,α xn) reactions. Evaporation residues further decay through emission of α ray (α decay) or positron (β^+ decay), or via electron capture (EC decay). Cumulative yields of ^{208,209}At and $^{203-207}$Po cover the sum of the cross sections for xn (x=3-5), pxn (x=2-5), and α xn (x=1-5) reactions, and furthermore contain partially the formation cross sections of 6n and 7n reactions as presented in Table 3.2. The decay routes of ^{207}Fr to ^{203}At (30%) and ^{206}Fr to ^{202}At (90%) are not included there. Accordingly, σ_{er} was determined by adding 30% and 90% of the formation cross sections of ^{207}Fr and ^{206}Fr, respectively, to the sum of the cumulative yields for ^{208,209}At and $^{203-207}$Po. As to a nuclide such as ^{208}At or ^{205}Po, whose decay constant is not much smaller than that of its precursor, growth and decay during the irradiation time were taken into account in calculation of the cumulative yield. The products with the mass numbers less than 202 were disregarded, because the transfer reaction products might begin to mix with them. The deficit due to missing cross sections is considered to be significant at the projectile energies higher than 110MeV.

The resulting excitation function for σ_{er} is shown in Fig.3.11. Three points at E_{cm} larger than 110MeV should be considered to give lower limits for σ_{er}, because some of the cross sections with considerable contribution may be missed as described above. The σ_{er} obtained here gave much smaller values than those of Natowitz [25] measured by using mica track detectors. The discrepancies are remarkable at projectile energy between 95 and 110MeV. The cause of these discrepancies are not clear. It is hardly likely

Table 3.2. Relation of each independent cross section to cumulative cross section for the ^{16}O-induced reaction. Nuclides whose cumulative yields were measured are listed in the first column. Contribution of the reaction channels, namely, xn, pxn, α xn, and α pxn reactions are also listed. The decay data are from [32] and [33].

	xn	pxn	α xn	α pxn
^{209}At	$0.09\times{}^{209}Fr$	$0.83\times{}^{209}Rn$	^{209}At	
^{208}At	$0.12\times{}^{208}Fr$	$0.48\times{}^{208}Rn$	^{208}At	
^{207}Po	$0.05\times{}^{207}Fr$	$0.69\times{}^{207}Rn$	$0.90\times{}^{207}At$	^{207}Po
^{206}Po	^{210}Fr	$0.36\times{}^{206}Rn$	^{206}At	^{206}Po
	$0.05\times{}^{206}Fr$	$0.96\times{}^{210}Rn$		
^{205}Po	$0.82\times{}^{209}Fr$	$0.17\times{}^{209}Rn$	$0.90\times{}^{205}At$	^{205}Po
		$0.69\times{}^{205}Rn$		
^{204}Po	$0.85\times{}^{208}Fr$	$0.52\times{}^{208}Rn$	$0.96\times{}^{204}At$	^{204}Po
		$0.27\times{}^{204}Rn$		
^{203}Po	$0.66\times{}^{207}Fr$	$0.23\times{}^{207}Rn$	$0.69\times{}^{203}At$	^{203}Po

that they come from the incorrectness of the decay properties, or that the cross section missed in summing up is so large in this energy region. I like to put more confidence on the present results rather than the track data. Although Natowitz carefully separated the tracks by evaporation residues from the others by the difference in track length in his measurement using the mica track detector, one cannot discard the possibility of mixing up the true tracks with tracks by other processes such as transfer reactions for example. On the other hand, the cross sections in the present study agree with those of Hinde et al. [26] in magnitude, but the starting energy of the reaction in the present study is a few MeV higher than that by Hinde et al. The source of the discrepancy shall not be discussed any further at present.

Decay chains of evaporation residues for the ^{12}C-induced reaction are much simpler than those for the ^{16}O-induced reaction. In order to obtain the evaporation cross section σ_{er} in this case, the formation cross sections of $^{203-206}At$ and the independent formation cross sections of $^{203-206}Po$ were summed up. (The cross sections obtained by Bimbot et al. [28] with measurement of α rays were used for ^{203}At in the summations, because its α-decay property is known more accurately than the property of γ-ray emission.) The summation covers cross sections for (^{12}C,xn) and (^{12}C,pxn) reactions with x=3-6 and 2-5, respectively. Formation cross sections of the Bi nuclides via the (^{12}C,α xn) reactions were not included by the summed cross section. According to Bimbot et al. [38], a large part of the direct formation of $^{200-203}Bi$ is through the transfer reaction. Furthermore cumulative yields of $^{203-205}Bi$ agreed with those of $^{203-205}Po$,

respectively, within the experimental uncertainties at the energies lower than 90MeV. This means that $^{203-205}$Bi were formed almost completely via the decay of the precursors of Po and therefore the cross sections for (^{12}C,α xn) reactions with x=0-2 were negligibly small there. The yield of ^{203}Bi began to exceed that of ^{203}Po at the energy greater than 95MeV. The resulted σ_{er}'s are shown in Fig.3.12. There is a possibility of missing some evaporation cross section in the energy around 90MeV.

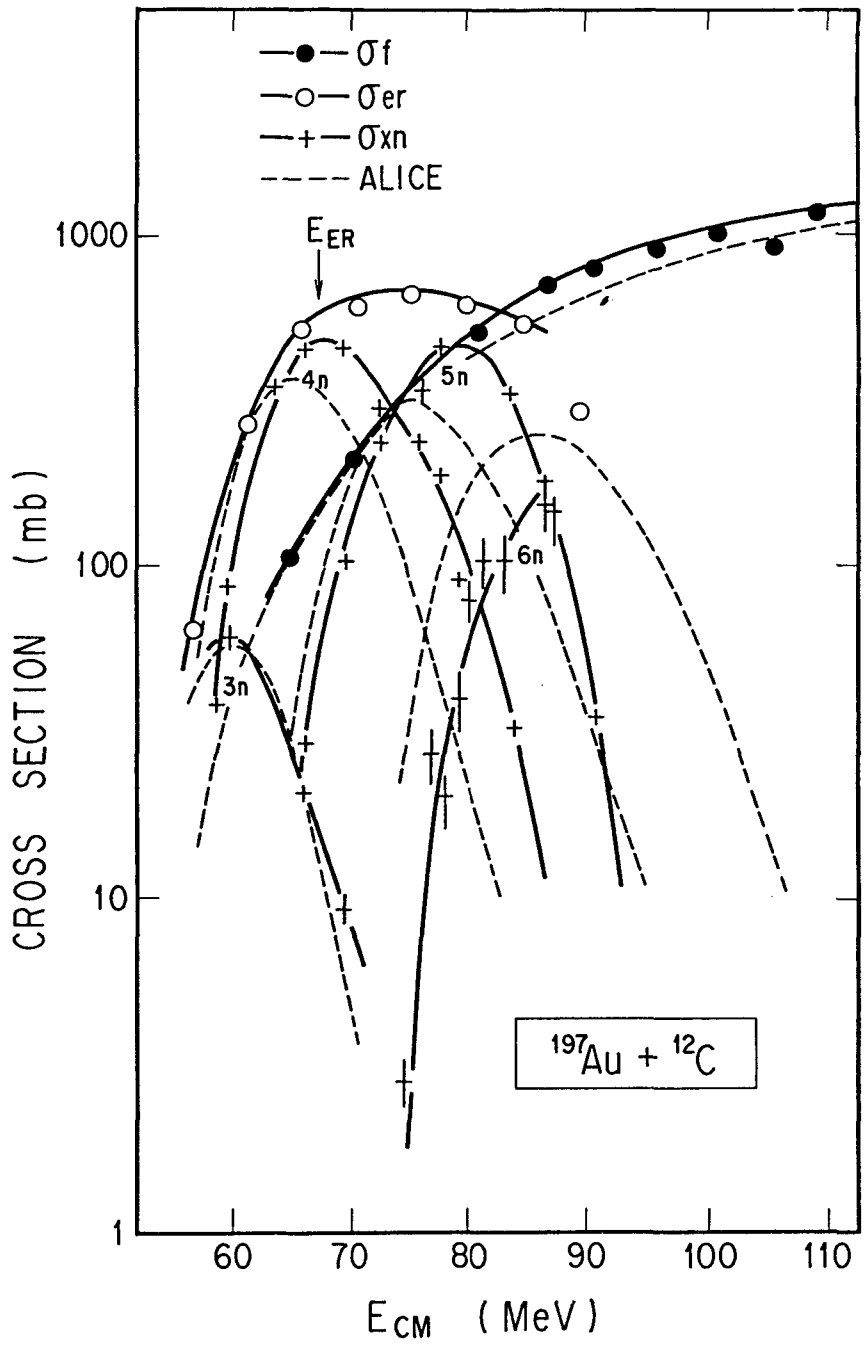

Fig.3.12. Excitation functions of xn reactions (σ_{xn}), formation of total evaporation residues (σ_{er}) and fission (σ_f) [24] for the ^{12}C-induced reaction. See 3.4.4 for the symbol E_{ER} marked with arrow. Solid lines are drawn through the experimental values. Dashed lines represent the excitation function calculated by the ALICE code with the parameters a_f/a_ν = 1.06 and P_{LD} = 18.

3.4. DISCUSSION

3.4.1. Comparison of Fusion Cross Sections and Model Calculations for Fusion

The total cross sections of evaporation residues σ_{er} were deduced for the ^{16}O- and ^{12}C-induced reactions in 3.3.4. Then fusion cross section σ_{fu} was obtained from the sum of σ_{er} and the fission cross section σ_f. I referred to the fission cross sections of [23] and [24] for the ^{16}O- and ^{12}C-induced reactions, respectively. Obtained values of σ_{fu} are plotted versus $1/E_{cm}$ with solid lines in Figs. 3.13 and 3.14.

As well as the reaction cross section (see Eq.(2.7)), the fusion cross section is expressed as

$$\sigma_{fu} = \pi \lambda\!\!\!^{-2} \sum_{\ell=0}^{\infty} (2\ell+1) T^{fu}_{\ell} \qquad (3.2)$$

with the transmission coefficient T^{fu}_{ℓ} of the ℓ-th partial wave for fusion at the center-of-mass energy E_{cm}. In the sharp cut-off approximation, T^{fu}_{ℓ} is assumed to be unity for $\ell \leq \ell_{crit}$ and T^{fu}_{ℓ} is assumed to be zero for $\ell > \ell_{crit}$. Here, ℓ_{crit} is given by the maximum orbital angular momentum ℓ_{max} in the entrance channel as far as ℓ_{max} does not exceed the critical angular momentum for fusion, ℓ_{fu}. This is a plausible approximation in the heavy-

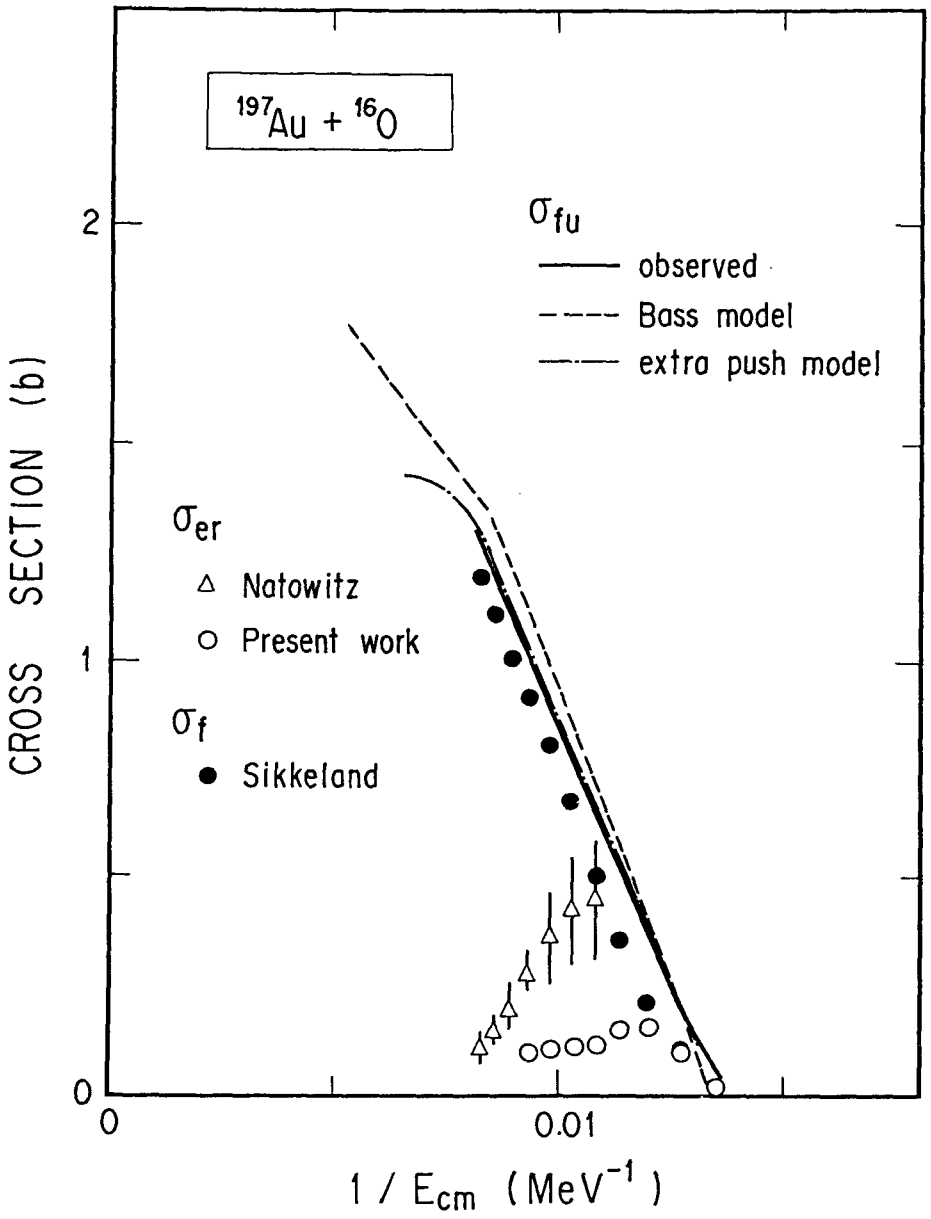

Fig.3.13. Fusion cross section σ_{fu} from the sum of σ_{er} and fission cross section σ_f for the ^{16}O-induced reactions versus 1/E. The fusion cross sections calculated with models are drawn with dashed lines (Bass model) and dot-dashed lines (extra-push model).

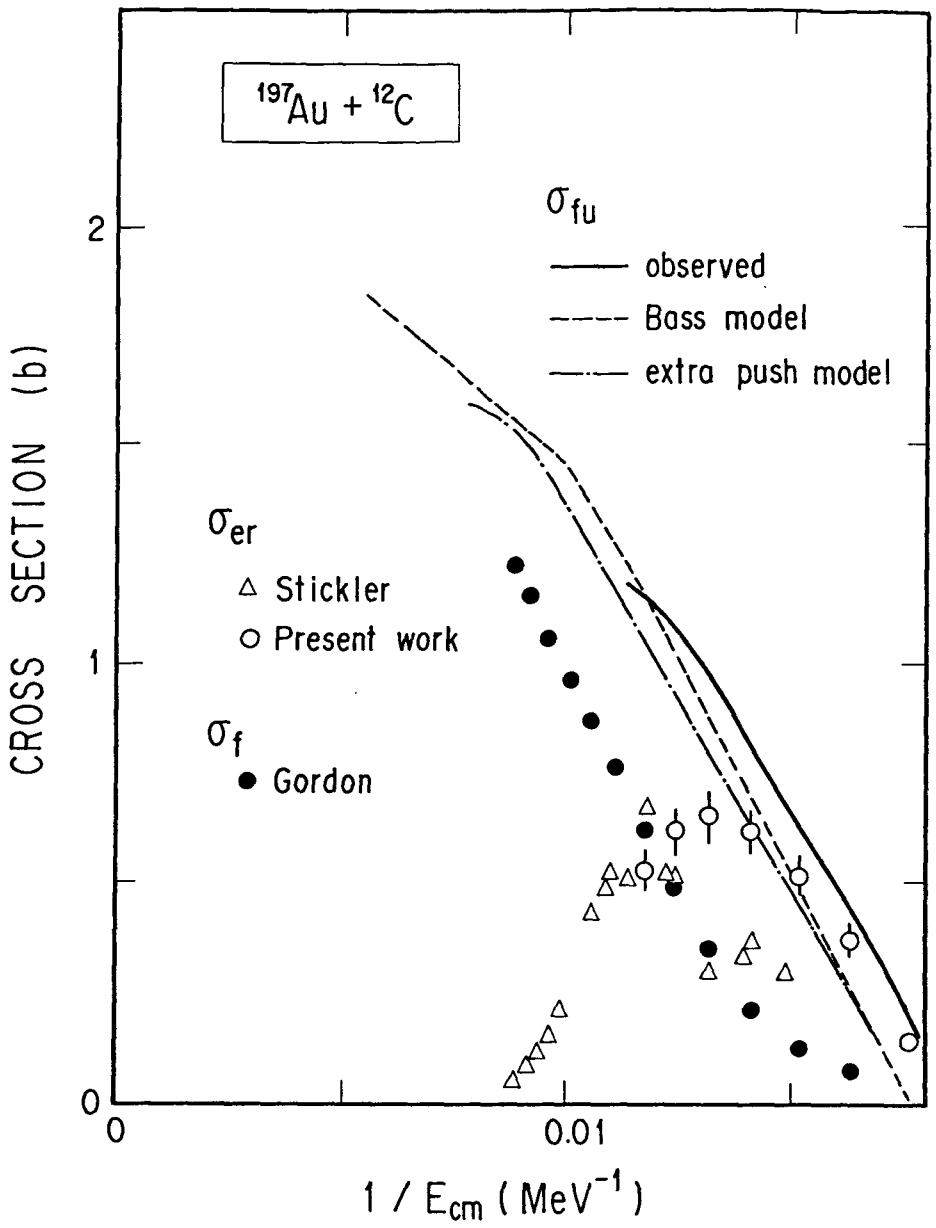

Fig.3.14. The same as Fig.3.13 but for the ^{12}C-induced reactions

ion induced reaction in which a projectile moves near the classical trajectory. Then, σ_{fu} is rewritten as

$$\sigma_{fu} = \pi \lambda\!\!\!^{-2} \sum_{\ell=0}^{\ell_{crit}} (2\ell+1)$$

$$= \pi \hbar^2/(2\mu)(\ell_{crit}+1)^2 \ /E_{cm}. \qquad (3.3)$$

According to Eq.(3.3), σ_{fu} depends on ℓ_{crit} besides the explicit energy dependence of $1/E_{cm}$ in the low energy region where $\ell_{max} < \ell_{fu}$, but should lie on a straight line passing through the origin for sufficiently high energies when plotted versus $1/E_{cm}$.

In order to investigate the reaction mechanism, I applied two models to both of the reaction systems studied; one is Bass model [30] and the other is the extra-push model [31]. Bass model is a simple model for fusion of heavy nuclei. It is based on a one-dimensional potential, and energy and angular momentum conservations are taken into account in the model. Its agreement with the observed data has been attained in the energy region not too high above the Coulomb barrier and for reaction systems not too heavy [2]. Whereas Swiatecki proposed a extra-push model based on a multidimensional dynamic calculation with one-body dissipation and the effects of neck formation between the interacting nuclei. The model has been successful in reproducing the data for very heavy systems for which the one-dimensional potential model fails to give quantitative explanation [2]. Fu-

sion cross sections calculated with the two models are drawn with dashed lines (Bass model) and dot-dashed lines (extra-push model) in Figs.3.13 and 3.14.

For the ^{16}O-induced reaction, calculation with Bass model reproduces the observed data fairly well, while agreement of data and calculation is even much better with the extra-push model. For the ^{12}C-induced reaction, both of the models attain equally fairly good agreement with observed data though they give some deviations from the observation.

In conclusion, therefore, I could not find the superior model of the above two as far as the present study concerns. The extra-push model has been shown to reproduce well the fusion cross sections in the heavy element region [31], while Bass model is found to work satisfactorily for light nuclear systems. The reaction systems in the present study happen to lie in the boundary zone. This is why both of the models worked equally well.

3.4.2. Comparison of the Observed Excitation Functions with Statistical Model Calculation

In this subsection competition of particle evaporation and fission shall be discussed. Probabilities of fission and evaporation of particle x ($x = n, p, \alpha$) are expressed as

$$p_f = \Gamma_f/(\Gamma_f+\sum_x \Gamma_x) \qquad (3.4)$$

and

$$p_x = \Gamma_x/(\Gamma_f+\sum_x \Gamma_x), \tag{3.5}$$

respectively, where Γ_f and Γ_x are the level widths of fission and particle evaporation, respectively [1]. The widths are expressed as

$$\Gamma_f = \pi\hbar^2 \int_0^{E-B_f(J)} \rho^*(E-B_f(J)-K)dK \tag{3.6}$$

and

$$\Gamma_x \ (x= n,p,\alpha) = 2g_x\mu_x \int_0^{E-B_x(J)} \sigma_x(\varepsilon)\rho(E-B_x(J)-\varepsilon)d\varepsilon . \tag{3.7}$$

E is the excitation energy of the compound nucleus, B_f and B_x are fission barrier and effective binding energy of the x particle , respectively, and g_x, μ_x, and σ_x are the intrinsic degeneracy and the reduced mass of x particle, and the inverse cross section of the residual nucleus and x particle, respectively. Furthermore ε is the kinetic energy of the emitted particle while K is the energy in the fission degrees of freedom. ρ^* (E) and ρ (E) are the nuclear level densities at the saddle point and at the equilibrium deformation after particle emission, respectively, and expressed by the Fermi gas model as

$$\rho(E) = E^{-2}\exp[2(aE)^{1/2}] \tag{3.8}$$

with the level density parameter a. Two different level density parameters, a_f and a_ν, are defined for the saddle point and for the equilibrium deformation after particle emission [1]. In a simple approximation, a is expressed as

$$a = A/P_{LD} \tag{3.9}$$

where A is the mass number of the nucleus and P_{LD} is a parameter taking a value between 8 and 12 in most cases [39].

Parameter fitting procedure was carried out with two adjustable parameters, the ratio a_f/a_ν and P_{LD}, using the ALICE code [40,41]. In the fitting RFRM fission barriers are used in the calculation without any scaling. The a_f/a_ν value is related to the relative strength of fission againt particle evaporation. Increase in a_f/a_ν results in the raise of the fission excitation function. P_{LD} is associated with the starting energy of the excitation function of each evaporation residue. The larger the P_{LD} value is, the higher the threshold energy for particle evaporation. The best fit condition was found to be a_f/a_ν = 1.03 and P_{LD} = 18 for the ^{16}O-induced reaction and a_f/a_ν = 1.06 and P_{LD} = 18 for the ^{12}C-induced reaction. Calculated excitation functions of xn reactions and fission are depicted in Figs.3.11 and 3.12. Statistical calculation with RFRM fission barriers reproduced fairly well the data in the present systems. The

parameter values of a_f/a_ν fitted to the data are close to those predicted by Reisdorf [39], namely, 1.05 and 1.06 for the ^{16}O- and ^{12}C-induced reactions, respectively. The resulting P_{LD} is, however, considerably larger than usual values. Hofstetter and Stickler have reported that the excitation functions in the $^{197}Au+^{12}C$ reaction were reproduced well with $P_{LD}=20$ in a similar statistical calculation [29]. A large value of P_{LD} means only a small number of levels are available in the nuclear system. Though calculation with a more reasonable value of $P_{LD}=12$ can reproduce the general feature of excitation functions of evaporation residues, threshold energies and peak positions of the functions were not reproduced well with the value. There are certainly a few kinds of over-simplification in the model calculation, such as neglect of angular momenta taken away by the emitted particles or disregard of the competition of γ-ray transitions. Yet, the presently deduced large value of $P_{LD}=18$ or 20 is hardly understandable for such mid-shell nuclei. This problem must therefore be left for future studies as an open question.

3.4.3. Fission Barrier Dependent on the Angular Momentum

In the statistical analysis of the competition of fission and particle evaporation, the fission barrier dependent on the angular momentum, $B_f(J)$, is another important quantity. So far I have used a theoretically predicted fission barrier, the RFRM barrier [19], which is proved to be consistent with experiments in many reaction systems. However, the verfication of the

predicted barrier is indirect and performed by comparing observed and calculated excitation functions accompanied by multi-parameter fitting. In order to calculate partial cross sections we need to know the fission barrier height for a given value of the angular momentum J. It has been considered that one can not determine the fission barrier for any specified J. It is qualitatively accepted that the fission barrier decreases as J increases and finally disappears at a certain critical value of J. However, there has been no way to know experimentally the J-dependence of the barrier. I had to accept the guidance of the theory on this J-dependence.

There is still another ambiguity in the whole problem; namely, the specification of the fissioning nucleus at which the series of particle emission terminate and fission takes place instead. Though RFRM or RLDM does predict the fission barrier of a given value of J, it does not tell us what is the fissioning nucleus for a given reaction system. So one has to treat the problem comprehensively by means of the statistical model calculation with predicted fission barries and demonstrates satisfactory reproduction of observed fission excitation functions of as many nuclei as possible to verify the theory. It follows that the theory is not directly compared with experiments as far as the fission barrier concerns. On the contrary, I devised a method to deduce experimentally the fission barrier at a specified J-window. It is discussed in detail in 3.4.4.

3.4.4. Deduction of Fission Barrier at a Specified J-Window

Fusion cross section σ_{fu} is expressed as

$$\sigma_{fu}(E) = \pi \lambda\!\!\!^{-2} \sum_{\ell=0}^{\infty} (2\ell+1) T^{fu}_{\ell}(E) = \sigma_{er}(E) + \sigma_{f}(E) \qquad (3.10)$$

since the fused system is considered to decay via either of two competing processes, particle evaporation and fission. Here, charged-particle emission is neglected in the evaporation process [42] and, for simplicity, both the target nucleus and the projectile are assumed to have zero spins. Then, the formation cross section for evaporation residues is given by

$$\sigma_{er}(E) = \pi \lambda\!\!\!^{-2} \sum_{J=0}^{\infty} (2J+1) T^{fu}_{J}(E) \prod_{i} \{1 - p_{f,i}(J; E_{x,i})\}, \qquad (3.11)$$

where $p_{f,i}$ is the probability that the compound nucleus with angular momentum J once formed ends up in fission after (i-1) neutrons are evaporated. $p_{f,i}$ is written as

$$p_{f,i} = \Gamma^{i}_{f}(E_{x,i},J) / \{\Gamma^{i}_{n}(E_{x,i},J) + \Gamma^{i}_{f}(E_{x,i},J)\}, \qquad (3.12)$$

where Γ^{i}_{n} and Γ^{i}_{f} are the partial level widths for neutron emission and fission, respectively, for the residual nucleus after (i-1) neutrons are emitted. $E_{x,i}$ is the excitation energy left in the i-th residual nuclei,

namely,

$$E_{x,i} = E + Q_i - \sum_{k=1}^{i-1} \varepsilon_k \qquad (3.13)$$

with the reaction Q-value Q_i and average kinetic energy ε_k of the emitted neutrons. I have further disregarded the variation of the angular momentum due to neutron emission since it would not mislead the consequences.

For partial level widths, let me use the well established expression:

$$\Gamma^J{}_f(E_x,J)/\Gamma^J{}_n(E_x,J) = C \cdot \exp\{2[a_f(E_x'-B_f(J))]^{1/2} - 2[a_n(E_x'-B_n)]^{1/2}\}, \qquad (3.14)$$

where $E_x' = E_x - E^0{}_R$, B_n is the neutron separation energy, and a_f and a_n are the level density parameters in the fission and neutron channels, respectively. $E^0{}_R$ is the rotational energy at the equilibrium deformation [3]. The pre-exponential factor C is given by

$$C = K_0\{2[a_f(E_x'-B_f(J))]^{1/2}-1\}/[4\alpha A^{2/3}(E_x'-B_n)] \qquad (3.15)$$

with $\alpha = a_f/a_n$ and a constant K_0 being chosen to be 9.8MeV [23]. The energy B_n was calculated with mass data of [43]. $B_f(J)$ is the angular momentum-dependent fission barrier.

For the pre-actinide nuclides, fission barrier at zero-angular momen-

tum is larger than B_n, so that fission cross section is negligibly small in the low energy region. As the angular momentum increases the fission barrier decreases, eventually becomes comparable to B_n, and finally vanishes at a certain value of the angular momentum. One can see from such trend of $B_f(J)$ and from Eqs.(3.12) and (3.14) that $p_f(J)$ essentially remains zero while J is small, very steeply rises in the vicinity of a certain value of J, J_{ER}, and reaches a plateau (=1) for higher J values. J_{ER} is defined as the critical angular momentum at which the Γ_f/Γ_n value of Eq.(3.14) is unity or $p_f(J_{ER}) = 0.5$. (p_f depends weakly on the energy and therefore the energy is suppressed in the notation.)

To find out such J_{ER}'s, the experimental values $\sigma_{er}(E)$ and $\sigma_f(E)$ for the ^{16}O- and ^{12}C-induced reactions were analyzed in the following procedure. Heavy-ion fusion reaction is known to be treated classically, that is, $T_J=1$ for $J \leqq J_{crit}$ and 0 for $J > J_{crit}$ in terms of the critical angular momentum J_{crit} for fusion, which is a function of energy. One can rewrite Eq.(3.11) as

$$\sigma_{er}(E) = \pi \lambda\!\!\!^{-2} \sum_{J=0}^{J_{crit}} (2J+1) \prod_i \{1 - p_{f,i}(J)\}, \tag{3.16}$$

For energies so high that J_{crit} is greater than J_{ER}, Eq.(3.16) is further rewritten as

$$\sigma_{er}(E) = \pi \lambda\!\!\!^{-2} \sum_{J=0}^{J_{ER,i}} (2J+1)$$

$$= \pi \hbar^2/(2\mu E)(J_{ER,i} + 1)^2 \qquad (3.17)$$

since the summation up to J_{crit} in Eq.(3.16) is replaced by the summation up to J_{ER} for the sharp cut-off distribution of p_f as depicted in Fig.3.15. Here, one should note that among the sequential multiple chance fissions only the i-th fission for which the critical value $J_{ER,i}$ is the smallest of all becomes effective in Eq.(3.17). The empirically determined critical value J_{ER} corresponds to this smallest J_{ER}. I will mention later about the multiplicity i in more detail.

As Figs.3.16 and 3.17 show, σ_{er} varies proportionally to 1/E in the energy ranges 85 - 110MeV and 70 - 85MeV, respectively. In the energy region, $\sigma_{er}(E)$ can be expressed as Eq.(3.17). Then critical energy E_{ER} was extracted by extrapolation of the linear part to the point where the line crosses the fusion excitation function (cf. Figs.3.16 and 3.17). E_{ER} is interpreted as just the energy where fission starts at the maximum angular momentum brought in the fused system, when the smooth variation of p_f from 0 to 1 is substituted for an equivalent sharp cut-off. The exact value p_f should be 0.5 at $J = J_{ER}$. J_{ER} is then calculated with E_{ER} as

$$J_{ER} = (2\mu E_{ER} \cdot \sigma_{ER}/\pi \hbar^2)^{1/2} - 1, \qquad (3.18)$$

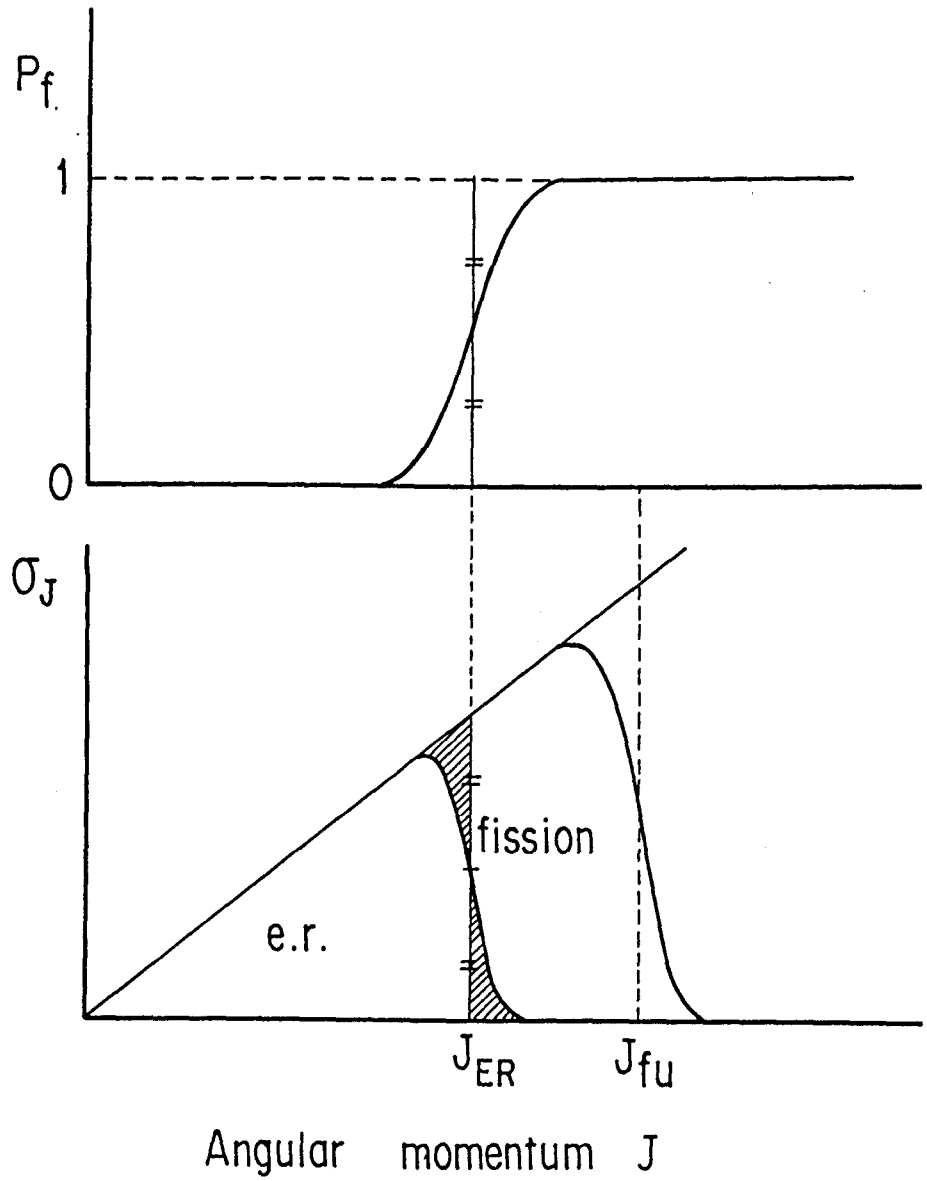

Fig.3.15. Schematic illustration of the sharp cut-off approximation. See text for the symbols.

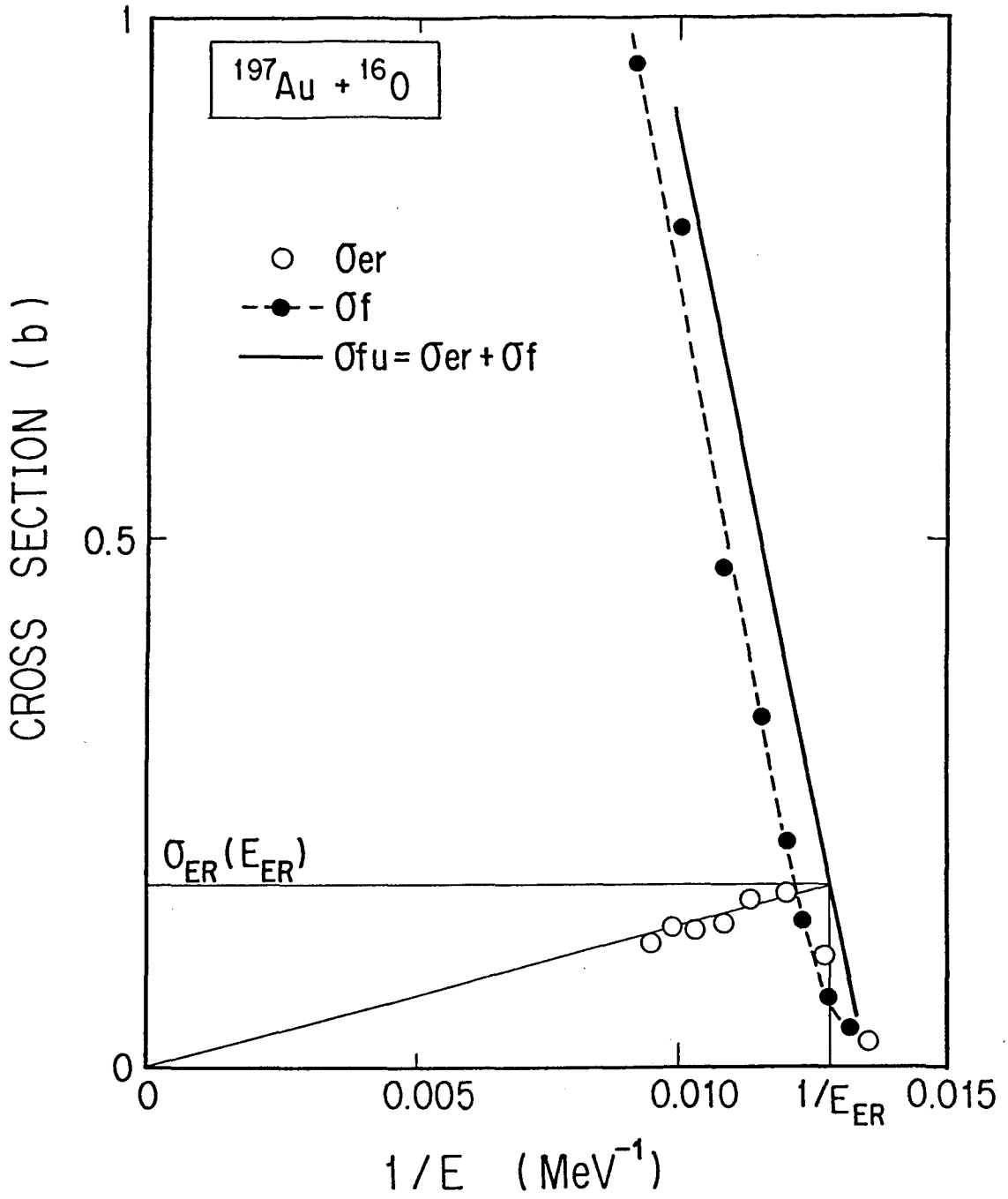

Fig.3.16. Excitation functions of fission, fusion, and formation of the evaporation residues for the ^{16}O-induced reactions versus 1/E. See text for the symbols.

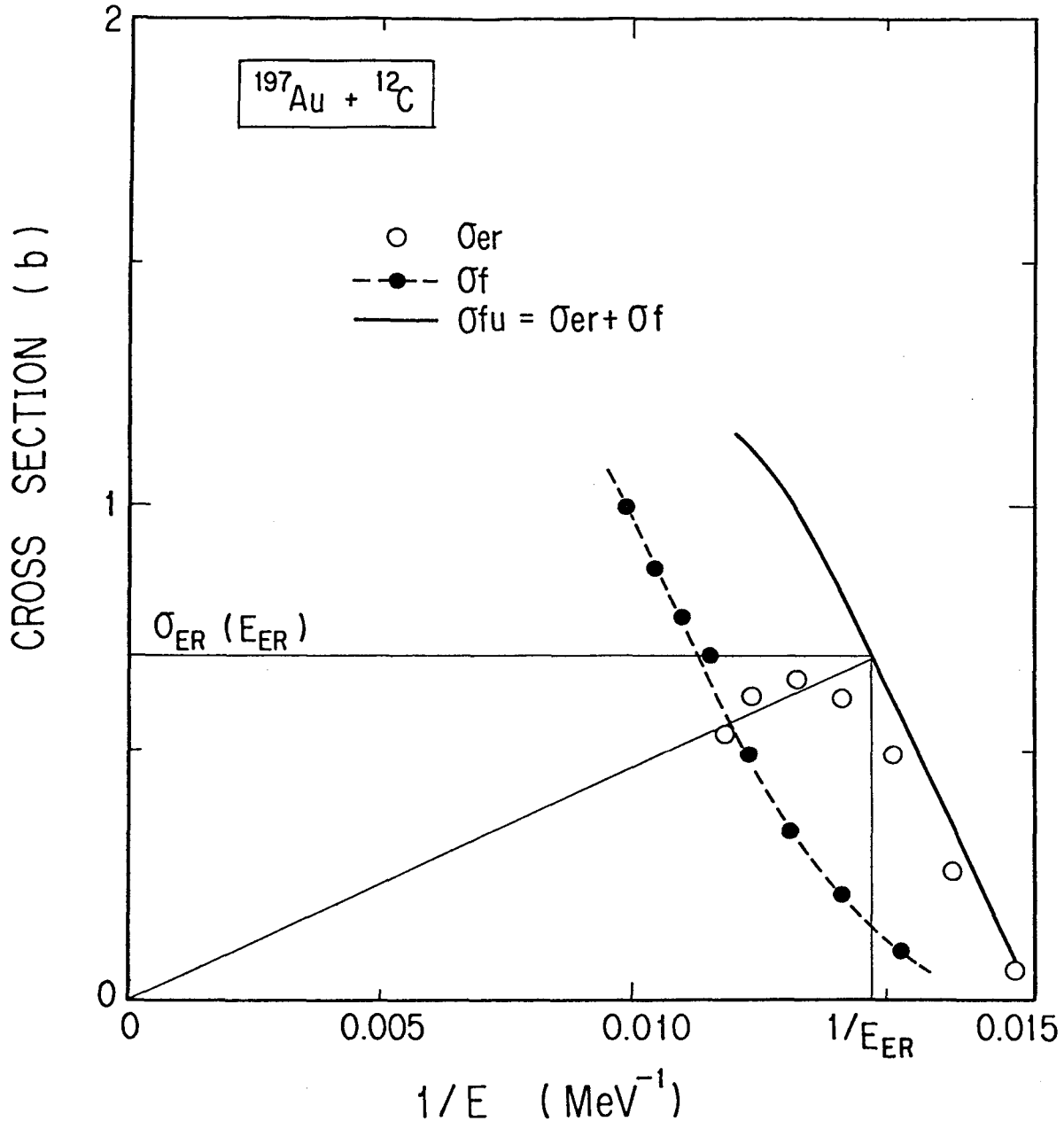

Fig.3.17. Same as Fig.3.16 but for the ^{12}C-induced reactions.

where

$$\sigma_{ER} = \sigma_{fu}(E_{ER}) \tag{3.19}$$

In Table 3.3, these values experimentally obtained for the ^{16}O- and ^{12}C-induced reactions are presented. Setting Eq.(3.14) = 1 and $E'_{x,i} = E_{ER} + Q_i - E^0_R$, one obtains the equation

$$B_f(J_{ER,i}) = (1-\alpha^{-1})E'_{x,i} + B_{n,i}/\alpha - (\ln C)^2/(4a_f) + \ln C/a_f[a_n(E_{x,i}'-B_{n,i})]^{1/2}. \tag{3.20}$$

When the number i is given, one can calculate fission barrier height of fissioning nucleus by solving Eq.(3.20) and assign it to the experimentally obtained angular momentum J_{ER}.

3.4.5. Neutron Multiplicity of Fission Process

The excitation functions of xn reactions, formation of total evaporation residues and fission are shown for the two reaction systems in Figs.3.11 and 3.12, respectively, where E_{ER}'s are marked with arrows. As shown in the figures, 4-neutron evaporation occurs mainly at E_{ER} in both systems and charged particle emission can be neglected there. Accordingly, fission may begin to compete with 0, 1, 2, or 3-neutron evaporation in a

Table 3.3. Specified values of E_{ER}, σ_{ER}, J_{ER} obtained from the analysis described in 3.4.4.

	$^{16}O + ^{197}Au$	$^{12}C + ^{197}Au$
E_{ER} (MeV)	78.0± 0.5	67.5± 0.5
σ_{ER} (mb)	170± 5	690± 10
$J_{ER,i}$ ($\hbar$)	16± 1	27± 1

fused system with the angular momentum of J_{ER}. Therefore, the number i in Eq.(3.20) is between 1 and 4.

Equation (3.20) contains two adjustable parameters a_n and $\alpha = a_f/a_n$. Use was made of a_n = A/18 which was obtained in fitting to excitation functions of evaporation residues described in 3.4.2. However, the parameter a_f/a_n obtained in the fitting is not perfectly dependable since it is associated with the RFRM barriers used in the calculation. Consequently, the value of a_f/a_n was determined according to the following consideration. Different combinations of target and projectile leading to the same compound systems have the same J-window and consequently the same J_{ER} and the same value of B_f by Eq.(3.17). As a result of performing such a procedure with three groups of the combinations, ^{210}Po, ^{206}Po, and ^{200}Pb [11,20,22,44] in the vicinity of the present systems, the a_f/a_n value was determined to be 1.10 when a_n=A/18 was chosen.

Next the effective multiplicity of fission was obtained according to the following procedure. $B_f(J)$ decreases monotonously as J increases, and so does $B_f(J)/B_f(0)$. The rate of barrier reduction $B_f(J)/B_f(0)$ should not significantly differ among the species involved in the series of particle evaporation. Therefore the nucleus showing the smallest reduction rate should be associated with the smallest J_{ER}. As $B_f(0)$, I rather used a liquid drop barrier [45] $B^{LD}{}_f(0)$ expressed as

$$B^{LD}{}_f(0) = 0.38(0.75-x)E^0{}_s \quad \text{for } x \leqq 0.675$$
$$= 0.83(1-x)^3E^0{}_s \quad \text{for } x > 0.675, \qquad (3.21)$$

where $x = (Z^2/A)/48.0$ was used as the fissility parameter and $E^0s = 17.8A^{2/3}$ MeV as the surface energy of the spherical nucleus [23] with mass number A. This is because it is expected to be a suitable normalization factor which gives the right order in the magnitude of the reduction rate among the neighboring isotopes, even if its absolute magnitude may not be correct. The situation in the ^{16}O-induced reaction is schematically illustrated in Fig.3.18, where calculated $B_{f,i}(J_{ER,i})/B_{f,i}(0)$ are shown for Fr isotopes with mass numbers from 210 to 213 in relation with each $J_{ER,i}$. Here a curve of solid line schematically represents the J-dependence of $B_f(J)/B_f(0)$ common to all of $^{210-213}Fr$. Therefore the order among the magnitudes of $B_f(J)/B_f(0)$ for different fissioning nuclei can be converted to that of the specific angular momenta for the compound nucleus ^{213}Fr. In this reaction system the third chance fission, fission of ^{211}Fr, was found to give the smallest critical J-value and consequently the previously deduced J-window J_{ER} was concluded to belong to ^{211}Fr. A similar situation was obtained also in the case of ^{12}C-induced reaction, that is, the third chance fission has been predominant when the fission channel opens. (see Table 3.4.)

The final results are listed in Table 3.5, in which the numbers of prefission neutrons are given as well as the deduced fission barriers. In Table 3.5 are also given the prefission neutron numbers at E_{ER} computed by the systematics given by Hinde [46] for comparison. The fission barriers are compared in Fig.3.19 with the RFRM fission barriers [19].

The present analysis extracts the effective fissioning nucleus at a particular energy and a specified J-value. It follows that we can deduce the effective numbers of prefission neutrons which are found reasonable

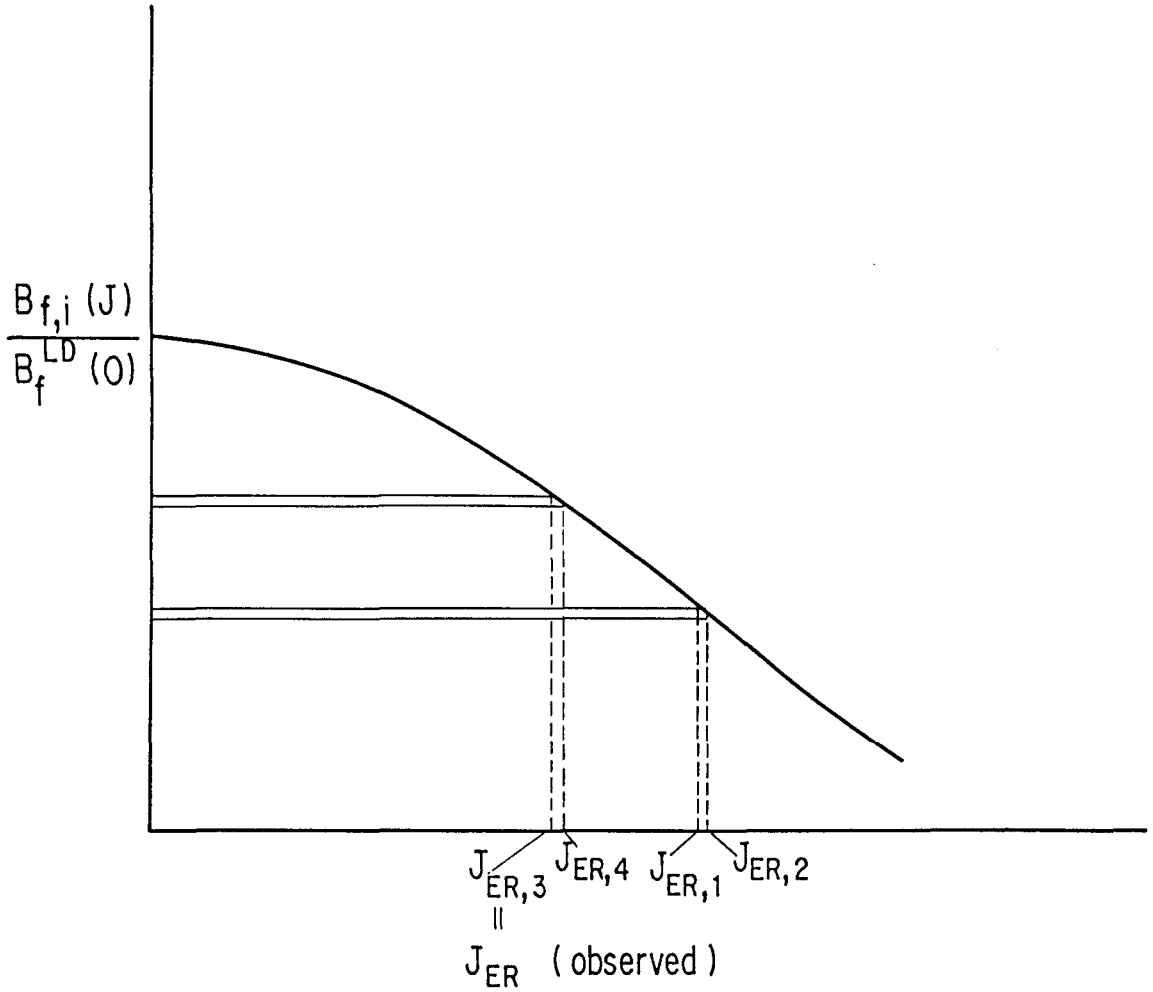

Fig.3.18. Calculated ratios $B_{f,i}(J_{ER,i})/B_{f,i}(0)$ for Fr isotopes with mass numbers from 210 to 213 in relation with each $J_{ER,i}$.

Table 3.4. Reduced fission barriers for possible fissioning nuclides at the critical angular momentum

i-th chance fission	Number of emitted neutron	$^{16}O + ^{197}Au$ $B_{f,i}/B^{LD}_{f,i}(0)$	$^{12}C + ^{197}Au$ $B_{f,i}/B^{LD}_{f,i}(0)$
1	0	0.78	0.66
2	1	0.76	0.60
3	2	0.97	0.78
4	3	0.91	0.71

Table 3.5. Pre-fission neutron numbers ν_{pre} and fission barriers

Reaction	ν_{pre} Obtained	[46]	Fissioning Nuclide	J(ħ)	Fission Barrier obtained (MeV)
$^{16}O + ^{197}Au$	2	1.5	^{211}Fr	16± 1	8.0
$^{12}C + ^{197}Au$	2	1.8	^{207}At	27± 1	7.8

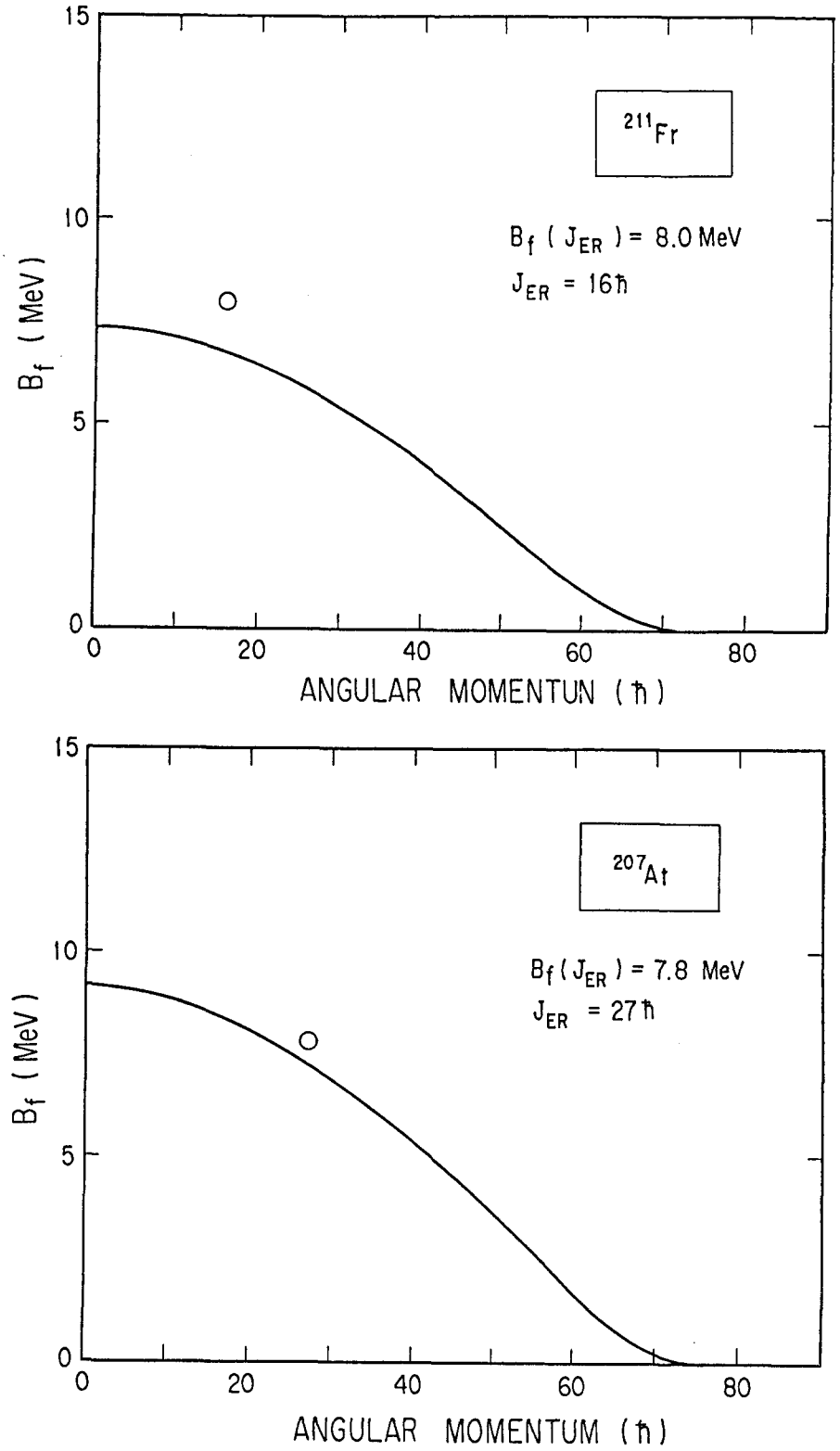

Fig.3.19. Deduced fission barriers at specified J-windows for ^{16}O- and ^{12}C-induced reactions. Solid lines represent the RFRM fission barriers.

considering Hinde's systematics despite of the facts that the former neglects minor contributions of fission with other multiplicities and the latter has reservation in subtraction of post-scission neutrons. Fission barriers presently obtained turned out to be significantly high for ^{211}Fr and ^{207}At as compared with the RFRM barriers. The discrepancies might indicate deviations of the nuclear property from the averaged liquid-drop nature. We, however, need a systematic study of the fission barrier before we can deduce a clear conclusion on the present problem.

3.5. Conclusion

Total cross sections of evaporation residues were measured for the ^{16}O- and ^{12}C-induced reactions on ^{197}Au. Fusion cross sections, the sum of σ_{er} and σ_f, are reproduced well with either of Bass model or the extra-push model. The competition process of fission and particle evaporation is satisfactorily explained by statistical model calculation with the RFRM fission barriers.

I described a simple method based on the statistical model but practically with no fitting processes. It enabled us to define a specific J-window for pre-actinide fissioning systems, to deduce fission barrier $B_f(J)$ at this J-value and to determine the effective fissioning nucleus together. This analysis is applicable to the reaction system in which probability of fission is comparable with that of evaporation residue formation at the excitation energy, where non-complete-fusion processes can be easily discriminated.

REFERENCES TO SECTION 3

1. Friedlander, G., Kennedy, J. W., Macias, E. S., Miller, J. M.: Nuclear and Radiochemistry, 3rd ed., pp. 132-147. New York, Chichester, Brisbane, Toronto: Wiley 1981
2. Birkelund, J. R., Huizenga, J. R.: Ann. Rev. Nucl. Part. Sci. 33, 265 (1983)
3. Cohen, S., Plasil, F., Swiatecki, W. J.: Ann. Phys. (N.Y.) 82, 557 (1974)
4. Le Beyec, Y., Hahn, R. L., Toth, K. S., Eppley, R.: Phys. Rev. C14, 1038 (1976)
5. Beckerman, M., Blann, M.: Phys. Rev. Lett. 38, 272 (1977)
6. Plasil, F., Ferguson, L., Britt, H. C., Erkkila, B. H., Goldstone, P. D., Stokes, R. H., Gutbrod, H. H.: Phys. Rev. C18, 2603 (1978)
7. Beckerman, M., Blann, M.: Phys. Rev. C17, 1615 (1978)
8. Plasil, F., Ferguson, R. L., Hahn, R. L., Obenshain, F. E., Pleasonton, F., Young, G. R.: Phys. Rev. Lett. 45, 333 (1980)
9. Sikora, B., Scobel, W., Beckerman, M., Bisplinghoff, J., Blann, M.: Phys. Rev. C25, 1446 (1982)
10. Guillaume, G., Coffin, J. P., Rami, F., Engelstein, P., Heusch, B., Wagner, P., Fintz, P., Barrette, J., Wegner, H. E.: Phys. Rev. C26, 2458 (1982)
11. Leigh, J. R., Hinde, D. J., Newton, J. O., Galster, W., Sie, S. H.: Phys. Rev. Lett. 48, 527 (1982)

    Hinde, D. J., Leigh, J. R., Newton, J. O., Galster, W., Sie, S. H.:

Nucl. Phys. A385, 109 (1982)

12. Hinde, D. J., Newton, J. O., Leigh, J. R., Charity, R. J.: Nucl. Phys. A398, 308 (1983)
13. Rohe, R., DiRienzo, A., Enge, H., Salomaa, M. K., Smith, A., Schier, W., Tsoupes, N., Wegner, H. E.: Phys. Rev. C29, 1362 (1984)
14. Plasil, F., Awes, T. C., Cheynis, B., Drain, D., Ferguson, R. L., Obenshain, F. E., Sierk, A. J., Steadman, S. G., Young, G. R.: Phys. Rev. C29, 1145 (1984)
15. Delagrange, H., Benachou, A., Hubert, F., Llabador, Y., Heusch, B., Coffin, J. P., Engelstein, P., Fintz, P., Guillaume, G.: Nucl. Phys. A429, 173 (1984)
16. Reisdorf, W., Hessberger, F. P., Hildebrand, K. D., Hofmann, S., Münzenberg, G., Schmidt, K.-H., Schneider, W. F. W., Sümerer, K., Wirth, G., Kratz, J. V., Schlitt, K., Sahm, C.-C.: Nucl. Phys. A444, 154, (1985)
17. Britt, H. C.: Phys. Rev. Lett. 39, 1458 (1977)
18. Mustafa, M. G., Baisden, P. A., Chandra, H.: Phys. Rev. C25, 2524 (1982)
19. Sierk, A. J.: Phys. Rev. C33, 2039 (1986)
20. Van der Plicht, J., Britt, H. C., Fowler, M. M., Fraenkel, Z., Gavron, A., Wilhelmy, J. B., Plasil, F., Awes, T. C., Young, G. R.: Phys. Rev. C28, 2022 (1983)
21. Beckerman, M., Wiggins, J., Aljuwain, H., Salomaa, M. K.: Phys. Rev. C29, 1938 (1984)
22. Charity, R. J., Leigh, J. R., Bokhorst, J. J. M., Chatterjee, A.,

Foote, G. S., Hinde, D. J., Newton, J. O., Ogaza, S., Ward, D.: Nucl. Phys. A457, 441 (1986)

23. Sikkeland, T.: Phys. Rev. 135, B669 (1964)
24. Gordon, G. E., Larsh, A. E., Sikkeland, T., Seaborg, G. T.: Phys. Rev. 120, 1341 (1960)
25. Natowitz, J. B.: Phys. Rev. C1, 623 (1970)
26. Hinde, D. J., Charity, R. J., Foote, G. S., Leigh, J. R., Newton, J. O., Ogaza, S., Chattejee, A.: Nucl. Phys. A452, 550 (1986)
27. Thomas, T. D., Gordon, G. F., Latimer, R. M., Seaborg, G. T.,: Phys. Rev. 126, 1805 (1962)
28. Bimbot, R., Lefort, M., Simon, A.: J. Phys. (Paris) 29, 563 (1968)
29. Stickler, J. D., Hofstetter, K. J.: Phys. Rev. C9, 1064 (1974)
    Hofstetter, K. J., Stickler, J. D.: Phys. Rev. C9, 1072 (1974)
30. Bass, R.: Nucl. Phys. A231, 45 (1974)
31. Swiatecki, W. J.: Nucl. Phys. A376, 275 (1982)
32. Lederer, C. M., Shirley, V. S. (ed.): Table of Isotopes, 7th ed. New York, Chichester, Brisbane, Toronto: Wiley 1978
33. Hornshøj, P., Hansen, P. G., Jonson, B.: Nucl. Phys. A230, 380 (1974)
34. Friedlander, G., Kennedy, J. W., Macias, E. S., Miller, J. M.: Nuclear and Radiochemistry, 3rd ed., pp. 321-323. New York, Chichester, Brisbane, Toronto: Wiley 1981
35. Friedlander, G., Kennedy, J. W., Macias, E. S., Miller, J. M.: Nuclear and Radiochemistry, 3rd ed., pp. 302. New York, Chichester, Brisbane, Toronto: Wiley 1981
36. Ewart, A., Valentine, C., Blann, M.: Nucl. Phys. 69, 625 (1965)

37. Hata, K.: to be published in INDC report

38. Bimbot, R., Gardes, D., Rivet, F.: Nucl. Phys. A189, 193 (1972)

39. Reisdorf, W.: Z. Phys. A300, 227 (1981)

40. Plasil, F., Blann, M.: Phys. Rev. C11, 508 (1975)

41. Blann, M.: COO-3494-29 (1976)

42. Britt, H. C., Quinton, A. R.: Phys. Rev. 124, 877 (1961)

43. Wapstra, A. H., Audi, G.: Nucl. Phys. A432, 1 (1985)

44. Forster, J. S., Mitchell, I. V., Andersen, J. U., Jensen, A. S., Laegsgaard, E., Gibson, W. M., Reichelt, K.: Nucl. Phys. A464, 497 (1987)

45. Cohen, S., Swiatecki, W. J.: Ann. Phys. (N.Y.) 22, 406 (1963)

46. Hinde, D. J.: private communication

APPENDICES

A. DIFFUSION MODEL

One dimensional master equation can be described by means of Fokker-Planck equation as follows [1];

$$\partial P(x,t)/\partial t = -v\,\partial P/\partial x + D\,\partial^2 P/\partial x^2, \qquad (A.1)$$

where $P(x,t)$ is the probability for the system possessing the value x for a given characteristic valuable at a moment of time t. In this case x may be the atomic number or the mass number of one of the DIT products, v and D are the drift velocity and the diffusion coefficient, respectively. If the coefficients v and D remain constant in the course of interaction and the initial distribution over x has the form of a δ function, the Fokker-Planck equation has the following solution [1]:

$$P(x,t) = (4\pi Dt)^{-1/2}\exp[-(x-vt)^2/(4Dt)]. \qquad (A.2)$$

If one specifies x and t as the atomic number of projectile-like products Z_{PLP} and the ℓ-dependent interaction time $\tau_{int}(\ell)$, respectively, equation (2.29) is obtained as follows [2,3];

$$P\{Z_{PLP},(\tau_{int}(\ell))_n\} = \{4\pi D_z \tau_{int}(\ell)\}^{-1/2} \times \exp\{-(Z_{PLP}-Z_P-v_z\tau_{int}(\ell))^2/(4D_z\tau_{int}(\ell))\}, \quad (2.29)$$

where v_z and D_z are the drift velocity and the difusion coefficient of the charge, respectively. These coefficients were predicted theoretically as follows [2-6];

$$D_z \simeq 0.21\gamma\Delta^{1/2}[E_\ell^*(A_1)/A]^{1/4}[(A_1A_2)^{1/3}/(A_1^{1/3}+A_2^{1/3})]^2(Z/A)^2 \quad (\text{in } 10^{22}s^{-1}) \quad (A.3)$$

$$v_z \simeq -D_z/T_\ell(E_\ell^*,A_1)\,\partial U_\ell(A_1)/\partial A_1(Z/A) \quad (\text{in } 10^{22}s^{-1}) \quad (A.4)$$

with $\gamma\Delta^{1/2} = 2.21$ and the nuclear temperature of the composite system

$$T_\ell(E_\ell^*,A_1) = 3.46(E_\ell^*(A_1)/A)^{1/2}, \quad (\text{in MeV}) \quad (A.5)$$

although D_z and v_z are usually scaled by an appropriate factor to reproduce the data. Here A_1 and A_2 are the masses of the fragments forming the dinuclear system with the mass number A and the atomic number Z. E_ℓ^* and U_ℓ are the excitation energy and the driving potential which were calculated with the formulas [2]:

$$U_\ell(A_1) = U_{LD}(A_1)+U_{LD}(A_2)-U_{LD}(A)+e^2/R_0(Z/A)^2A_1A_2 + v_p(A_1,A_2)+\ell(\ell+1)\hbar^2/(2J_{tot}) \quad (\text{in MeV}) \quad (A.6)$$

and

$$E_{\ell}^{*}(A_1) = E^{*} - e^2/R_0(Z/A)^2A_1A_2 - v_p(A_1,A_2) - \ell(\ell+1)\hbar^2/(2J_{tot}).$$
(in MeV) (A.7)

where U_{LD} is the liquid drop energy when the N/Z value of the product is equal to that of the composite system, E^{*} and v_p are the total excitation energy at $\ell=0$ and the nuclear attractive potential calculated with the proximity potential [7], respectively. J_{tot} is the rigid body moment of inertia with the sticking condition [2]:

$$J_{tot} = \mu R_0^2 + 2/5A_1R_1^2 + 2/5A_2R_2^2, \quad (A.8)$$

where μ, R_1, and R_2 are the reduced mass and radii of the fragments, respectively. R_0 is the interaction distance calculated with a formula $R_0 = 1.2(A_1^{1/3}+A_2^{1/3})$ in fm. Interaction time was calculated in relation to the scattering angle as follws [8];

$$\tau_{int}(\ell)_{2n-1} = J_{tot}/(\hbar\ell)[2\pi(n-1)-(\theta-\theta_{gr})]$$

and

$$\tau_{int}(\ell)_{2n} = J_{tot}/(\hbar\ell)[\theta_{gr}+\theta+2\pi(n-1)]. \quad (A.9)$$

$(n=1,2,\ldots\ldots,\ \tau_{int}>0)$

B. SUM RULE MODEL

The sum rule model proposed by Wilczyński et al. [9,10] combines the ideas of partial equilibration and the critical angular momentum associated with each product. A formula of the Q_{gg} dependence, which is considered to be due to partial equilibration, is assumed in the model as described below.

$$p(i) \propto \exp[(Q_{gg} - Q_c)/T], \tag{2.23'}$$

where

$$Q_c = (Z_P Z_T - Z_{PLP} Z_{TLP}) e^2 / R_c . \tag{2.20}$$

The critical angular momentum of the product is decribed as

$$\ell_{lim}(i) = \frac{A_P A_T}{mA_P + nA_T} \ell_{crit}, \tag{2.26}$$

This relation was found to reproduce well angular momenta of the products in the $^{14}N + ^{159}Tb$ reaction [10]. A smooth cut-off transmission coefficient

$$T_{\ell}(i) = [\ 1+\exp((\ell-\ell_{lim}(i))/\Delta\ )]^{-1} \qquad (2.25)$$

was introduced in the model. Therefore one can obtain the cross section of a product i as follows.

$$\sigma(i) = \pi \lambda\!\!\!^{-2} \sum_{\ell=0}^{\ell_{max}} [(2\ell+1)\ \frac{T_{\ell}(i)p(i)}{\sum_{j} T_{\ell}(j)p(j)}]\ , \qquad (2.24)$$

Differential cross sections of typical products in the 8.8MeV/u ^{16}O-induced reaction on ^{197}Au are depicted in Fig.B.1, where one can see limiting behavior on the angular momentum of each product. The parameters used in the calculation are the same as listed in Table 2.4.

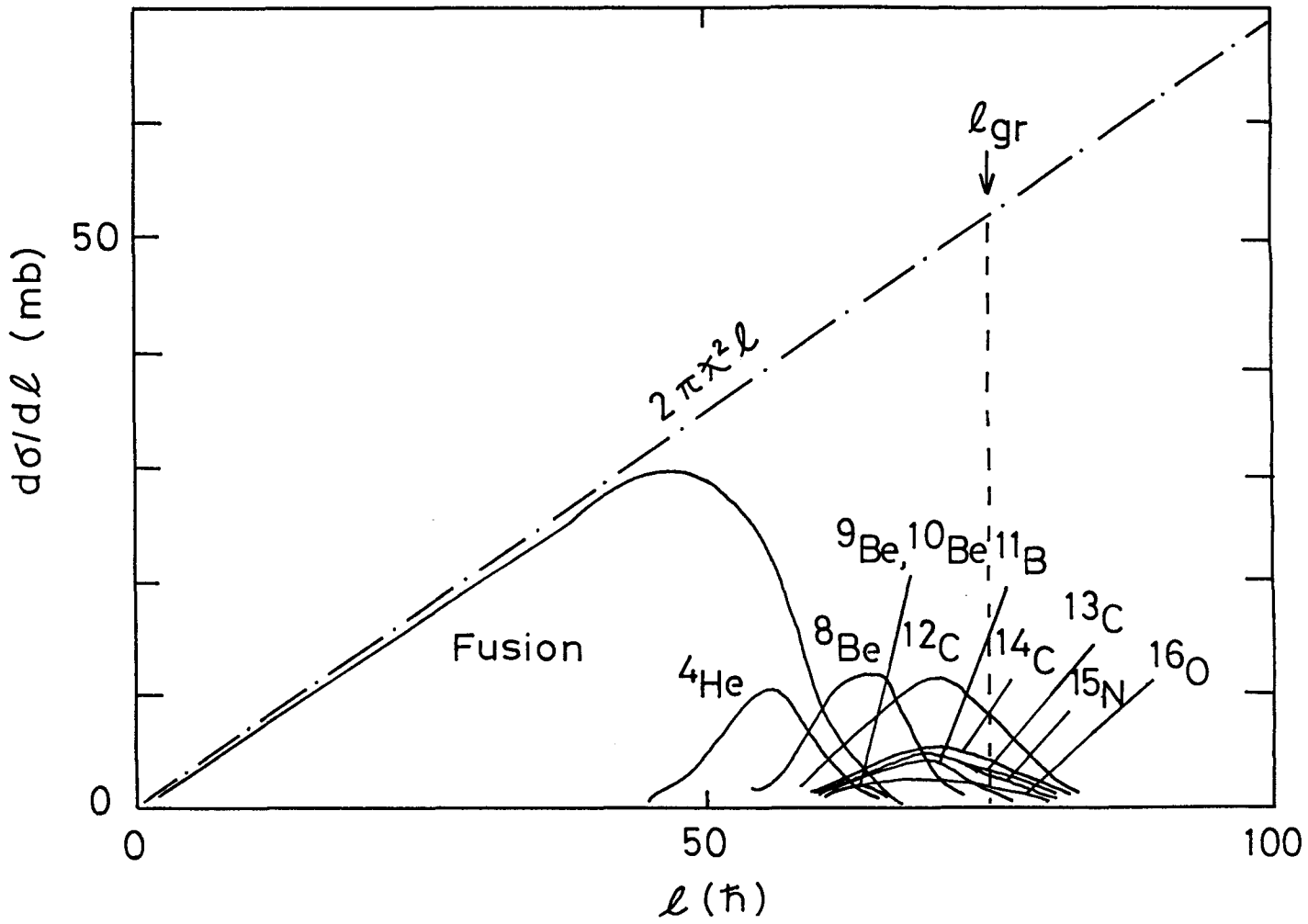

Fig.B.1. Differential cross sections calculated with the sum rule model for the 8.8MeV/u ^{16}O-induced reaction on ^{197}Au (solid line). The parameters used in the calculation are listed in Table 2.4. Dot-dashed line represents the maximum differential cross section at each ℓ. Grazing angular momentum of this system is depicted with dashed line.

REFERENCES TO APPENDICES

1. Nörenberg, W.: Phys. Lett. 52B, 289 (1974)
2. Wolschin, G., Nörenberg, W.: Z. Phys. A284, 209 (1978)
3. Riedel, C., Wolschin, G., Nörenberg, W.: Z. Phys. A290, 47 (1979)
4. Ayik, S., Schürmann, B., Nörenberg, W.: Z. Phys. A279, 145 (1976)
5. Ayik, S., Schürmann, B., Norenberg, W.: Z. Phys. A277, 299 (1976)
6. Schmidt, R., Toneev, V. D., Wolschin, G.: Nucl. Phys. A311, 247, (1978)
7. Blocki, J., Randrup, J., Swiatecki, W. J., Tsang, C. F.: Ann. Phys. (N.Y.) 105, 427 (1977).
8. Agarwal, S.: Z. Phys. A297, 41 (1980)
9. Wilczyński, J., Siwek-Wilczyńska, K., Van Driel, J., Gonggrijp, S., Hageman, D. C. J. M., Janssens, R. V. F., Łukasiak, J., Siemssen, R. H.: Phys. Rev. Lett. 45, 606 (1980)
10. Wilczyński, J., Siwek-Wilczyńska, K., Van Driel, J., Gonggrijp, S., Hageman, D. C. J. M., Janssens, R. V. F., Łukasiak, J., Siemssen, R. H., Van der Werf, S. Y.: Nucl. Phys. A373, 109 (1982)

AKNOWLEDGEMENTS

The works in this thesis have been performed under the direction of Professor Hiroshi Baba of Osaka University. The author wishes to express his sincere gratitude to Prof. H. Baba for his many valuable suggestions, stimulative discussions and kind encouragement, and also for his critical reading of this manuscript.

The author is greatly indebted for helpful discussions and collaborations to the staff of the nuclear chemistry group of Japan Atomic Energy Research Institute (JAERI). In particular, he would like to express his acknowledgement to Dr. Sumiko Baba, Dr. Toshiaki Sekine and Mr. Nobuo Shinohara for their co-operation in activation experiments including chemical separation, to Mr. Kentaro Hata and Dr. Yuichiro Nagame for their co-operation in various phases of in-beam experiments and helpful suggestions, and to Mr. Shin-ichi Ichikawa for operation of an isotope separator on-line (ISOL). The author is also grateful to Mr. Yuichi Hatsukawa of Tokyo Metropolitan University and Mr. Masaaki Magara for co-operation in a experiment with a He-jet transport system. He is indebted to Mr. Hiromitsu Matsuoka for operation of the tandem Van de Graaff accelerator of JAERI and to Mr. Toshio Suzuki for co-operation of γ-ray measurement.

Special thanks are due to Dr. Yoshiaki Tomita of JAERI for his kind instruction of a data-taking system and a data-analyzing system furnished with the tandem accelerator. And the author would like to thank all the

staff of the tandem Van de Graaff accelerator of JAERI.

The author would like to express his appreciation to Professor Ichiro Fujiwara of Otemon Gakuin University for his interesing discussions and co-operation in chemical separation.

The author wishes to express his gratitude to the members of Baba laboratory: to Dr. Tadashi Saito for his helpful advice and co-operation in various phases of these works, to Dr. Naruto Takahashi for co-operation in ISOL experiment, to Dr. Atsushi Shinohara for kind teaching and helpful discussions, and to Mr. Masahide Shoji, now at Mitsui Mining and Smelting Co., Ltd., and Mr. Satoshi Wakamatsu for their co-operation in in-beam experiment and various assistances in these works.

And the author thanks all his friends, whose friendship and encouragement were indispensable to his works.